Performance Testing of a Prototypic Annular Linear Induction Pump for Fission Surface Power

K.A. Polzin, J.B. Pearson, M.P. Schoenfeld, K. Webster, and M.G. Houts
Marshall Space Flight Center, Marshall Space Flight Center, Alabama

T.J. Godfroy
Maximum Technology Corporation, Huntsville, Alabama

J.A. Bossard
BSRD, LLC/Yetispace, Inc., Huntsville, Alabama

The NASA STI Program…in Profile

Since its founding, NASA has been dedicated to the advancement of aeronautics and space science. The NASA Scientific and Technical Information (STI) Program Office plays a key part in helping NASA maintain this important role.
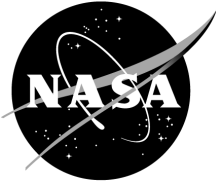
The NASA STI Program Office is operated by Langley Research Center, the lead center for NASA's scientific and technical information. The NASA STI Program Office provides access to the NASA STI Database, the largest collection of aeronautical and space science STI in the world. The Program Office is also NASA's institutional mechanism for disseminating the results of its research and development activities. These results are published by NASA in the NASA STI Report Series, which includes the following report types:

- TECHNICAL PUBLICATION. Reports of completed research or a major significant phase of research that present the results of NASA programs and include extensive data or theoretical analysis. Includes compilations of significant scientific and technical data and information deemed to be of continuing reference value. NASA's counterpart of peer-reviewed formal professional papers but has less stringent limitations on manuscript length and extent of graphic presentations.

- TECHNICAL MEMORANDUM. Scientific and technical findings that are preliminary or of specialized interest, e.g., quick release reports, working papers, and bibliographies that contain minimal annotation. Does not contain extensive analysis.

- CONTRACTOR REPORT. Scientific and technical findings by NASA-sponsored contractors and grantees.

- CONFERENCE PUBLICATION. Collected papers from scientific and technical conferences, symposia, seminars, or other meetings sponsored or cosponsored by NASA.

- SPECIAL PUBLICATION. Scientific, technical, or historical information from NASA programs, projects, and mission, often concerned with subjects having substantial public interest.

- TECHNICAL TRANSLATION. English-language translations of foreign scientific and technical material pertinent to NASA's mission.

Specialized services that complement the STI Program Office's diverse offerings include creating custom thesauri, building customized databases, organizing and publishing research results…even providing videos.

For more information about the NASA STI Program Office, see the following:

- Access the NASA STI program home page at <http://www.sti.nasa.gov>

- E-mail your question via the Internet to <help@sti.nasa.gov>

- Fax your question to the NASA STI Help Desk at 443–757–5803

- Phone the NASA STI Help Desk at 443–757–5802

- Write to:
  NASA STI Help Desk
  NASA Center for AeroSpace Information
  7115 Standard Drive
  Hanover, MD 21076–1320

Performance Testing of a Prototypic Annular Linear Induction Pump for Fission Surface Power

K.A. Polzin, J.B. Pearson, M.P. Schoenfeld, K. Webster, and M.G. Houts
Marshall Space Flight Center, Marshall Space Flight Center, Alabama

T.J. Godfroy
Maximum Technology Corporation, Huntsville, Alabama

J.A. Bossard
BSRD, LLC/Yetispace, Inc., Huntsville, Alabama

Acknowledgments

TRADEMARKS

TABLE OF CONTENTS

LIST OF FIGURES

LIST OF TABLES

LIST OF ACRONYMS AND SYMBOLS

ac	alternating current
ALIP	annular linear induction pump
ATC	ALIP test circuit
CEI	Creative Engineers, Inc.
Cu	copper
DAQ	data acquisition
EM	electromagnetic
FSP	fission surface power
GFSSP	Generalized Fluid System Simulation program
GN_2	gaseous nitrogen
ID	inner diameter
INL	Idaho National Laboratory
I/O	input/output
MSFC	Marshall Space Flight Center
Na	sodium
NaK	sodium-potassium
RF	radio frequency
RT	real time
RTD	resistance temperature detector
SS	stainless steel
TP	Technical Publication
VCR	vacuum compression ring
VFD	variable frequency drive

NOMENCLATURE

A	offset constant
A	fit coefficient
a	curve fit coefficient
B	magnetic induction
B_r	radial magnetic field measurement
B_z	axial magnetic field measurement
b	curve fit constant
C	offset constant
C_L	flow coefficient
C_p	specific heat
c	curve fit coefficient
d	curve fit coefficient
e	curve fit coefficient
f	curve fit coefficient
I	current
m	curve fit coefficient
m	mass
P	power
P_{DAQ}	power measurement obtained using the wattmeter and data acquisition system
P_{IN}	input power
P_{scope}	average of instantaneous power measurement
p	pressure
p_{meas}	measured pump pressure

$p_{\text{meas\_1}}$	inlet hydrostatic pressure
$p_{\text{meas\_2}}$	outlet hydrostatic pressure
p_{pump}	pump pressure
$p_{\text{pump\_in}}$	pressure at pump inlet
$p_{\text{pump\_out}}$	pressure at pump outlet
T	temperature
t	time
V	voltage
v	volume
$\dot{v}$	volumetric flow rate
x	curve fit variable
x_0	fit coefficient
y	curve fit variable
y_0	fit coefficient
Z	electrical impedance
Δp	change in pressure
$\Delta p_{\text{correction}}$	variation in pressure as a function of flow rate
$\Delta p_{\text{leg\_1}}$	pressure loss from expansion from smaller diameter ALIP size to larger pipe
$\Delta p_{\text{leg\_2}}$	pressure loss from contraction of larger diameter ALIP size to smaller pipe
Δp_{meas}	pressure head measurement
η	efficiency
ρ	mass density
σ	fit coefficient uncertainty
σ_v	uncertainty on volume measurement
$\sigma_{\dot{v}}$	uncertainty on volumetric flow

TECHNICAL PUBLICATION

PERFORMANCE TESTING OF A PROTOTYPIC ANNULAR LINEAR INDUCTION PUMP FOR FISSION SURFACE POWER

1. INTRODUCTION

Fission surface power (FSP) systems could be used to provide power on the surface of the Moon, Mars, or other planets and moons of our solar system. Fission power systems could provide excellent performance at any location, including those near the poles or other permanently shaded regions, and offer the capability to provide on-demand power at any time, even at long distances from the Sun. Fission-based systems also offer the potential for outposts, crew, and science instruments to operate in a power-rich environment. NASA has been exploring technologies with the goal of reducing the cost and technical risk of employing FSP systems. A reference 40-kW$_e$ option has been devised that is cost competitive with alternatives while providing more power for less mass anywhere on the lunar surface. The reference FSP system is also readily extensible for use on Mars. On Mars, the system would be capable of operating through global dust storms and providing year-round power at any martian latitude.

One key technology associated with the FSP system is the pump that circulates liquid-metal coolant through the reactor system. An annular linear induction pump (ALIP) was designed to the reference mission requirements and tested at representative operating conditions. This Technical Publication (TP) details the performance testing of this prototypic FSP reference mission ALIP.

1.1 Fission Surface Power Technology Development

Under the NASA Exploration Technology Development program, NASA and the Department of Energy have begun long-lead technology development for potentially supporting future integrated FSP systems. The major effort in the FSP technology project has been focused on a reference mission and concept. The reference mission is to provide electrical power to habitats on the lunar surface. The requirements derived from this mission are 40 kW$_e$ delivered to the habitat, and a design life of 8 yr. Although many options exist, NASA's current reference FSP system uses a fast spectrum, pumped liquid, sodium-potassium- (NaK-) cooled reactor coupled to a Stirling power conversion subsystem. The reference system uses technology with significant terrestrial heritage that can perform at any location on the surface of the Moon or Mars. Detailed development of the FSP concept and the reference mission are documented in various other reports.[1–4]

The objectives of the FSP technology project are as follows:[5]

- Develop FSP concepts that meet expected surface power requirements at reasonable cost with added benefits over other options.

- Establish a non-nuclear hardware-based technical foundation for FSP design concepts to reduce overall development risk.

- Reduce the cost uncertainties for FSP and establish greater credibility for flight system cost estimates.

- Generate the key non-nuclear products to allow Agency decision makers to consider FSP as a viable option for potential future flight development.

One key technology associated with the FSP system is the liquid-metal pump. The pump must be compatible with the liquid NaK coolant and have adequate performance to enable a viable flight system. Idaho National Laboratory (INL) was tasked with the modeling, design, and fabrication of an ALIP suitable for the FSP reference mission.[6] A prototypic ALIP was fabricated under the direction of INL and shipped to NASA Marshall Space Flight Center (MSFC) for testing at representative operating conditions. This pump was designed to meet the requirements of the FSP reference mission. In addition, it incorporates unique design features to increase pump performance over typical industrial pumps in anticipation of the higher performance and lower weight typically required for a flight system. Analysis of the measured performance, as compared to the design predictions, as well as implications for the next ALIP design iteration, can be found in the companion report published by INL.[6] The ALIP test circuit (ATC) used to test the present pump will also be used to test future ALIPs for the FSP Technology Development program, including a pump designed for the Technology Demonstration Unit, which is a 10-kW$_e$, end-to-end test of FSP technologies intended to raise the entire FSP system to technology readiness level 6.

1.2 Nonnuclear Testing at Marshall Space Flight Center

The Early Flight Fission-Test Facility was established by MSFC to provide a capability for performing hardware-directed activities to support multiple in-space nuclear reactor concepts by using a nonnuclear test methodology.[7,8] This includes fabrication and testing at both the module/component level and near prototypic reactor components and configurations, allowing for realistic thermal-hydraulic evaluations of systems. In the present testing, the ATC was fabricated to provide the capability to measure the performance of induction pumps over a wide range of input conditions and environments. The system is described in detail in section 2, followed by measured performance results on the present ALIP.

2. ANNULAR LINEAR INDUCTION PUMP TEST CIRCUIT HARDWARE AND TEST SETUP

The ATC apparatus, shown schematically in figure 1 and photographically in figure 2, was fabricated to allow for performance testing of liquid-metal induction pumps. The present test circuit consists of the ALIP, an induction heater, a throttling valve, an electromagnetic flowmeter, and a gaseous nitrogen- (GN_2-) to-NaK heat exchanger. A large pipe size (3-in, schedule 10, stainless steel (SS)) was employed to minimize the viscous flow losses throughout the loop. In this section, the major hardware and instrumentation components of the system are described in detail.
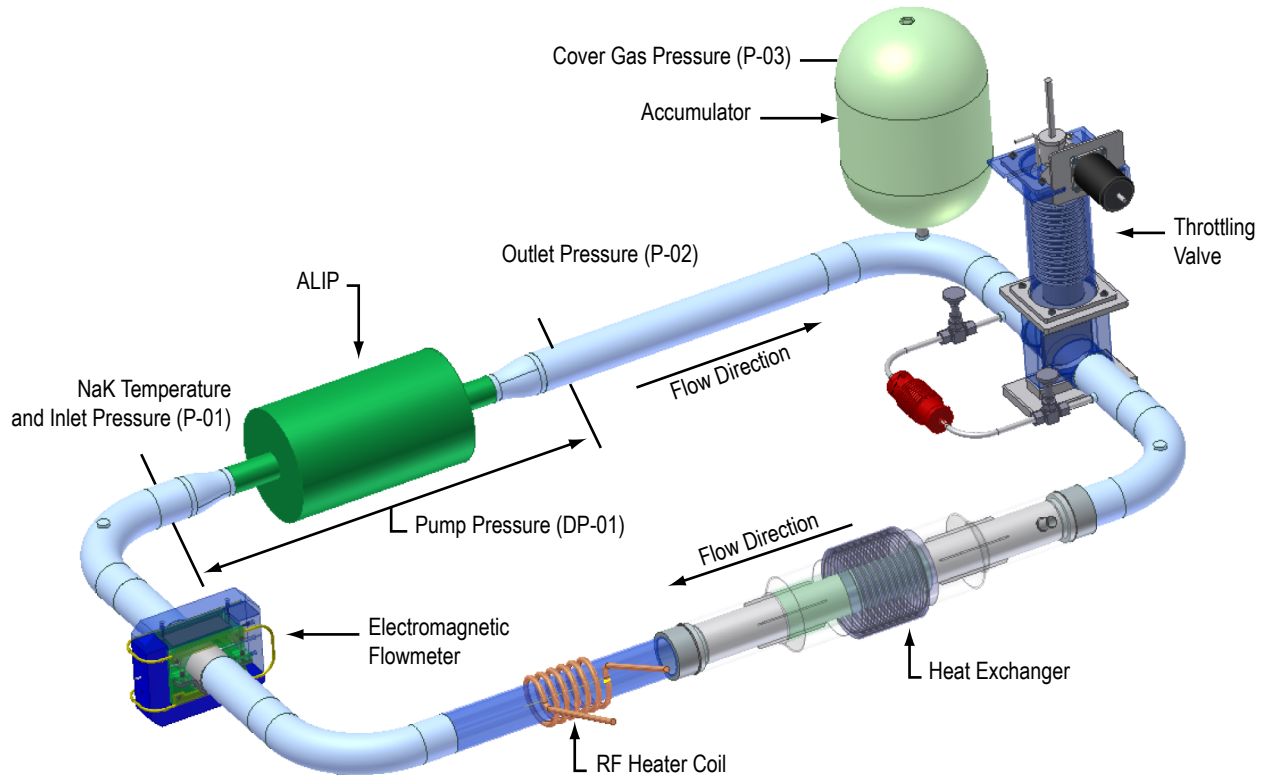
Figure 1. Schematic of the ALIP test circuit.
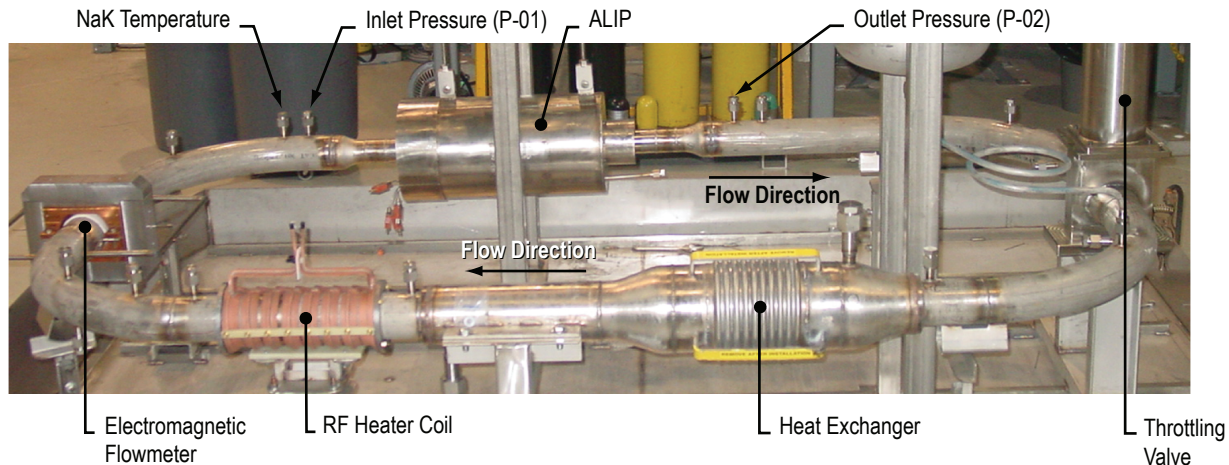
Figure 2. Photograph of the assembled ALIP test circuit.

2.1 Components in the System

2.1.1 Annular Linear Induction Pump

The primary test article is the ALIP shown in figure 3. The design and development of the pump was performed by INL and is discussed in a companion report.[6] Three-phase power is applied to the pump to produce an axially-traveling magnetic wave. This magnetic wave induces currents in the liquid metal, which subsequently interact with the magnetic field to produce a Lorentz body force on the fluid, pushing it through the system.

The power applied to the pump is completely characterized by the voltage, current, and frequency of the three-phase power. In the present experiment, the voltage and frequency were controlled, while the electrical impedance of the pump dictated the current. Two different power sources were applied to the pump. The first was an Allen Bradley PowerFlex 400 variable frequency drive (VFD), which allowed for setting the frequency of the power delivered to the pump to an arbitrary value from zero to 60 Hz. The VFD employs pulse width modulation (using a 4-kHz carrier wave frequency) to produce an approximately sinusoidal current at these arbitrary frequency levels. A sample of the raw output of the VFD is shown in panel (a) of figure 4 with a section of the output enlarged in panel (b) to show the detail on the pulse width modulation. A second method for applying power was directly from the electrical grid, which provided a very clean, purely sinusoidal—in both current and voltage—waveform at 60 Hz.

While the raw current output of the VFD was a good approximation of a sinusoidal wave, it is difficult to combine it with the modulated voltage waveform to obtain an accurate power measurement owing to the very fast voltage switching. To alleviate this issue, a sine wave filter was employed to filter the VFD voltage output into an approximately sinusoidal waveform that could be better combined with the current waveform within the data acquisition (DAQ) system to measure power. The effectiveness of filtering is demonstrated in figure 5. The raw VFD output at 36 Hz is shown in

4
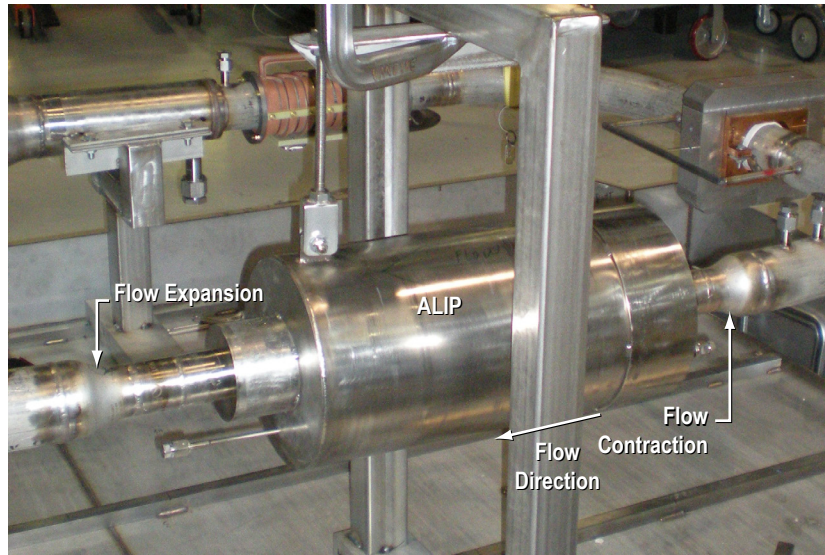
Figure 3. The ALIP installed in the test circuit.

(a)

(b)
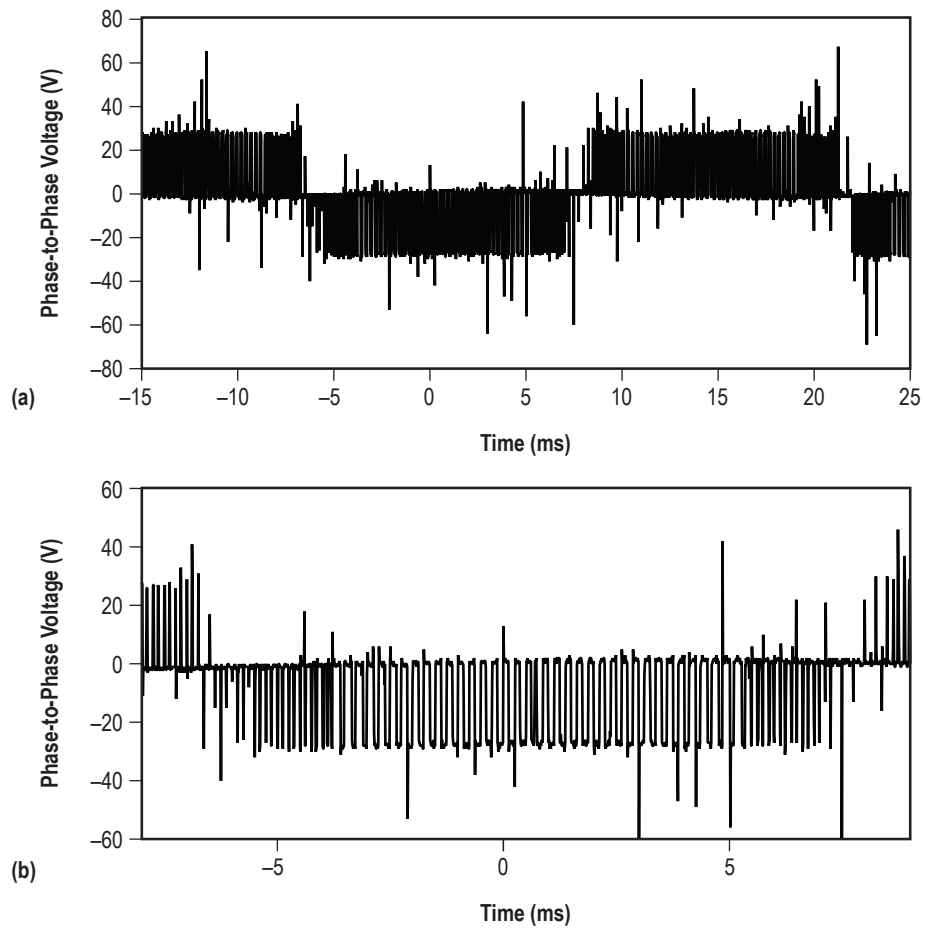
Figure 4. Sample waveform showing (a) the raw voltage output of the VFD
at 36 Hz and (b) an enlarged section of the output showing
the detail on the pulse width modulation.
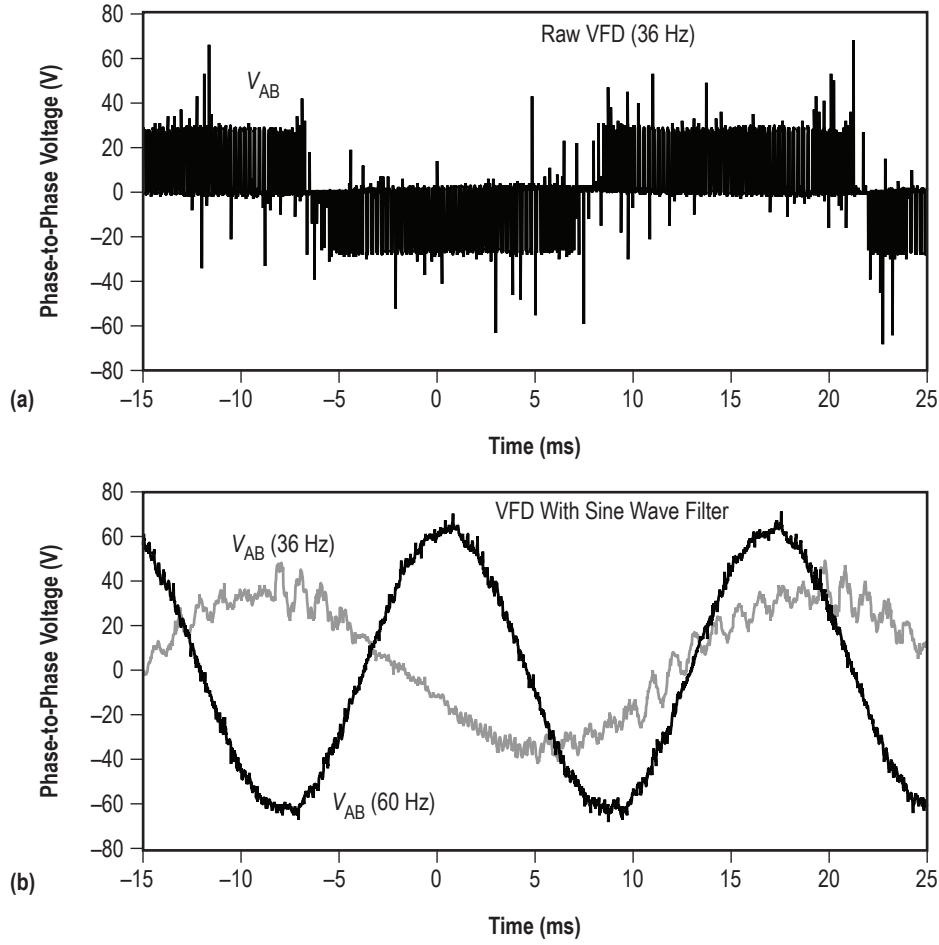
Figure 5. Sample voltage output: (a) raw VFD waveform at 36 Hz and
(b) the sine wave filtered voltage waveforms at 36 and 60 Hz.

panel (a) and the filtered VFD output for both 36 and 60 Hz is shown in panel (b). The slight oscillations on the filtered voltage waveforms only affect the measurements of voltage and power in the DAQ at low voltage levels (below 30–40 V ac).

The filtered VFD output or power from the electrical grid was passed through a variac transformer to control the voltage. By adjusting the variac, the voltage and commensurate power to the pump could be controlled to an arbitrary level.

2.1.2 Throttling Valve Design

An in-house custom design was chosen for the throttling valve owing to the unique system-level requirements. These included operation in a hot NaK environment, very low pressure drop in the flow configuration where the valve was fully open, and a requirement to not deadhead the pump (i.e., valve should not fully close and seal). To produce the smallest pressure drop across the valve, a gate valve design was selected, making use of a welded bellows to provide actuation and hermetic sealing of the valve. The high-temperature NaK required SS or similar materials for all wetted surfaces.

6

The final design of the gate valve is shown in figure 6. The gate was required to translate completely across the duct to decrease the pressure drop as much as possible. The gate itself was constructed of Inconel®. This material was selected because it has a lower coefficient of thermal expansion than the SS grade 304 that comprised the rest of the valve body, and also to prevent galling between the valve body and the gate.
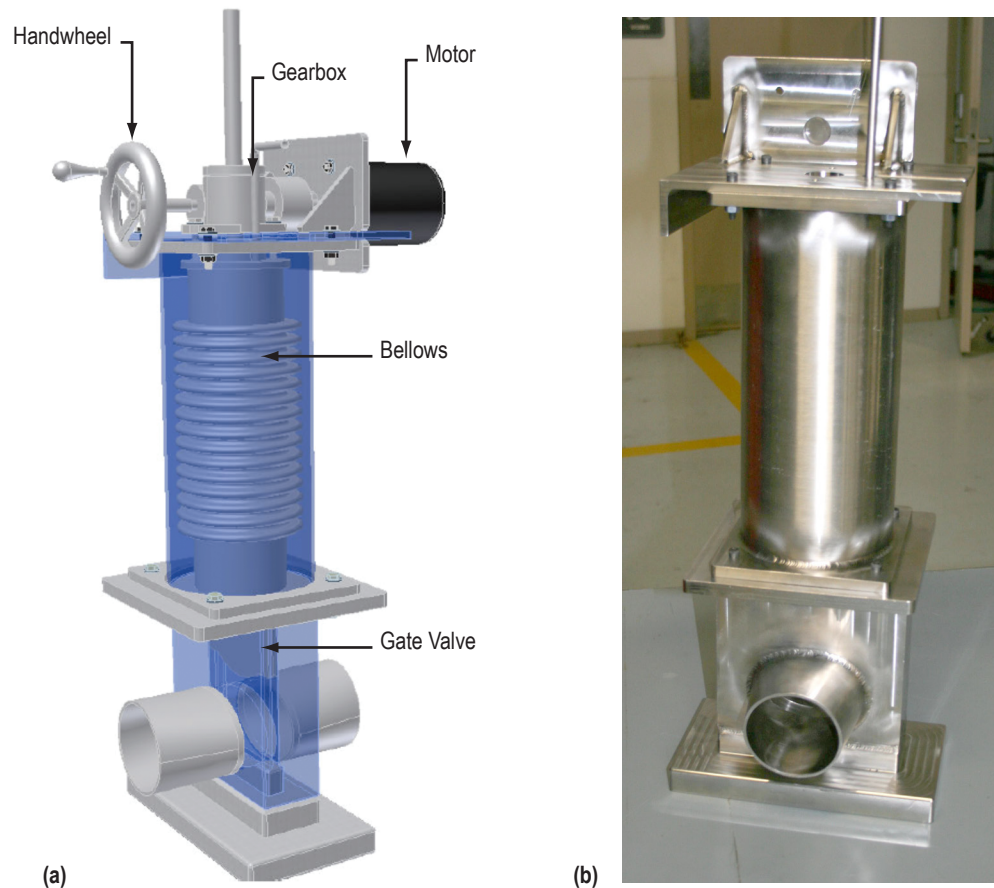
Figure 6. Throttling valve used on the ATC: (a) Rendering and (b) photograph.

The bellows was sized to provide 3 in of travel corresponding to the height of the duct. The neutral point of the bellows was located at the approximate midpoint in the duct, resulting in the bellows in tension when fully open and compression when fully closed. A stress analysis of the valve was performed and is documented in appendix A.

A vacuum-rated motor is connected through a worm-drive gearbox to the top plate of the bellows. The stepper motor allows for precise and repeatable positioning of the valve gate. A tube was installed at the top of the bellows to allow for evacuation of trapped gases and to facilitate posttest cleaning.

The effectiveness of the throttling valve is demonstrated in figure 7. The experimental test data presented in this figure show the pressure rise imparted by the pump, and the NaK volumetric

flow rate—at relatively constant pump power—as a function of valve position. The zero (0) position is equivalent to a fully open valve and the valve 'fully closed' limit switch is set at 7.744 cm (3.049 in). As the valve closes, the flow resistance in the system increases. This leads to a decrease in the flow rate and a commensurate increase in the pressure rise imparted to the fluid by the pump.

2.1.3 Radio Frequency Heater

The NaK was heated using the radio frequency (RF) inductive heater coil shown in figure 8. The coil was manufactured by Fluxtrol, Inc., Auburn Hills, MI, and was powered using a Toccotron 400, 12.5-kW, inductive heater power supply. Two thermal images of the coil heating the flow channel are presented in figure 8 to demonstrate the effectiveness of heating.

Several issues were encountered during heating. First, the thermal insulation of the loop was incomplete, allowing significant amounts of heat to escape, which necessitated the addition of auxiliary heating elements (see sec. 2.1.4). Second, the coil could not be operated at full power because the vacuum level inside the chamber was only in the 1 to 10 mTorr range, which is very amenable to inductive breakdown (plasma formation). Once a plasma would form, the coil ends would short circuit, which rapidly changed impedance of the load and forced the inductive power supply to automatically shut down. Consequently, full-power inductive heating could not be achieved in this test setup. Finally, the impedance mismatches in the transmission line between the power supply and the coil most likely caused significant power reflection in the system, reducing power to the coil to something well below the level set on the supply.

2.1.4 Auxiliary Resistive Heater Elements

Four graphite heaters were added to the ATC during testing to provide additional heat and allow for reaching the target maximum circuit temperature. The site of installation was immediately downstream of the ALIP as it was the only location on the ATC with a straight run of pipe available to receive the heaters. The design involved clamping four tubes to the sides of the ATC pipe wall and sliding the heaters inside these tubes (see fig. 9). The final design had to:

• Generate enough thermal energy from the heaters to heat the NaK to 525 °C.

• Affix the heaters to the side of the ATC pipe wall without welding.

• Achieve adequate heat transfer from the heaters to the NaK.

Each heater is capable of delivering ≈2,800 W. Four heaters wired in series were capable of producing between 6,000 and 7,000 W and were limited only by the power supply in this case.

The main challenges were providing for adequate heat transfer and allowing for thermal expansion and contraction. The heater tube is clamped to the ATC pipe, which leads to point contacts and poor thermal conduction between the tube and the pipe.

8
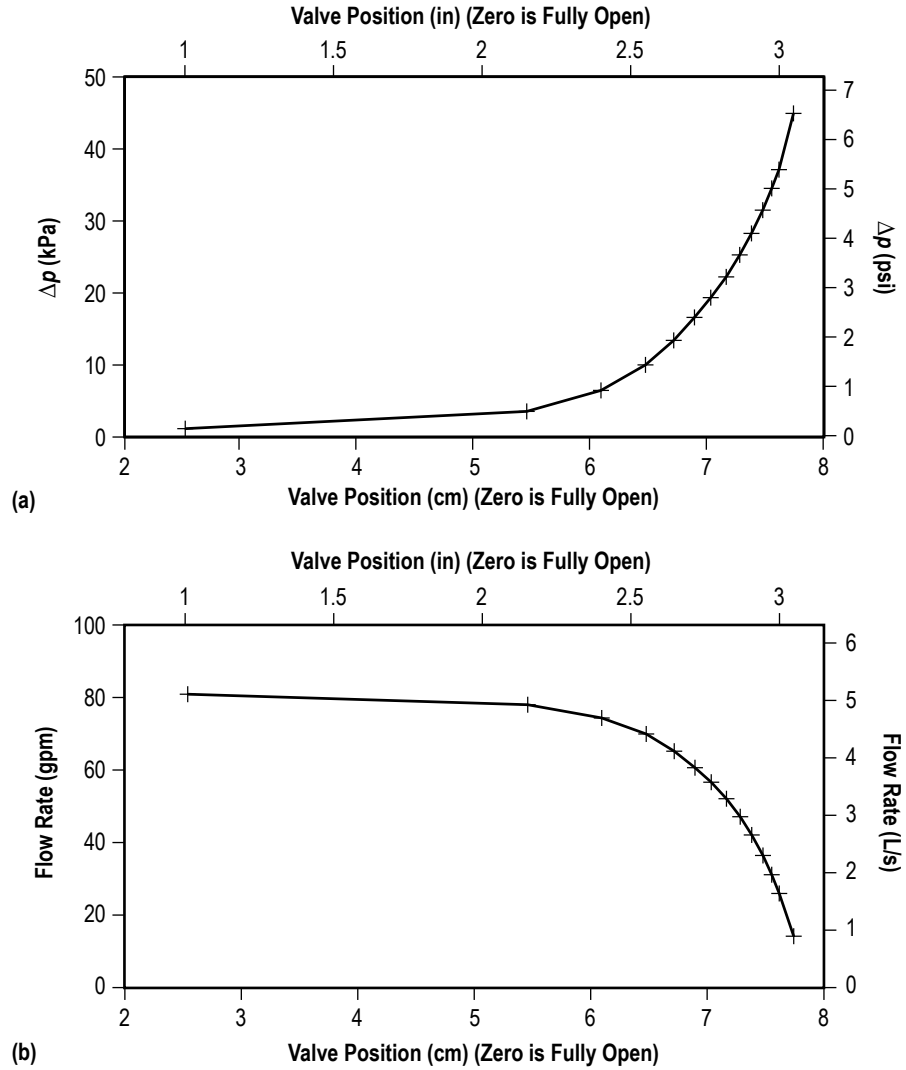
Figure 7. Throttling valve test data showing (a) the pressure across the pump
and (b) the NaK volumetric flow rate as a function of valve position.

A combination of copper (Cu) screen and Cu tape was used to enhance the thermal conductivity between the heater tubes and the ATC pipe. Copper screen was packed into the small spaces between the heater tube and the ATC pipe and was also packed into the space between the heater tubes. The entire assembly then was wrapped in Cu foil. A photograph of the final assembly is presented in figure 10. Clamps were employed to keep the mesh compacted into the various spaces.
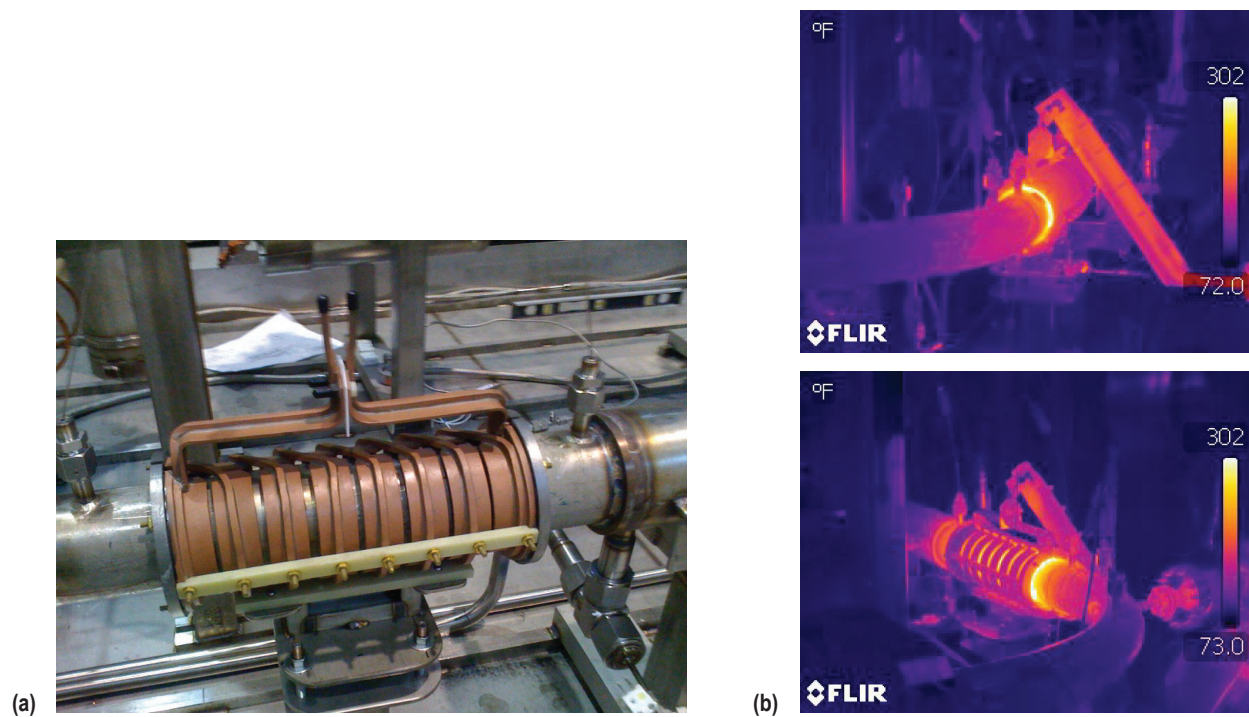
Figure 8. Photograph of the (a) RF inductive heater coil
and (b) two thermal images of the coil in operation.
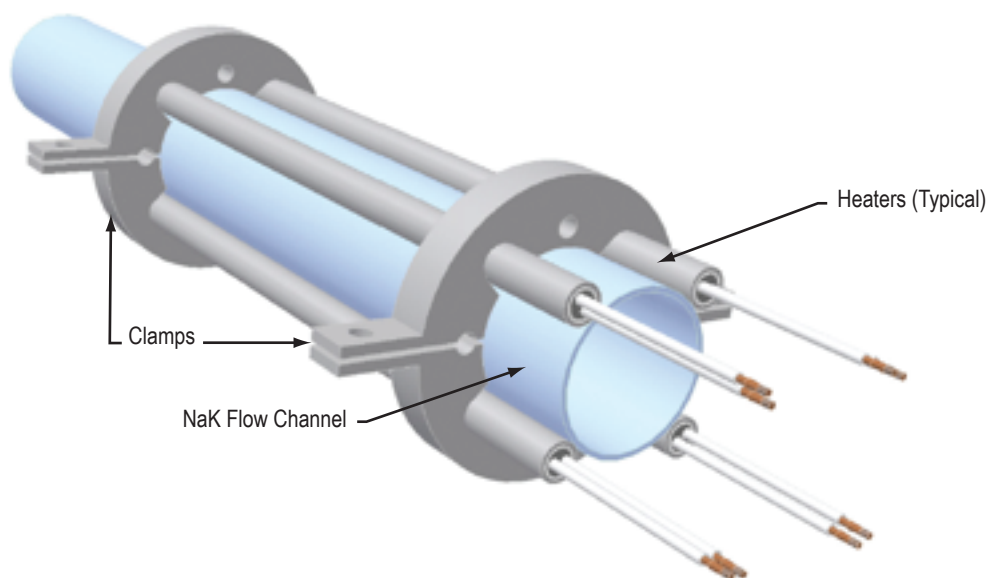
Figure 9. Rendering of the add-on heater assembly.

Figure 10. Final add-on heater assembly before the application of multilayer insulation.

2.1.5 Heat Exchanger

A gas-to-NaK counterflow concentric tube heat exchanger was used to provide cooling and temperature control for the loop (fig. 11). The heat exchanger was sized to provide 10 kW of cooling to the system using GN_2 as the heat exchange medium. The NaK side of the heat exchanger was designed as a continuation of the 3-in, schedule 10 pipe comprising the loop. The length and diameter of the GN_2 side of the heat exchanger were sized through heat transfer considerations. The heat exchanger employs a bellows section to accommodate differential expansion between the pipe and GN_2 shell. The shell consists of a 4-in, schedule 10S pipe with a custom bellows section fabricated by Pathway Bellows, Inc., Oak Ridge, TN, and was 36 in long. The bellows section includes a flow liner to reduce flow-induced vibrations and to maintain a small radial flow gap to maintain high convection rates. The GN_2 shell was sealed on the ends by welding annular disks between the ends of the shell and the outside of the NaK pipe.

A gas preheater was used to heat the GN_2 entering the heat exchanger to alleviate thermal shock and to provide finer control of heat removal at high temperatures. Additionally, this preheater/heat exchanger combination was used to heat the loop during heat-up transients and when additional heating was needed to supplement the induction heater.

11
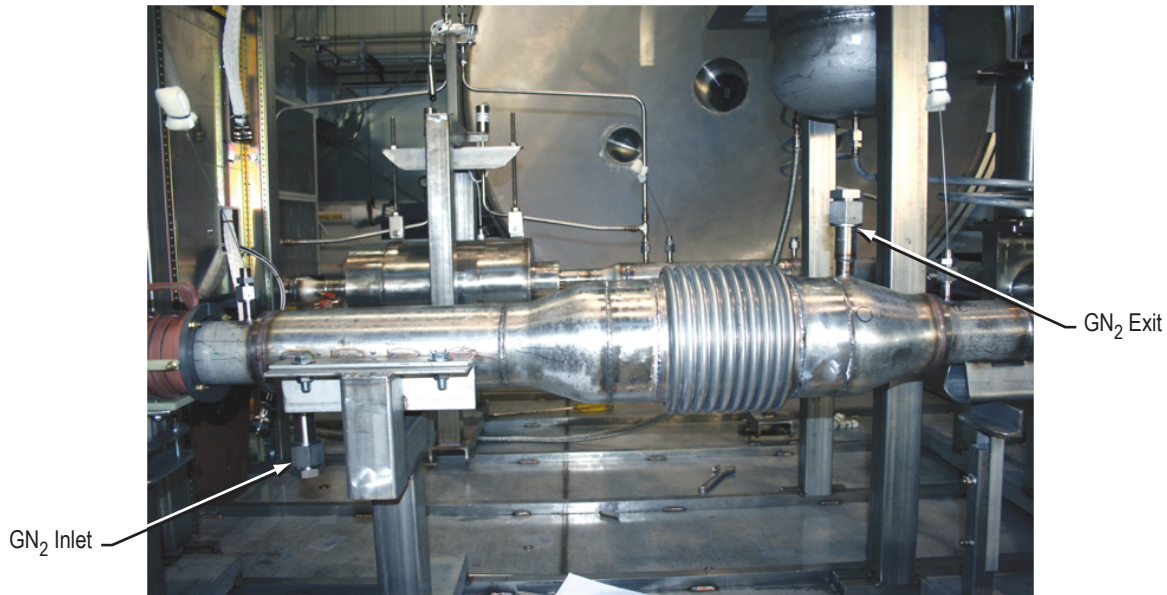
Figure 11. Gas-to-NaK heat exchanger installed in ATC.

2.2 Major Instrumentation

2.2.1 Data Acquisition and Control Platform

The DAQ and control system is based on National Instruments hardware and software. The system consists of a Windows XP-based PC for user interaction and data recording, a PXI-1042 chassis for DAQ and control, and an SCXI-1001 chassis for signal conditioning.

The PC runs an in-house-developed LabVIEW™ application that communicates via Transmission Control Protocol/Internet Protocol with the real-time LabVIEW application running on the controller in the PXI-1042 chassis. The PC application receives data and status information for display and recording and transmits user-initiated commands to the controller in order to operate the experiment. The application provides a user interface for operating the RF heater, throttling valve, heat exchanger, and data recorder. It also provides visual feedback on the status of and data from the system.

The PXI-1042 chassis includes a PXI-8110 Real-Time (RT) embedded controller, a PXI-6281 DAQ module, a PXI-6704 analog output module, and a PXI-6528 digital input/output (I/O) module. The PXI-8110 has a 2.26-GHz quad-core processor running the LabVIEW RT operating system. The controller runs an in-house-developed LabVIEW RT application that acquires data through the PXI-6281 DAQ module, scales the data into engineering units, monitors the data for alarm conditions, and transmits the data to the PC application for recording and display. The RT application also controls the operation of the experiment in direct response to commands from the PC application and provides appropriate feedback status to the PC application. Any closed-loop control is handled by the RT application. The PXI-6281 DAQ module is used to scan all available channels from the SCXI-1001 chassis that handles all signal conditioning.

12

The SCXI-1001 chassis includes SCXI-1102 analog input modules and an SCXI-1503 resistance temperature detector (RTD) analog input module. The SCXI-1102 module is used to condition analog voltage signals from various instrumentation transducers, including thermocouples and pressure transducers. The SCXI-1503 RTD module is used to condition readings from an RTD, which measures the temperature of a thermocouple cold junction located on the test rig inside the vacuum chamber.

2.2.2 Pressure Transducers

There are four pressure transducers of interest on the NaK-filled part of the experiment (see figs. 1 and 2). All of these transducers are manufactured by Delta Metrics, Worthington, OH. The transducer P-01 measures the absolute pressure of the NaK upstream of the ALIP, while the transducer P-02 performs the same measurement downstream of the ALIP.

The transducer DP-01 (Δp transducer) yields a measurement of the differential pressure rise across the pump and uses the same ports as P-01 and P-02. Finally, P-03 is located on the accumulator and measures the pressure of the argon cover gas used to pressurize the NaK.

As can be seen in figure 1, the transducers P-01, P-02, and DP-01 perform their measurements beyond flow transitions from the 5.08-cm (2-in) piping on the ALIP to the 7.62-cm (3-in) piping on the rest of the loop. Since there are pressure losses associated with the reduction and enlargement of the cross-sectional area of the pipe, the pressure rise across the pump will be greater than that measured by the pressure gauges on the loop. Consequently, the pressure rise data used for computing the pump performance are corrected to account for the transitions. The magnitudes of these effects can be found in the presentation of performance data (sec. 3) and in appendix B.

Data comparing the measurement of the Δp transducer to a Δp computed by taking the arithmetic difference between P-02 and P-01 are presented in figure 12. In this figure, the flow is stagnant at the left side of the graph, and both the Δp transducer measurement and P-02 minus P-01 are equal to zero. As the flow is started and the Δp increased by closing the throttling valve, a deviation is observed between the Δp transducer measurement and P-02 minus P-01. As the throttling valve is reopened, reducing the Δp across the pump, the offset between the Δp transducer and P-02 minus P-01 persists. As the flow is reduced to zero, the Δp transducer output is negative by roughly the same amount that it deviated from P-02 minus P-01 at the peak level, while the value of P-02 minus P-01 returns to zero. Therefore, P-02 minus P-01 is considered to be the more accurate measurement of Δp and will be used throughout the rest of this TP.

The absolute pressure transducer data from P-02 and P-01 are plotted in panel (a) of figure 13, along with the argon cover gas pressure measured by P-03. In addition, the Δp measurement is given in panel (b) of the same figure. While the pressure on all three gauges oscillates up and down as the valve is closed and opened, it is observed that at each valve setpoint, the value of Δp is relatively constant, as would be expected. Also note that all three pressure values are roughly the same at the 'no flow' condition, which is also an expected result if all three gauges were operating properly.
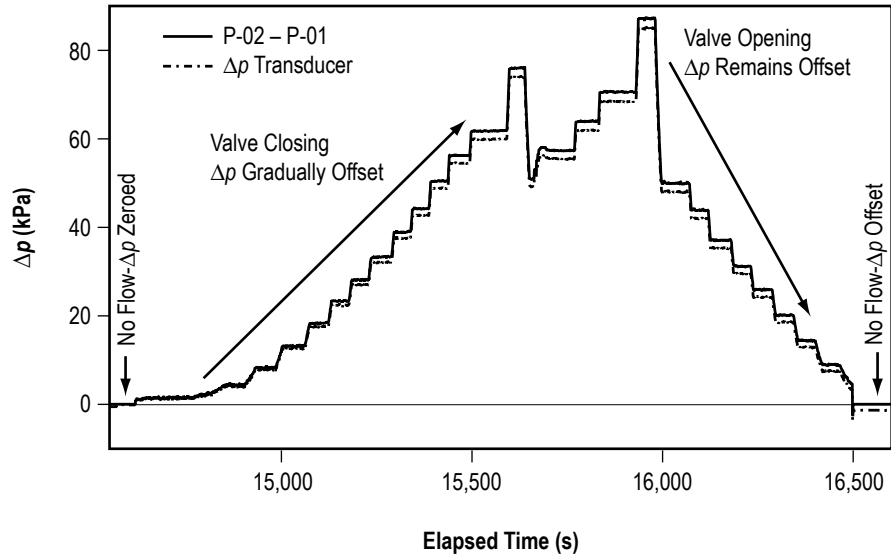
Figure 12. Data comparing the measurement of the Δp transducer to a Δp computed by taking the arithmetic difference between P-02 and P-01.
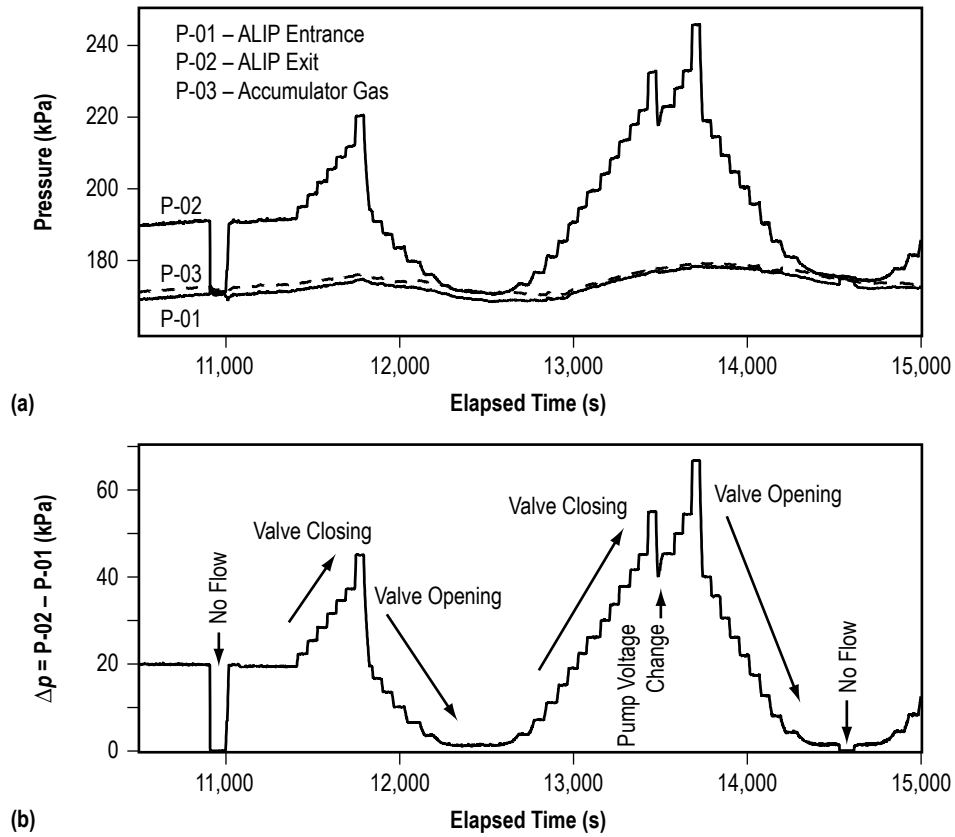
Figure 13. Measurements of (a) absolute pressure transducers on the NaK and argon cover gas and (b) calculated Δp displayed as a function of time.

The random uncertainty on the Δp data set is calculated to be 100–200 Pa (standard deviation of the data acquired at a given valve setpoint). However, the accuracy of the DAQ system is not as small as this value. The transducers yield a 5-V output over a pressure range of 689.5 kPa (100 psia). They are read through a National Instruments SCXI-1102 signal conditioner into a PXI-6281 DAQ card. The error on each pressure measurement through the given instrumentation chain is ≈258 Pa. When combined, the error for the difference in measurements between P-02 and P-01 yields a total Δp uncertainty of 365 Pa, which is taken as the uncertainty on all the Δp measurements.

Before leaving this topic, the Δp transducer exhibited significant drift, not just as the valve was exercised, but throughout the course of testing. This drift is likely due to a combination of several different causes. The transducer was observed to drift over time and was also seen to drift as the loop was heated. It is possible this drift was due not only to thermal effects to the transducer, but also to stresses induced in the transducer body as the two tubes connecting the transducer to the upstream and downstream ends of the ALIP moved apart under thermal expansion. The latter source could be observed when stressing the tubes by hand created a similar drift in the measurement.

Another potential problem could have been the presence of trapped gases inside the tubes, creating a compressible layer between the transducer diaphragms and the NaK. Even with the tubes clamped into place to minimize their movement, and after the attempt was made to pull all the gas from the transducer lines, drifts like those shown in figure 12 were still observed. Using thinner tubing and doing a more thorough job strain relieving the tubes connecting the transducer to the loop might help alleviate the problems, but it is still unclear whether the deviation and hysteresis observed in the Δp transducer data would be eliminated using these techniques.

2.2.3 Electromagnetic Flowmeter

An electromagnetic (EM) flowmeter (fig. 14) is used to measure the volumetric flow rate of NaK in the system. It consists of two neodymium-iron-boron magnets opposing each other on opposite sides of the pipe containing the flowing NaK. The magnetic flux return is provided using the magnetically permeable material Fluxtrol (Fluxtrol, Inc.). Copper blocks were designed into the flowmeter to hold the magnets apart and provide the ability to remove heat that might be imparted from the hot NaK flow channel. The Cu blocks are water cooled to thermally stabilize the magnets. A porous-ceramic blanket material is overlaid on the NaK flow channel to restrict heat transfer to the magnets. When the chamber is evacuated, this limits the heat transfer rate to thermal conduction along the tenuous paths presented by the ceramic material.
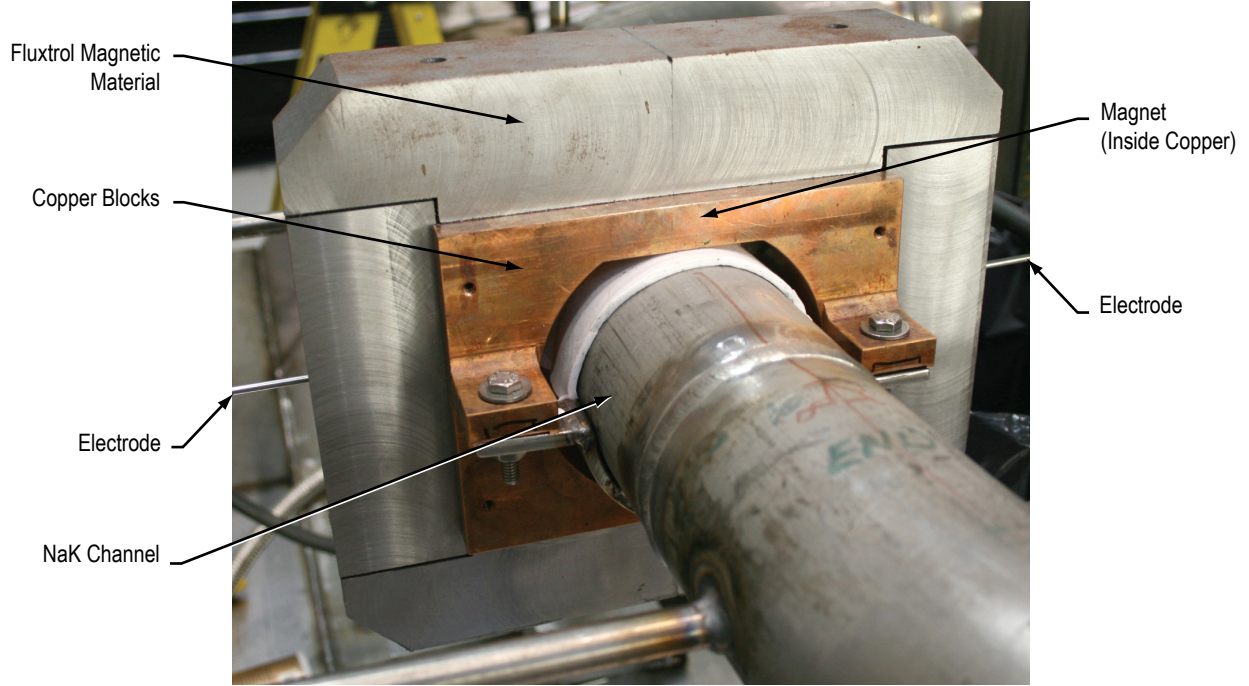
Figure 14. Electromagnetic flowmeter.

The principle of operation of an EM flowmeter derives from Faraday's law and is succinctly stated as follows: A 'back-emf' is induced in an electrically conductive medium—a conductive liquid in the present case—moving transverse to an applied magnetic field.[9] The volumetric flow rate ($\dot{v}$) is linearly related to the induced voltage (V) and can be written as

$$\dot{v} = \text{m } V + \text{b} , \tag{1}$$

where the constant m is a function of the magnetic field strength and the geometry of the flow channel and b is an offset constant. The value of m is typically determined by calibration and the value of b is typically set equal to zero. The calibration process employed for the present test apparatus is detailed in appendix C. The coefficients m and b obtained through that process are 0.4063 ± 0.0047 L/s / mV (6.440 ± 0.075 gpm/mV) and 0 ± 0.0070 L/s (0 ± 0.111 gpm), respectively. The voltage is measured across the flow channel and amplified using a Wilkerson field-programmable isolation amplifier to improve the signal-to-noise ratio before being fed into the DAQ system.

2.2.4 Annular Linear Induction Pump Power Measurements

The ALIP power is measured using an Ohio Semitronics two-meter wattmeter (model P-144D). The unit monitors the real three-phase power delivered to any load (connected in either a delta or a wye configuration) by simultaneously monitoring the current in two of the three legs and measuring the voltage in all three legs.[10] In the present test setup, the wires to the ALIP are looped through the current transducers four times to increase the signal-to-noise ratio in the measurement.

16

The measurement was calibrated using the method described in appendix D. This calibration method provided a data correction factor at low power that was dependent on the frequency of the three-phase power fed to the pump. It also allowed for a significant reduction in the reported error on the power measurement. The correction factors and uncertainties are also found in appendix D.

2.2.5 Temperature Measurements

Temperature measurements were acquired using thermocouples mounted in two ways— clamped externally to the piping and inserted in thermal wells at the flow centerline (fig. 15). Both mounting techniques were used in order to better understand the advantages and limitations of each. A discussion of the differences in the resulting measurements is presented in section 4.3.
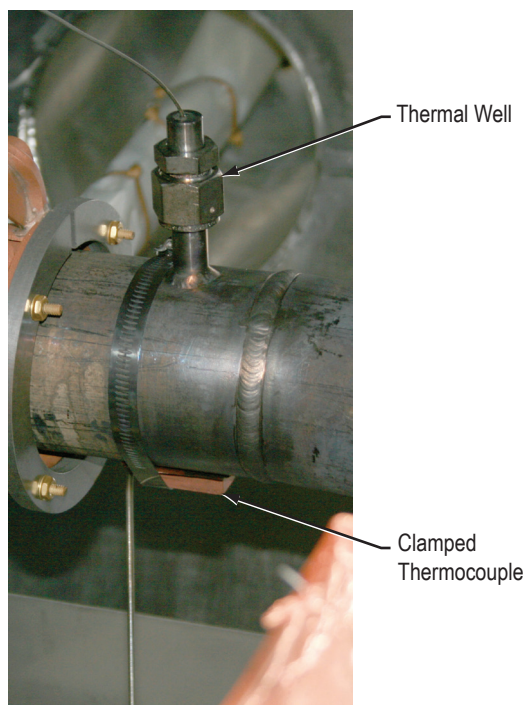
Figure 15. Clamp-on thermocouple and thermal well installed in ATC.

A thermocouple was inserted into a small Cu block, which was then clamped to the outside of the pipe. The block had one convex face that was designed to fit the contour of the pipe and provide good thermal contact. Figure 16 shows a typical block and thermocouple assembly. Note that the tip of the probe is axially located near the center of the block, and is placed in the block as close to the pipe as possible. This mount is a significant improvement over thermocouple probes clamped directly to the pipe as it reduces both the installation inconsistencies and oxidation of the thermocouple, both of which can lead to large uncertainties in the temperature measurement. Figure 15 demonstrates a typical installation in the experiment.
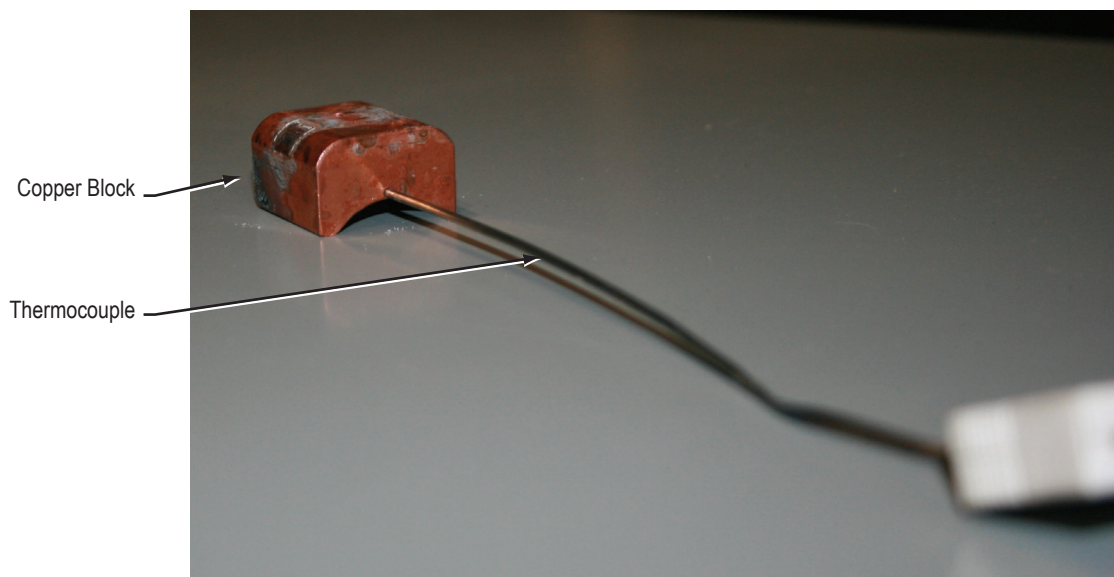
Figure 16. Typical mounting block for a clamp-on thermocouple.

The thermal wells (fig. 15) were installed to obtain more accurate steady-state and transient bulk NaK flow temperature measurements at the flow centerline. The thermal well protrusions were designed to be thin to minimize the contributions to pressure drop.

Each thermal well was installed through a tube boss with a ½-in female vacuum compression ring (VCR®) weld gland (fig. 15). The thermal well assembly was fabricated (fig. 17) by boring a ¼-in hole in a ½-in VCR male blank. A section of ¼-in tube was inserted to accept the thermocouple probe and provide rigidity inside the VCR weld gland. A ⅛-in SS rod was bored to a wall thickness of roughly 0.5 mm (0.020 in) to accept the thermocouple probe, with 0.5-mm (0.020-in) thickness left at the tip to leave the thermal well hermetically sealed from the NaK. The ⅛-in rod was inserted into the end of the ¼-in tube. It was placed so that the rod protruded into the pipe flow with the thermocouple probe tip located on the pipe centerline. The entire assembly was welded, as indicated in figure 17, and the thermocouple probe was brazed into the thermal well (Lucas Milhaupt Braze 716) to permit good thermal contact. An assembled thermal well is presented in figure 18.

(a)

¹⁄₁₆-in SS Sheathed Thermocouple

Gap Filled With Braze (Full Length)

½-in Male VCR Blank (Gasket)

0.065
0.25
0.02
0.125
0.02

2

4

(b)
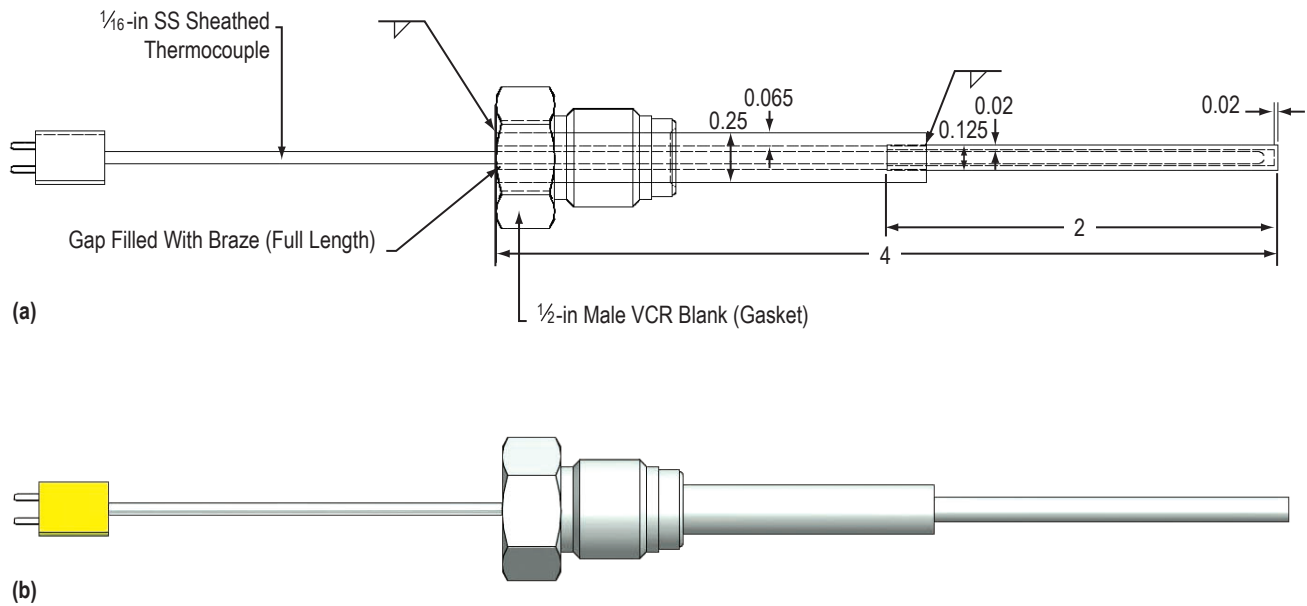
Figure 17. Thermal well assembly: (a) Schematic and (b) rendering.

1/8-in Rod Bored to 0.2-in Wall Thickness and From End

3/4-in Tube 0.065-in Wall

VCR Blank Bored

3/4-in Tube - VCR Blank Weld
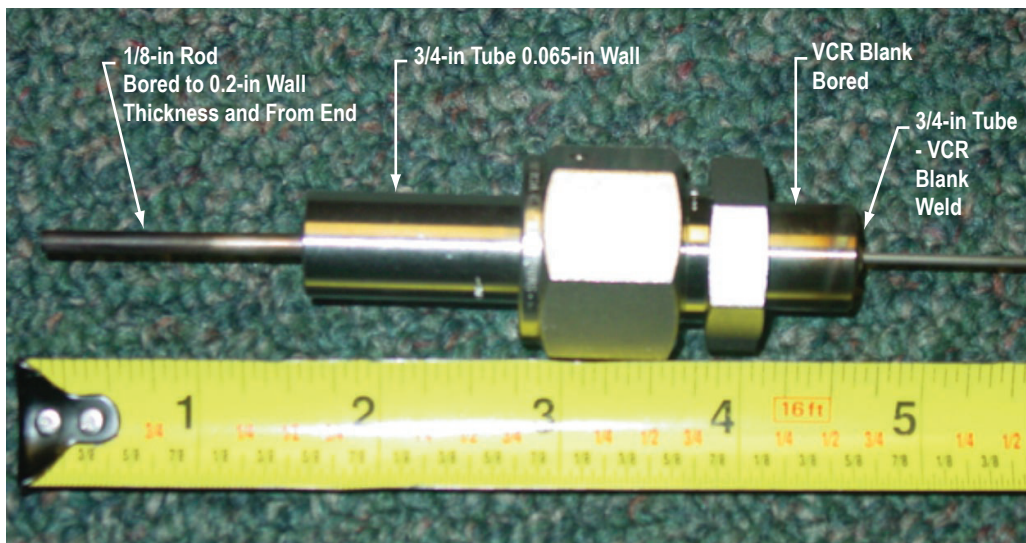
Figure 18. Thermal well as fabricated and mated to a ½-in female VCR gland.

3. PERFORMANCE TEST DATA

Presented in this section are performance measurements obtained during the course of testing. These data consist of volumetric flow rate ($\dot{v}$), pressure rise across the pump (Δp), input power (P_{IN}), and efficiency (η). Efficiency is equal to the fluid power divided by the input electrical power and is given as

$$\eta = \frac{\dot{v}\Delta p}{P_{IN}} \, . \tag{2}$$

The data set spans a range of NaK temperatures from room temperature (25 °C) up to a peak temperature of 525 °C. For this particular pump, the nominal operating frequency (design point) is ≈36 Hz. Data are presented for the pump operating on VFD-supplied, three-phase power at 33, 36, 39, and 60 Hz, and also on standard ac wall power at 60 Hz. The pump was operated over a range of voltage levels from 5 to 120 V ac at the nominal frequency, and over smaller voltage ranges at other frequencies.

Typically, data were acquired by first bringing the pump and loop temperature to a steady-state value. A constant pump voltage was then set using the variac. The throttling valve was exercised through its entire range to obtain pump performance curves over a range of $\dot{v}$ and Δp values.

Before presenting the measured performance data, it is important to note that this pump encountered some issues during the fabrication process that could lead to a lower than expected efficiency. A few of the major issues are summarized as follows: The Cu coil windings were thicker than expected, so fewer coil turns were possible, leading to a magnetic field strength at a given applied current level that was lower than the design value. Also, there is an uncertainty in the magnetic properties of the stators and torpedo. This could be due to low cobalt content of the alloy or improper annealing, either of which could result in reduced magnetic field strength in the channel for a given applied power. As will be shown in the data, the currents supplied to each of the three phases were not equal. This may be due to a short circuit between coils, unbalanced mutual inductance between the different coils, or end effects causing the inductance of each leg to be slightly different. Consequently, while the efficiency of this pump is admittedly lower than was expected, these data should not necessarily be taken as representative of the best possible performance for an ALIP. These issues are detailed and addressed in a companion report.[6]

To demonstrate the remarkably clean nature of the test data, each individual data point over roughly 215 min of testing is plotted in figure 19. These data were acquired at a sampling rate of 1 Hz, a NaK temperature of 325 °C, and an ALIP frequency of 36 Hz. Each line of dots in panel (a) represents operation at a constant pump voltage. Concentrations of data points represent flow conditions measured at steady-state flow conditions while the throttling valve was stationary (roughly 40–60 s dwell time). The individual dots forming the rest of the lines represent data obtained while the valve was transitioning from one setpoint to the next. Each efficiency point was computed using the flow rate (Δp), and input power as measured and recorded on the DAQ system.

20
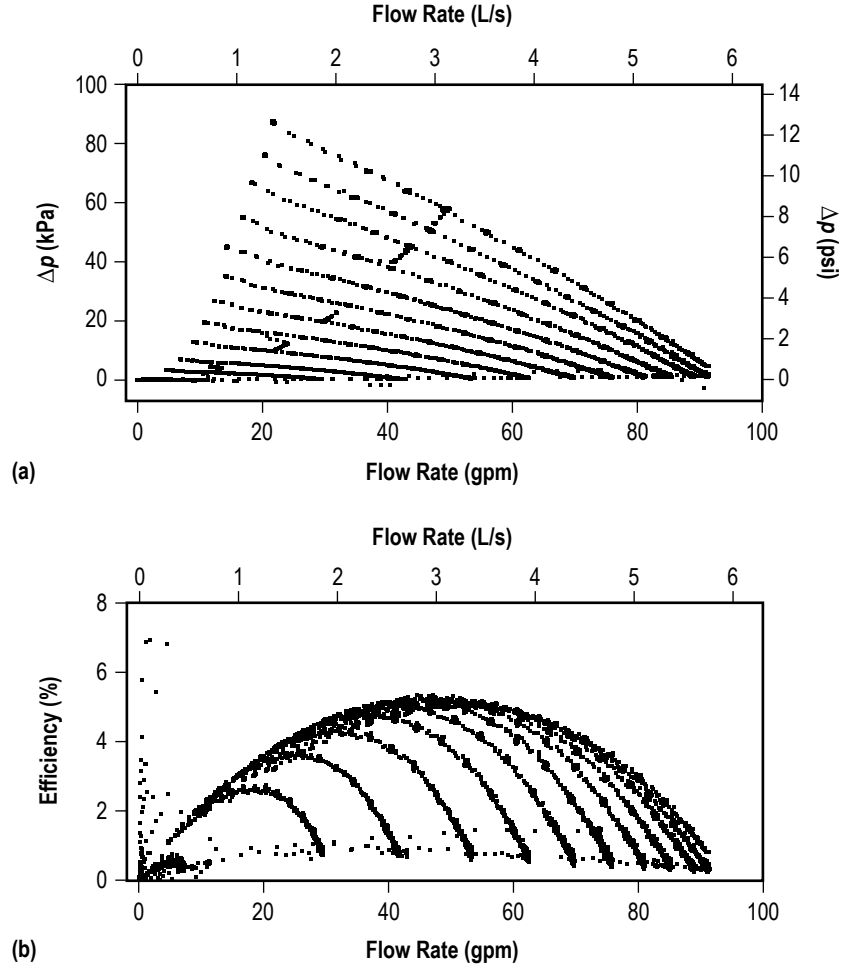
Figure 19. All raw data from operation at a NaK temperature of 325 °C
and a pump frequency of 36 Hz. Data were acquired
at a sampling rate of 1 Hz, and presented as (a) Δp and
(b) efficiency as a function of flow rate.

The data presented in figure 19 were analyzed and are presented as pump performance curves in figure 20. The data were analyzed at steady-state flow conditions. Each curve is labeled with the ALIP operating voltage for that particular performance curve. The error bars on flow rate, Δp, and input power were determined in the manner given in section 2.2.2 and appendices C and D. The error on calculated efficiency is given in the standard manner,[11] assuming no cross correlation between the errors on the three measured parameters. The error bars for the data set are small compared to the magnitude of the measurement. Those on the calculated efficiency are smallest at the highest flow rates and voltages, and grow larger as the flow rate or voltage is reduced. At 5 V, the error bars on efficiency are larger than the calculated value, which is unsurprising given the low values of all three parameters that comprise equation (2). If obtaining a much more accurate measure in this regime was required, the measurements on input power and Δp could be refined to obtain a lower uncertainty on the data.
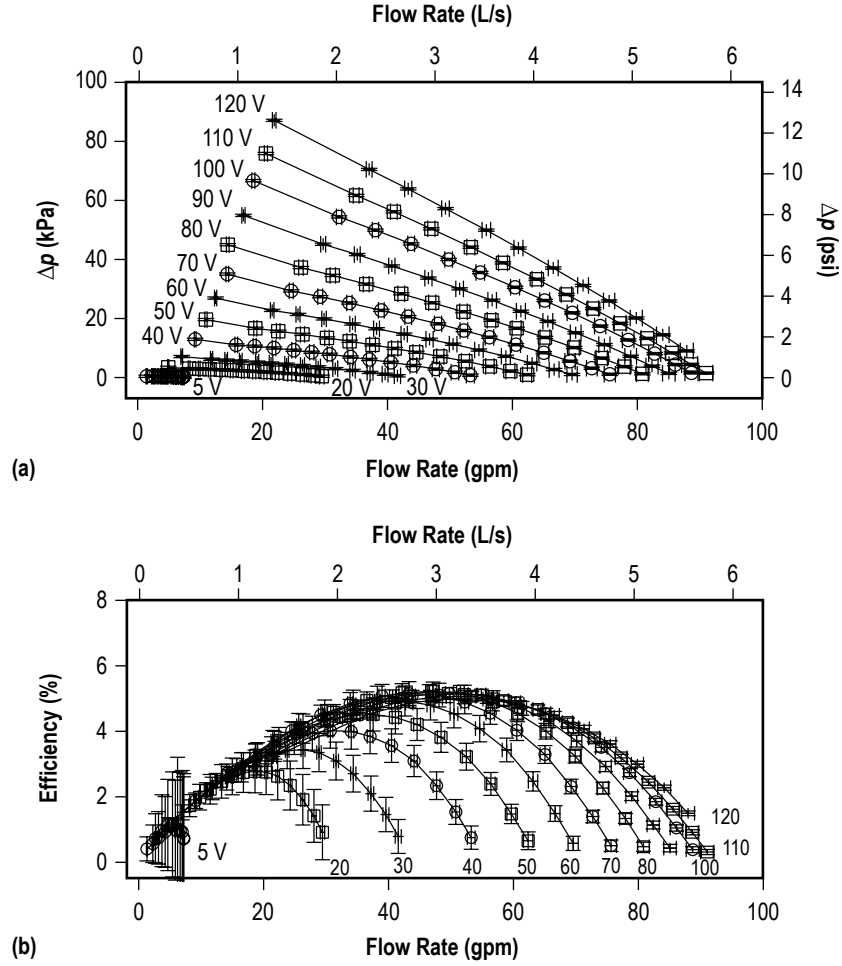
Figure 20. Reduced data from operation at a NaK temperature of 325 °C and a pump frequency of 36 Hz (fig. 19 data). Data presented (with error bars) as (a) Δp and (b) efficiency as a function of flow rate and constant pump voltage.

The Δp data given in figures 19 and 20 represent P-02 minus P-01, located as shown in figure 1. As previously stated, this does not measure the total pressure rise because there is pressure loss associated with the contraction and expansion of the flow at the pump's inlet and outlet, respectively. An analytical correction to account for these pressure losses was developed and is documented in appendix B. The effect of this correction on the Δp measurement is demonstrated on three representative data sets in figure 21. The correction is largest, both in absolute and relative terms, for the highest flow rates, but these corrections do not significantly affect the overall data set. Even though the correction is small, it has been incorporated into the subsequent data presented in this section for the sake of completeness.
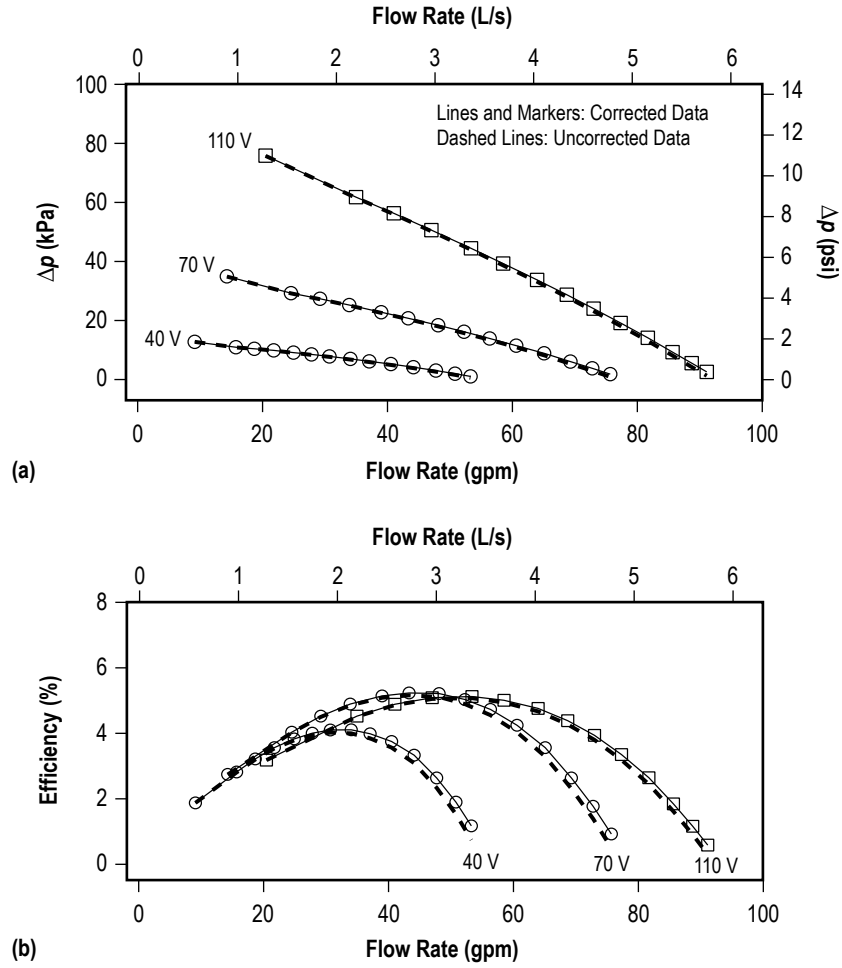
Figure 21. Select constant pump-voltage data from operation at a NaK
temperature of 325 °C and a pump frequency of 36 Hz,
showing the effect of the contraction and expansion corrections
on the (a) Δp measurement and (b) corresponding efficiency
as a function of flow rate.

In figures 22–26, data are presented showing the performance of the pump at different NaK
temperatures for constant applied voltages of 40, 60, 80, 100, and 120 V, respectively. The NaK tem-
peratures were 125, 225, 325, 425, and 525 °C. The trends in the data show that for a constant volt-
age, both the Δp and the efficiency as a function of flow rate shift lower with increasing temperature.

23
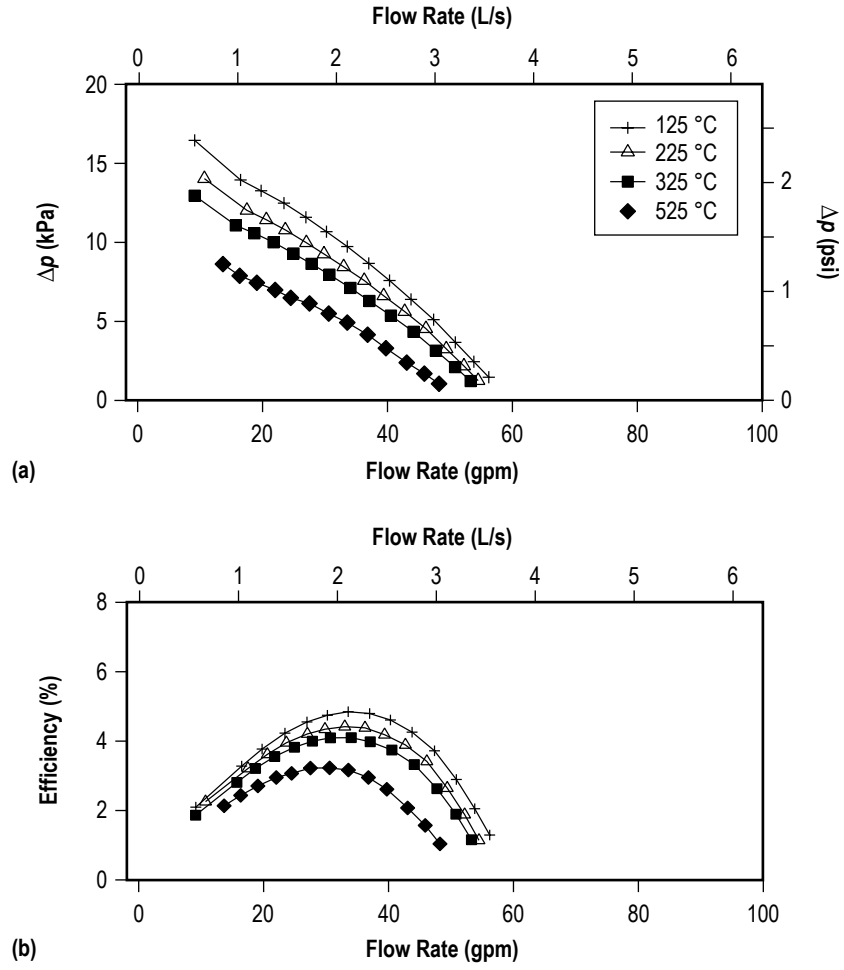
Figure 22. Measured performance curves for pump frequency of 36 Hz
and voltage of 40 V showing (a) Δp and (b) efficiency
as a function of flow rate and NaK temperature.
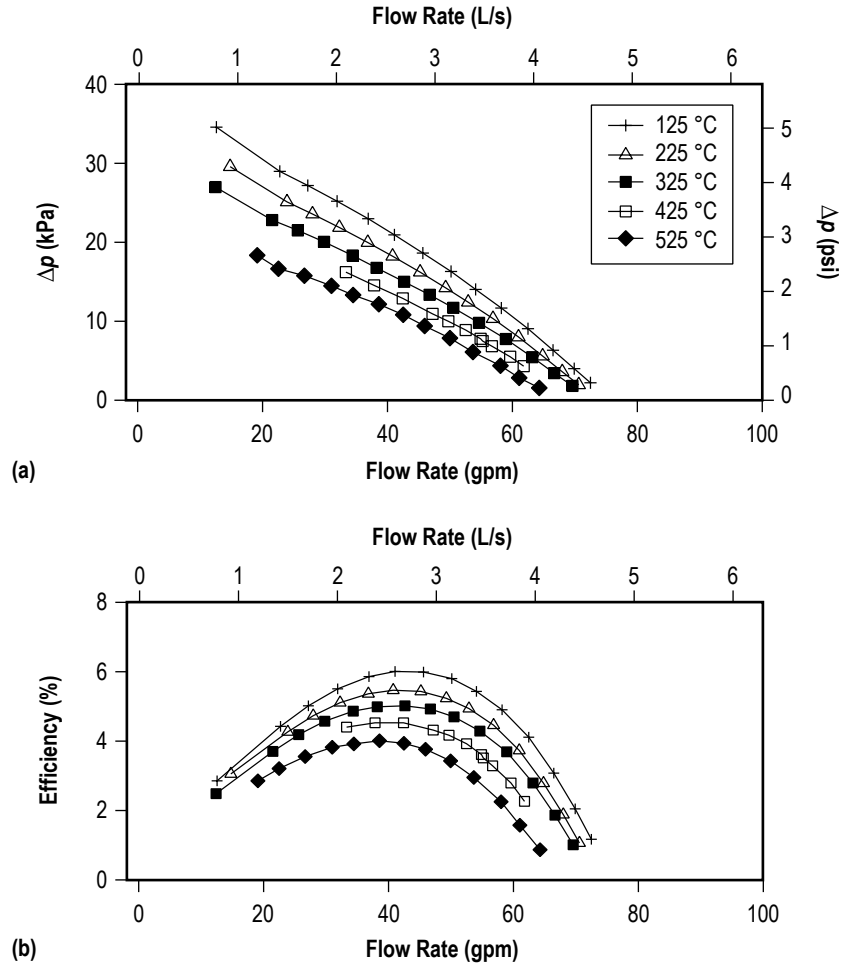
Figure 23. Measured performance curves for pump frequency of 36 Hz
and voltage of 60 V showing (a) Δp and (b) efficiency
as a function of flow rate and NaK temperature.
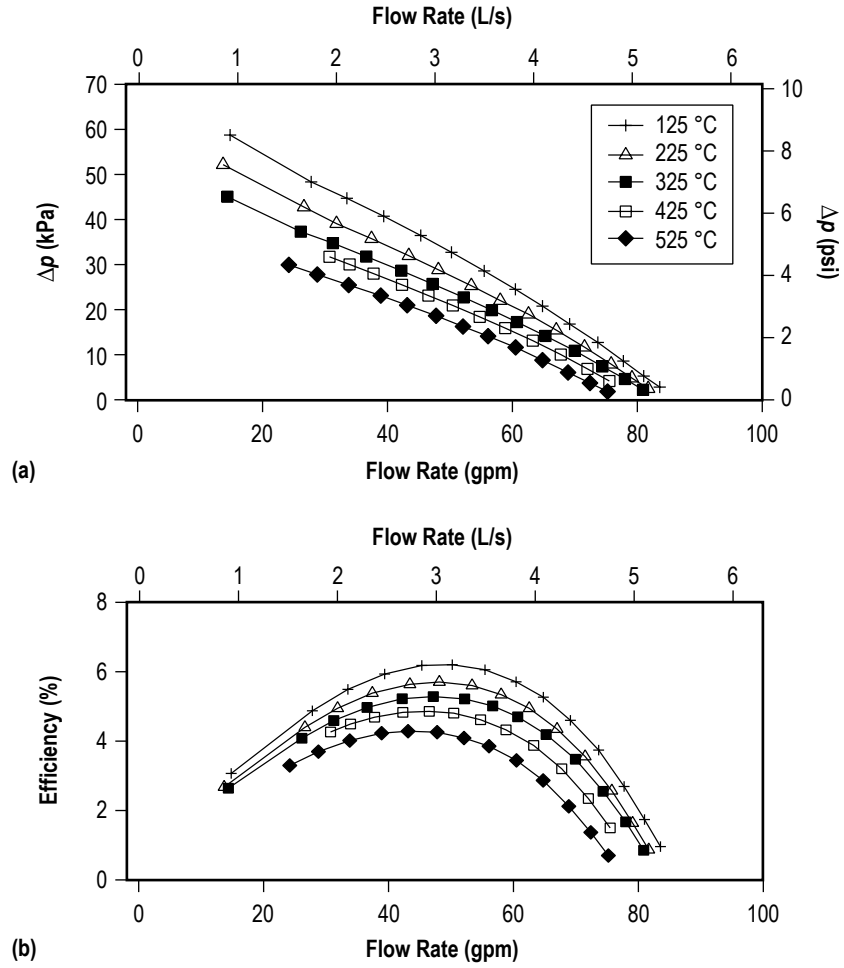
Figure 24. Measured performance curves for pump frequency of 36 Hz
and voltage of 80 V showing (a) Δp and (b) efficiency
as a function of flow rate and NaK temperature.
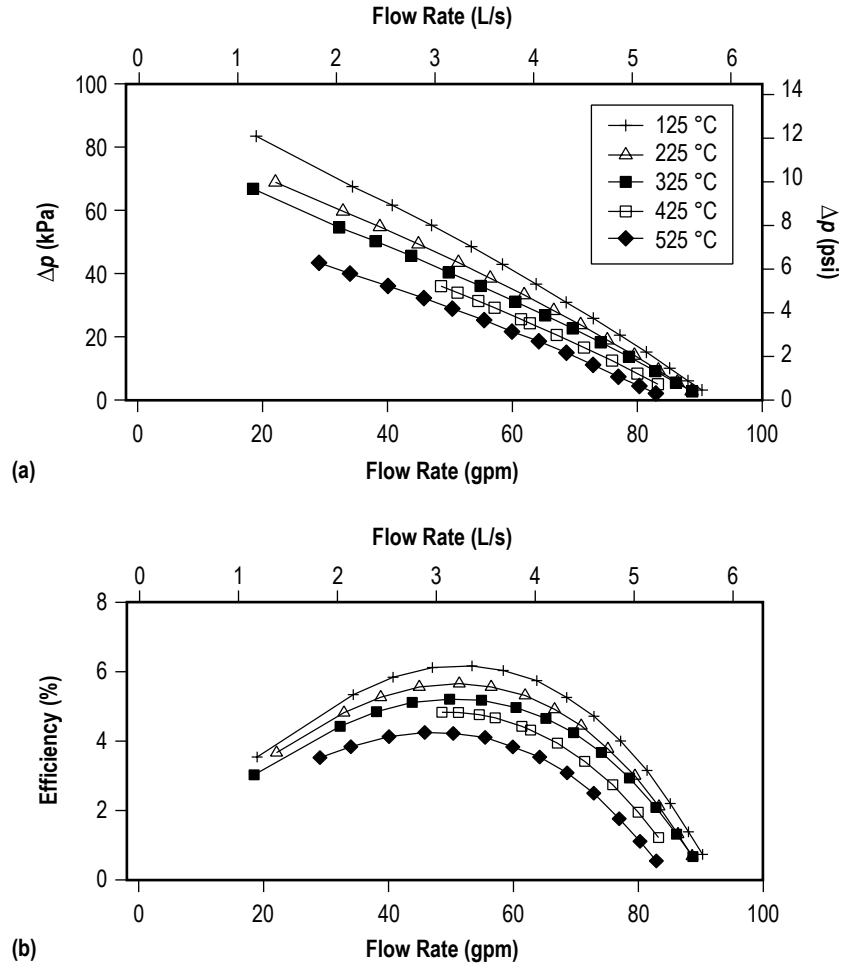
Figure 25. Measured performance curves for pump frequency of 36 Hz
and voltage of 100 V showing (a) Δp and (b) efficiency
as a function of flow rate and NaK temperature.
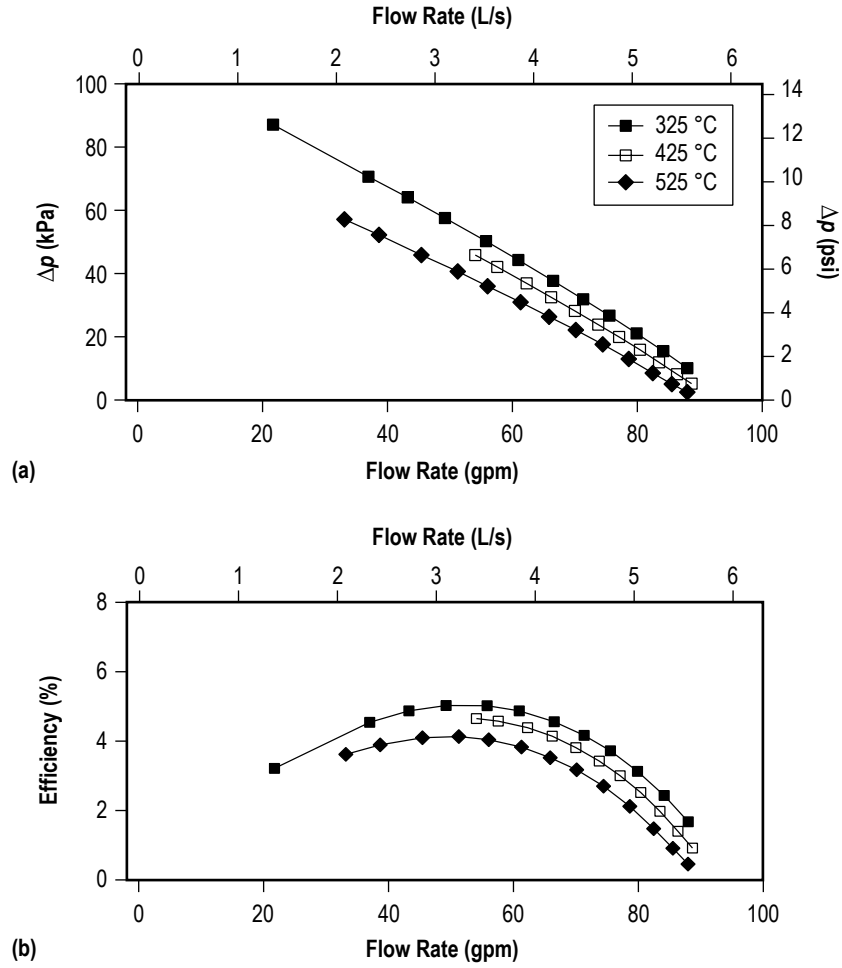
Figure 26. Measured performance curves for pump frequency of 36 Hz
and voltage of 120 V showing (a) Δp and (b) efficiency
as a function of flow rate and NaK temperature.

While constant applied voltage lines are an approximation of constant real power supplied to the pump, they are not, strictly speaking, the same. Consequently, data are plotted in figures 27 and 28 showing efficiency contours as a function of real power and flow rate at constant temperature. These data exhibit an efficiency island in the middle of the plot and show that the peak of this island becomes smaller as the temperature is increased.
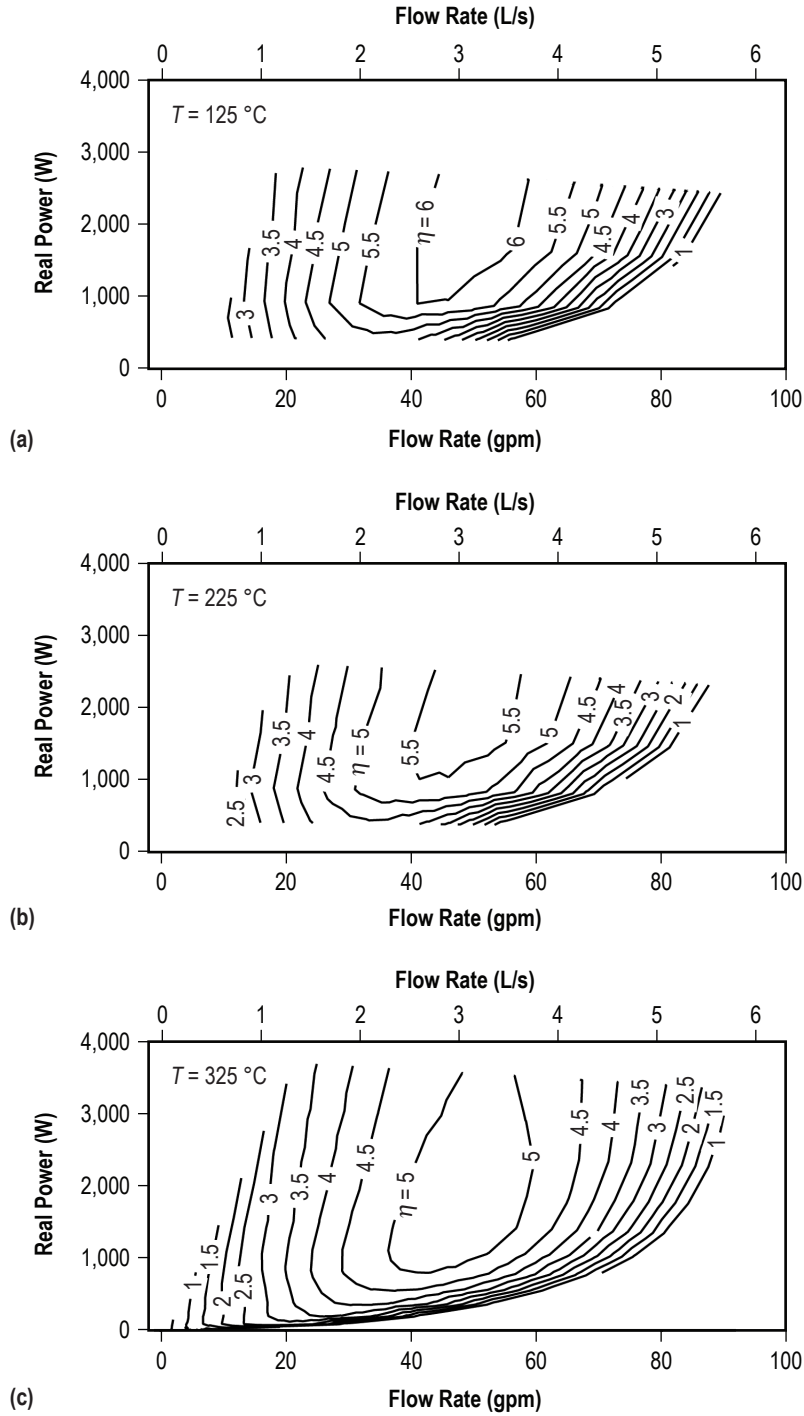
Figure 27. Measured efficiency contour plots from operation
at a pump frequency of 36 Hz as a function
of real power to the pump and flow rate for NaK
temperatures of (a) 125 °C, (b) 225 °C, and (c) 325 °C.
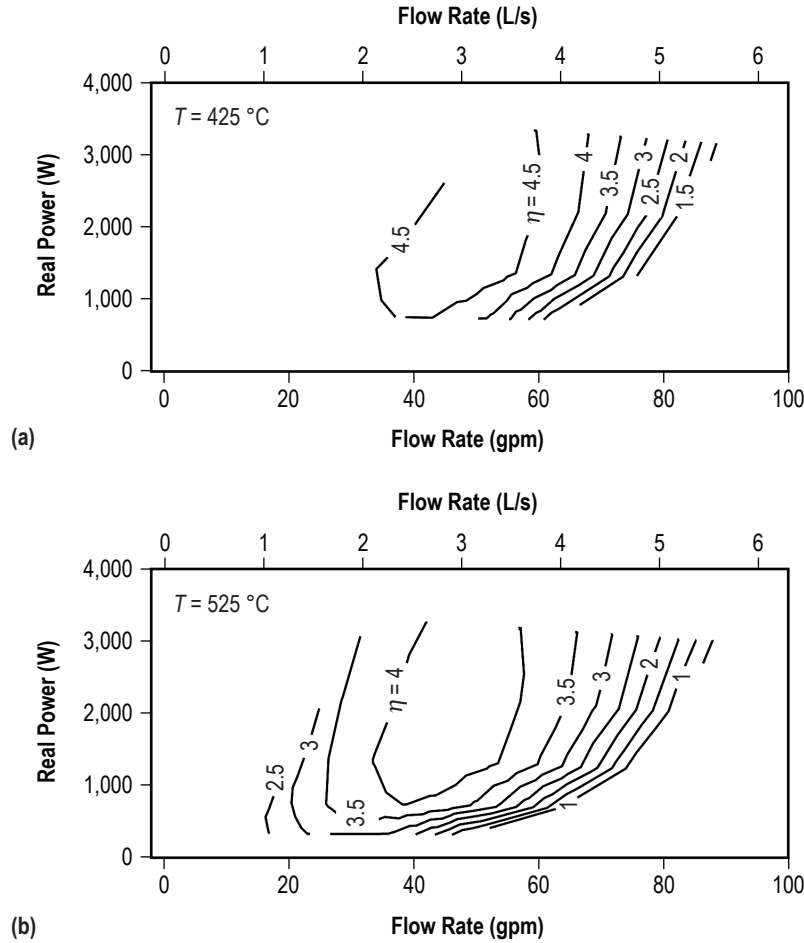
Figure 28. Measured efficiency contour plots from operation at a pump
frequency of 36 Hz as a function of real power to the pump
and flow rate for NaK temperatures of (a) 425 °C and (b) 525 °C.

The effects of changing the applied frequency while operating at a constant voltage (80 V) are explored in figure 29. In this figure, the data obtained at 33, 36, and 39 Hz are similar. The Δp levels deviate slightly at lower flow rates, but the efficiency curves as a function of flow rate are fairly consistent across the data set. (Recall the error bars on the measurement as shown fig. 20.)

As expected, the data obtained while operating at 60 Hz exhibit significantly lower performance than the other data sets. Of particular interest, however, is the comparison between the data obtained at 60 Hz with power supplied by the sine wave filtered VFD (open square symbols) and a pure sinusoidal voltage supplied straight from ac wall power. The data set shows that the approximated sinusoidal current supplied by the VFD compares favorably with the ac-supplied power, serving to validate the use of a pulse width modulated source as a method for supplying arbitrary frequency power. As an interesting side note, the data obtained using the VFD operating at 60 Hz was acquired on the first day of testing, while the data operating straight from ac wall power was obtained on the last day of testing. The favorable comparison between the two data sets provides strong evidence that the pump did not degrade over the course of testing.
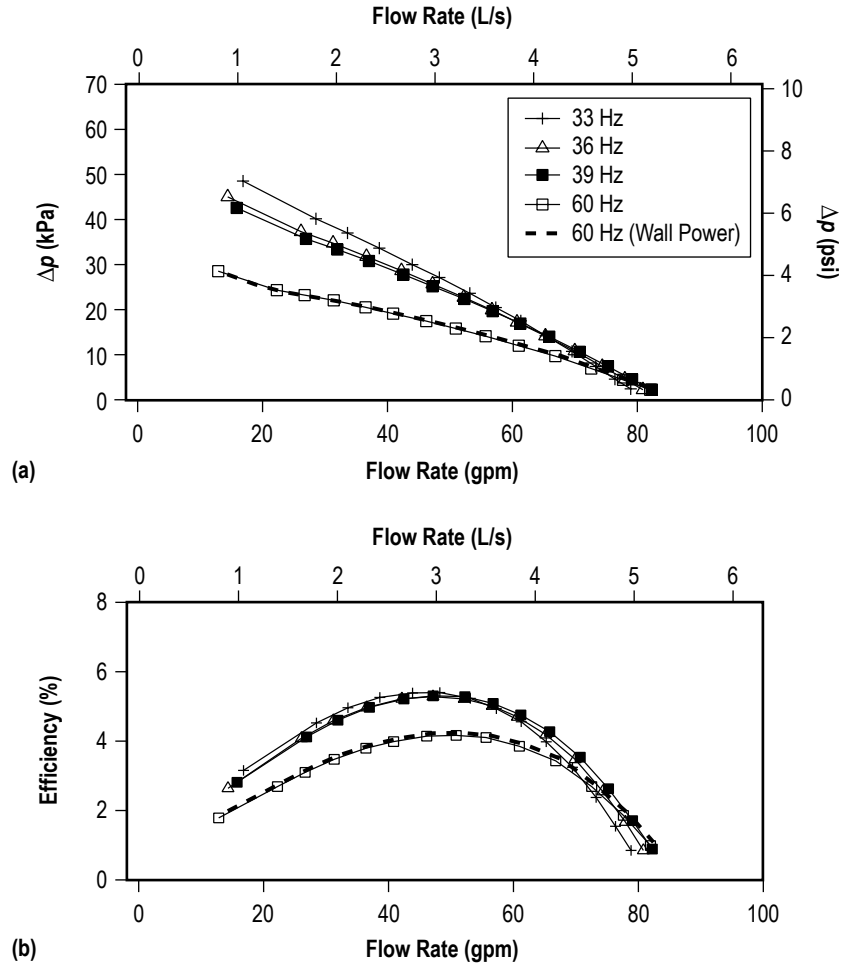
Figure 29. Measured performance curves from operation at a NaK temperature of 325 °C and a pump voltage of 80 V showing (a) Δp and (b) efficiency as a function of flow rate for different displayed pump frequencies. The 'wall power' curve represents operation directly connected to the electrical grid.

Finally, data were acquired at low temperature to measure the performance of the pump under conditions mirroring those encountered before reactor startup, when the fluid is cold and the available power is low. These data are presented in figures 30 and 31 for NaK temperatures of 25 and 75 °C, respectively. In these data sets, the pump was operated at three voltages (10, 20, and 40 V) and two frequencies (36 and 60 Hz). As observed in figure 29, the pump exhibited significantly lower performance at 60 Hz when compared with the 36 Hz. In both figures 30 and 31, the flow rate could be relatively high as the throttling valve was opened, even at low applied voltages. At low voltages, the pump performance curves follow the same pattern as those obtained at higher temperatures and voltages, indicating no fundamental change in operation under these off-nominal conditions.
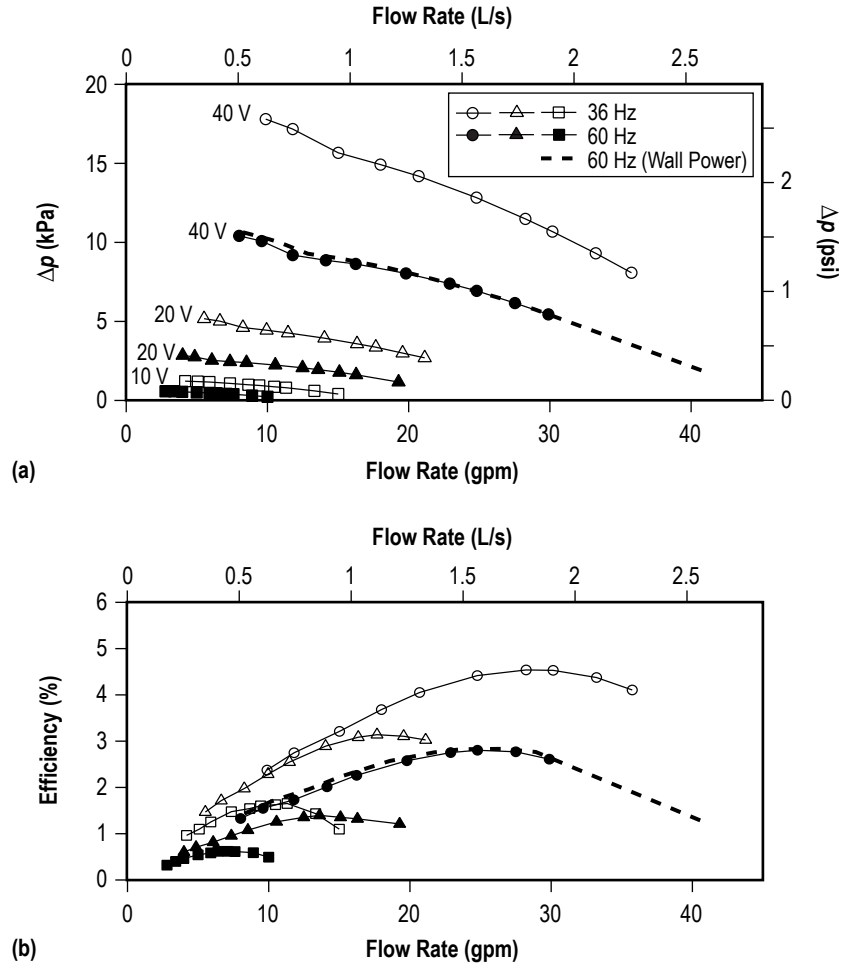
Figure 30. Measured performance curves from operation at a NaK temperature of 25 °C and pump voltages of 10, 20, and 40 V showing (a) Δp and (b) efficiency as a function of flow rate for different displayed pump frequencies. The 'wall power curve' represents operation directly connected to the electrical grid.
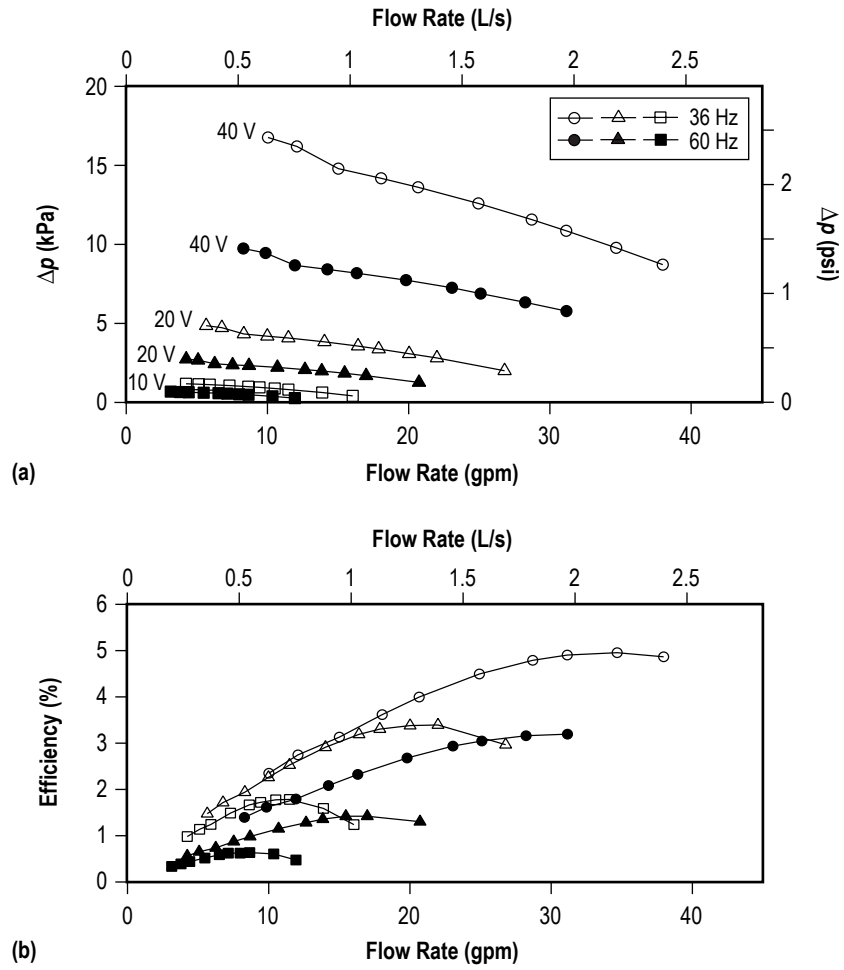
Figure 31. Measured performance curves from operation at a NaK
temperature of 75 °C and pump voltages of 10, 20, and 40 V
showing (a) Δ*p* and (b) efficiency as a function of flow rate
for different displayed pump frequencies.

4. ADDITIONAL TEST DATA

Nonperformance test data obtained during the course of this test series include measurements of the transient responses of parameters in the ATC, ALIP input power, NaK temperatures as compared to ALIP temperatures, thermal well measurements as compared to clamp-on temperature measurements, and the internal magnetic field in the ALIP flow channel.

4.1 Transient Data

An aspect of interest for the ALIP is the response of the fluid under transient conditions. This was tested by suddenly cutting the power to zero, waiting for a period of time for all the parameters to settle to their zero-flow values, and then ramping the power back to a nonzero value. Data showing the pump input power, volumetric flow rate, and pressure change across the pump for one of these sequences is presented in figure 32.
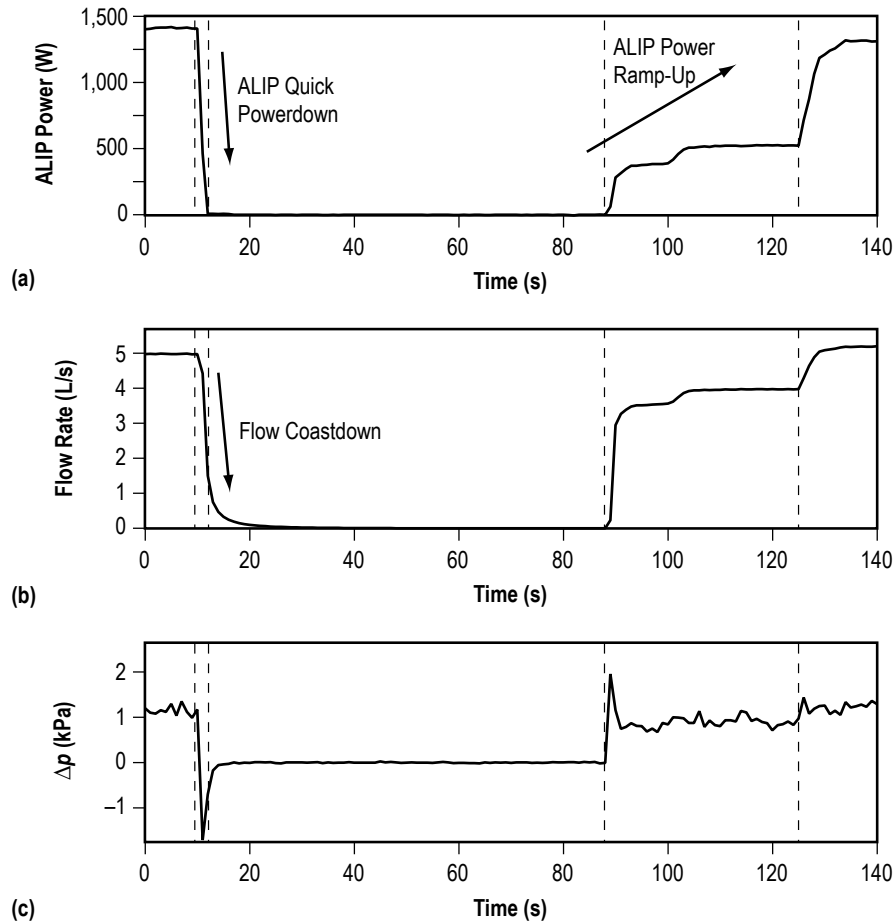
Figure 32. Data showing (a) pump input power, (b) volumetric flow rate, and (c) pressure change as a function of time during transients in pump operation.

When the power is reduced to zero, a negative pressure gradient is induced across the pump, immediately slowing the flow rate. After 10–15 s, the flow rate has essentially dropped to zero. When power is reapplied to the loop, the flow rate and pressure immediately respond. Most interestingly, when there is no external power applied to the pump, the fluid slowdown is somewhat gradual as the process is controlled only through the NaK's own inertia and viscous forces in the loop. However, the flow rate tracks the input power level one-for-one when active electromagnetic pumping is applied to the loop.

4.2 Annular Linear Induction Pump Electrical Measurements

The ALIP was connected in the manner illustrated in figure 33. Phase-to-phase voltage measurements and phase current measurements were performed on all input phases as indicated. The input voltages presented in figure 34 are representative samples shown to demonstrate the fidelity of the measurement only. Panel (a) shows the V_{AB} phase-to-phase voltage when the VFD was employed. Panel (b) shows all three voltages when 60 Hz wall power was applied to the ALIP. For clarity, only one of the phase-to-phase voltages at 36 and 60 Hz is shown in panel (a), but all three were measured and, other than being out of phase by 120 deg, they were virtually indistinguishable from each other. This is also the case when true sinusoidal 60 Hz power (wall power) is applied to the pump. At some frequencies, the voltage sine wave-filtered waveforms delivered by VFD deviate more from a true sinusoid than those for other frequencies (36 Hz compared to 60 Hz in fig. 34 (a)).

(a) ALIP (Aft Looking Forward)   (b) Electrical/Measurements Diagram
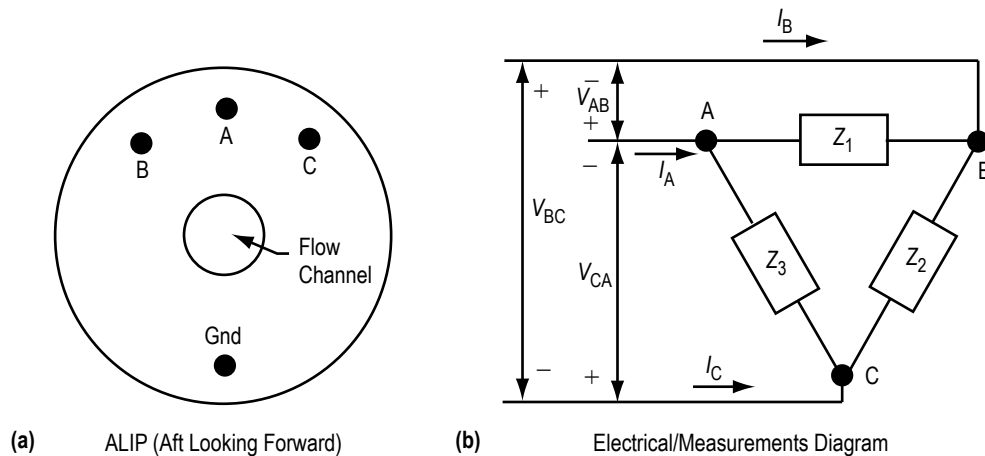
Figure 33. Illustration showing the naming convention for (a) the ALIP electrical connections and (b) an electrical schematic of how the ALIP was connected and where each differential voltage and current was measured.
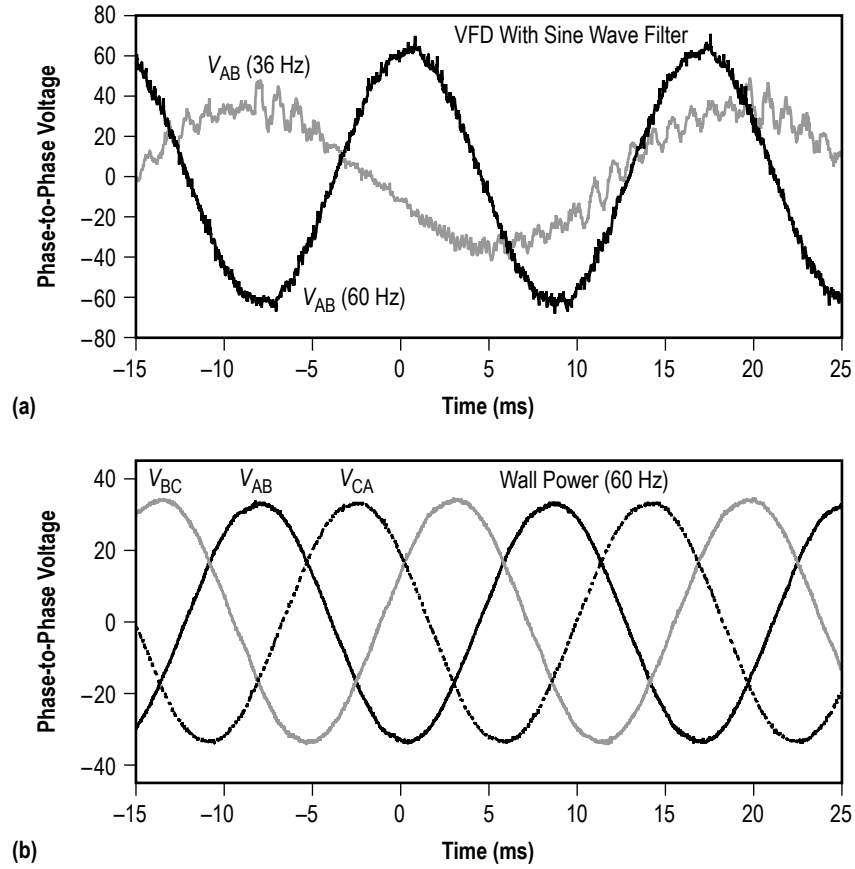
Figure 34. Phase-to-phase voltage: (a) Single phase-to-phase (V_{AB})
input voltage measurements acquired while the pump
was powered using the VFD through the sine wave filter
and (b) all three phase-to-phase input voltages acquired
when operating from the electrical grid wall power.

Measurements of the current in each input leg are presented in figure 35, with the three phase currents obtained while operating at 36 Hz using the VFD shown in panel (a) and the same measurements performed at 60 Hz sinusoidal power input shown in panel (b). The data indicate that the VFD is performing well in producing a low-noise approximation of a sinusoidal input current. More importantly, the currents in I_A, I_B, and I_C are not equal. For a given voltage input, I_B is always greatest while I_A is always the smallest with I_C falling in between. A fairly universal result is that the peak value of I_A is roughly 12.5%–13.5% smaller than the value of I_B.
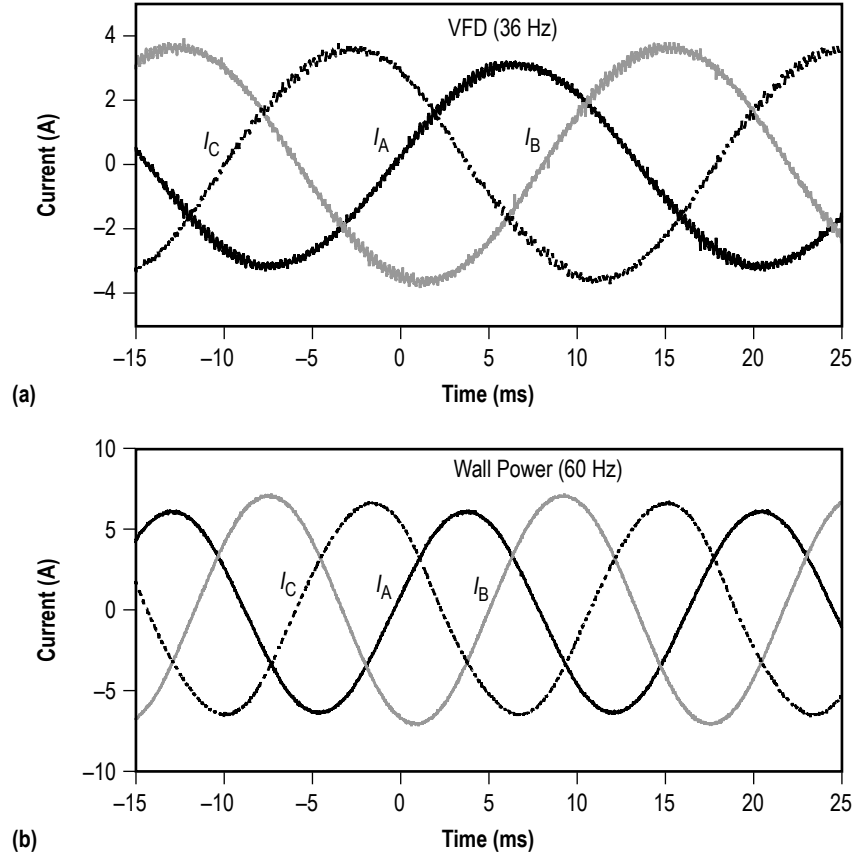
Figure 35. Input current measurements for each phase acquired (a) while
the pump was powered using the VFD through the sine wave
filter and (b) when operating from the electrical grid wall power.

4.3 Temperature Measurements

The temperature of the fluid entering the ALIP compared with thermocouple measurements inside the ALIP are presented in figure 36. These data show the entire thermal time history of the test series at 325 °C. The heating phase from room temperature to 325 °C lasted until ≈13,000 s into the test, and the testing itself lasted until ≈28,000 s. The NaK and ALIP temperatures appeared to be well-coupled, all varying in roughly the same manner. An enlarged view of the heating phase is presented in figure 37, showing all four internal ALIP thermocouple measurements compared with the NaK temperature.

A comparison was also performed between the measurements obtained using the thermal wells and those mounted in a Cu block clamped to the pipe. In these data, the thermal wells always measured slightly higher temperatures than the clamp-on thermocouples, which one would expect based on heat transfer through the thermal boundary layer and the pipe. This difference varied from location to location and ranged from 3 to 10 °C. In addition, clamp-on thermocouples were 30–60 s slower in responding to thermal transients in NaK temperature variations. These observations lead to the conclusion that a thermal well is desirable in situations where accurate measurements of fluid temperatures are required (e.g., performing power balances).

37
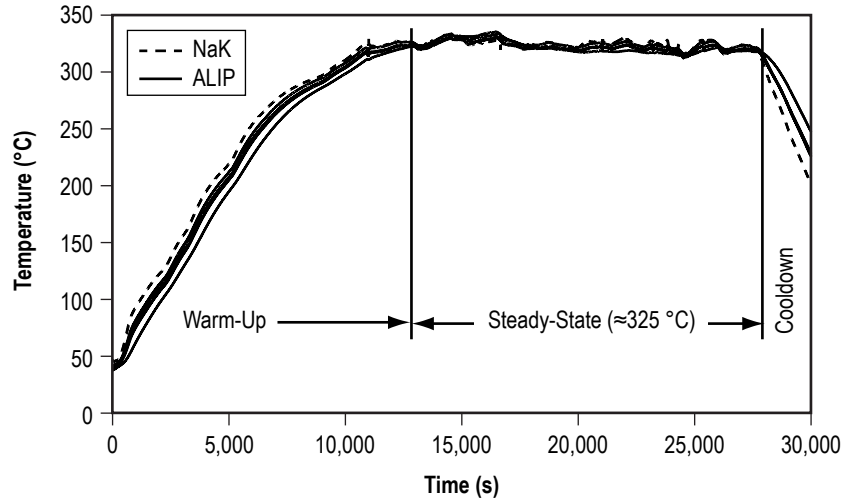
Figure 36. Time history showing temperature measurements of the NaK
at the ALIP entrance and the internal ALIP temperature
measurements.
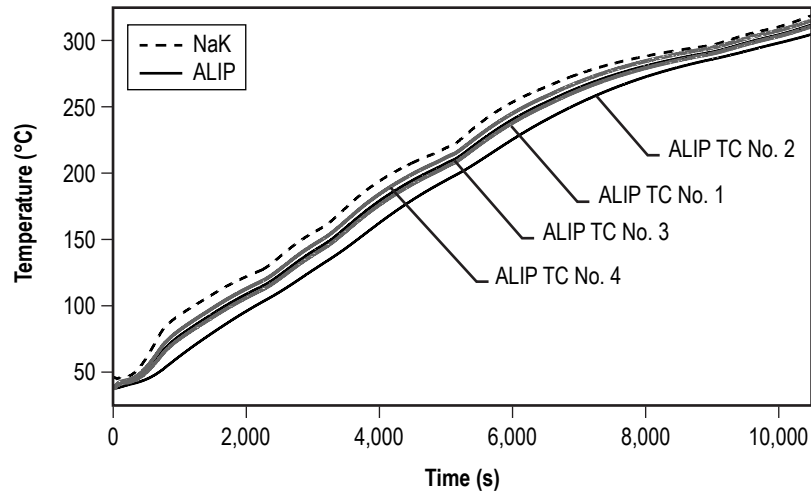
Figure 37. An enlarged view of the heating phase in figure 36
showing all four internal ALIP temperature measurements
as compared with the NaK temperature measurements.

4.4 Internal Electromagnetic Field Mapping

A custom-fabricated, two-axis Hall probe was used to map the time-varying magnetic field inside the ALIP annular flow channel. Details of this probe's construction and calibration are given in appendix E. Figures 38–49 are plots of the radial and axial magnetic field components as the phase current varies in time. The magnetic field plots have been accurately scaled to the ALIP drawing shown in panel (a) of the time slice images, providing full spatial and temporal representation of the field variation throughout the course of one cycle of the phase current. The phase current in one of the coils is given in panel (d) of the figures, and a dark vertical line is used to indicate which time slice of data is being displayed in the magnetic field graphs. A right-traveling sinusoidal magnetic field is observed in B_r, with the local peaks found on both the B_r and B_z data corresponding to locations where the field is concentrated by the stators. When installed in the ATC, the NaK flow through the pump is right to left (as opposed to the left-to-right direction of the traveling wave in the figures), indicating that wires for two of the phases were swapped when performing the field mapping exercise.

(a)

(b)

(c)

(d)

Figure 38. ALIP image (a) on the same scale as (b) and (c), (b) radial (B_r) and (c) axial (B_z) magnetic field measurements at time t=0 ms, displayed as a function of axial position in the channel. (d) Phase current displayed with a dark vertical line showing the instant of time.

(a) B_r ↑ → B_z

(b)

(c)

(d)

Figure 39. ALIP image (a) on the same scale as (b) and (c), (b) radial (B_r) and (c) axial (B_z) magnetic field measurements at time $t=3$ ms, displayed as a function of axial position in the channel. (d) Phase current displayed with a dark vertical line showing the instant of time.

(a)

(b)

(c)

(d)
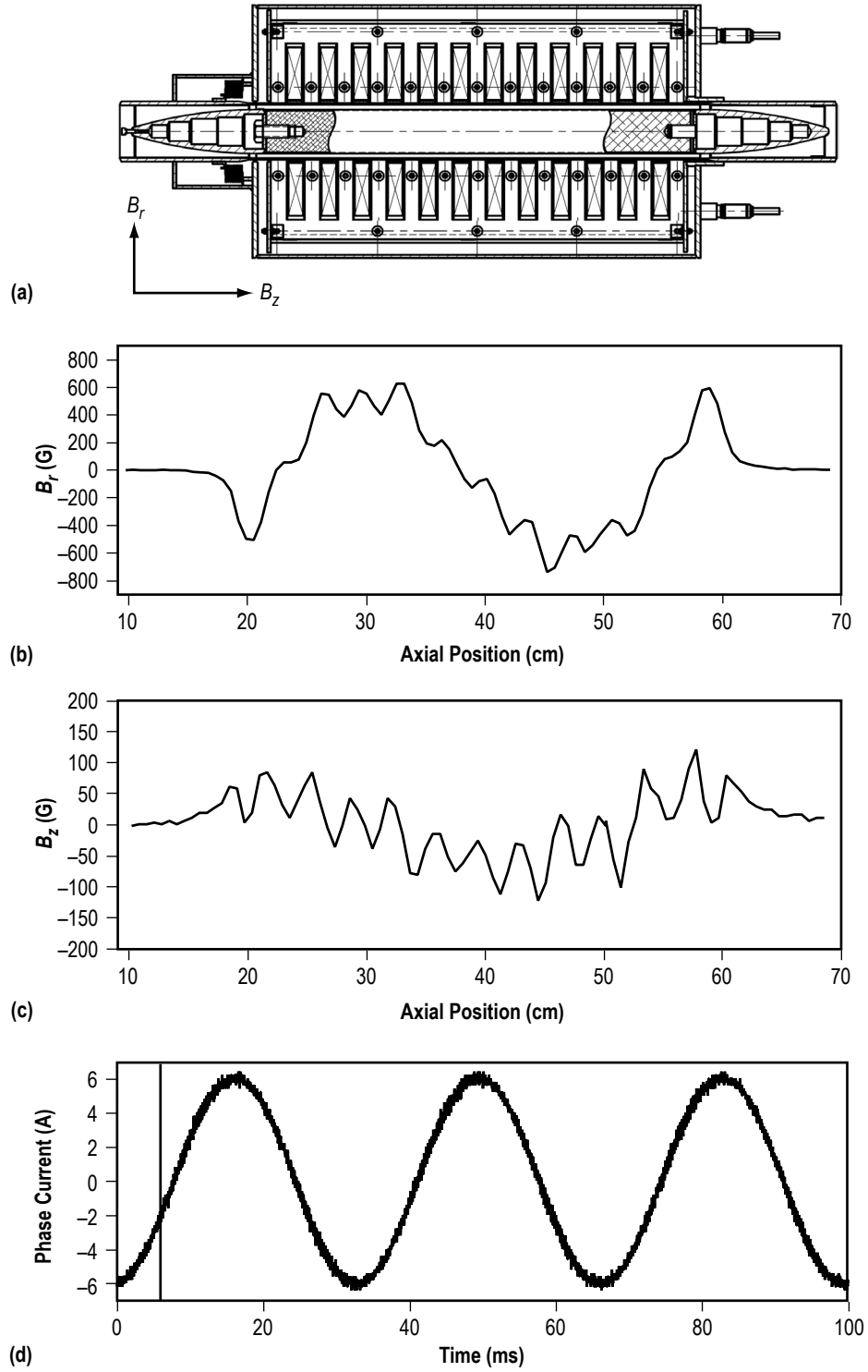
Figure 40. ALIP image (a) on the same scale as (b) and (c), (b) radial (B_r) and (c) axial (B_z) magnetic field measurements at time $t=6$ ms, displayed as a function of axial position in the channel. (d) Phase current displayed with a dark vertical line showing the instant of time.

(a)

(b)

(c)

(d)
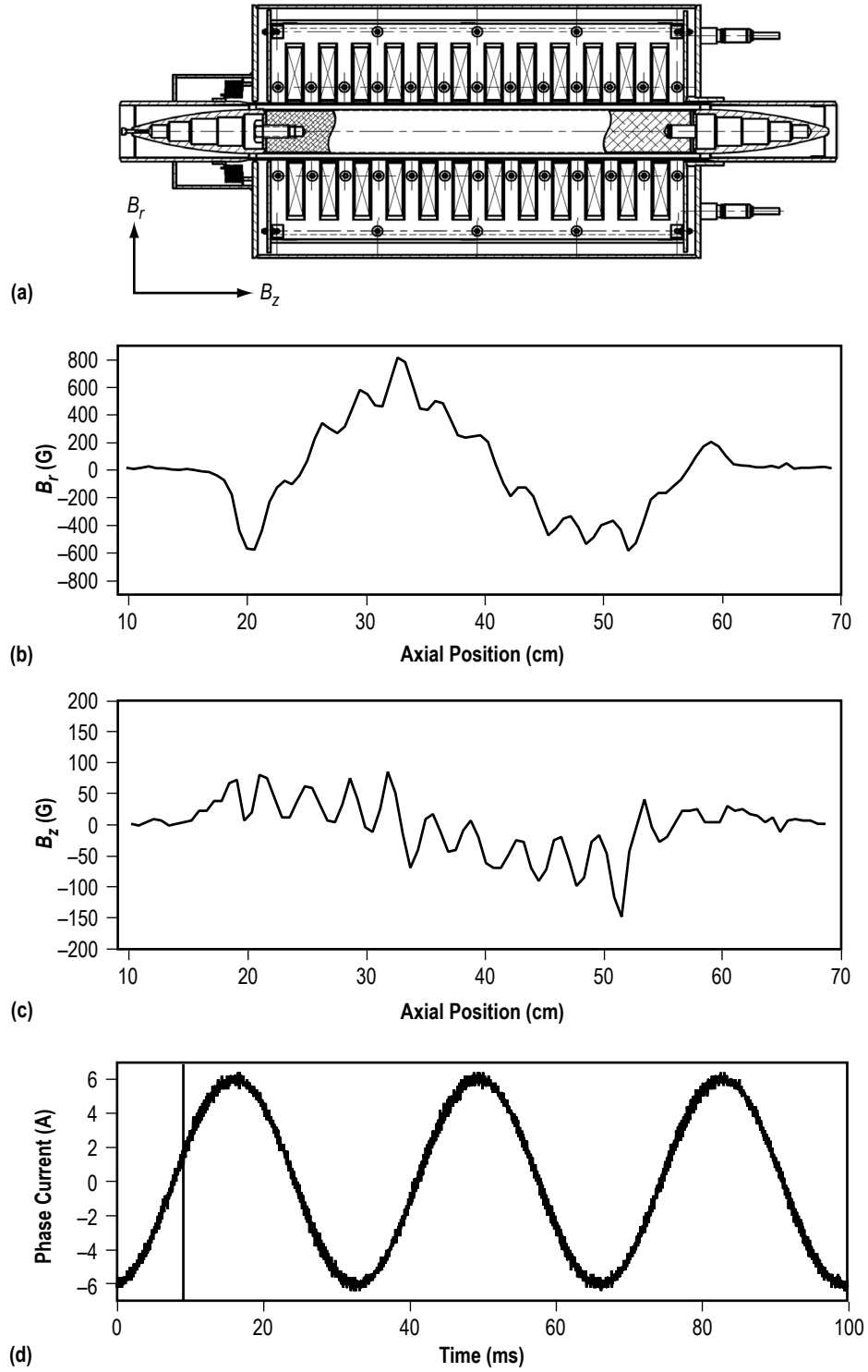
Figure 41. ALIP image (a) on the same scale as (b) and (c), (b) radial (B_r) and (c) axial (B_z) magnetic field measurements at time $t=9$ ms, displayed as a function of axial position in the channel. (d) Phase current displayed with a dark vertical line showing the instant of time.

43

(a)

(b)

(c)

(d)
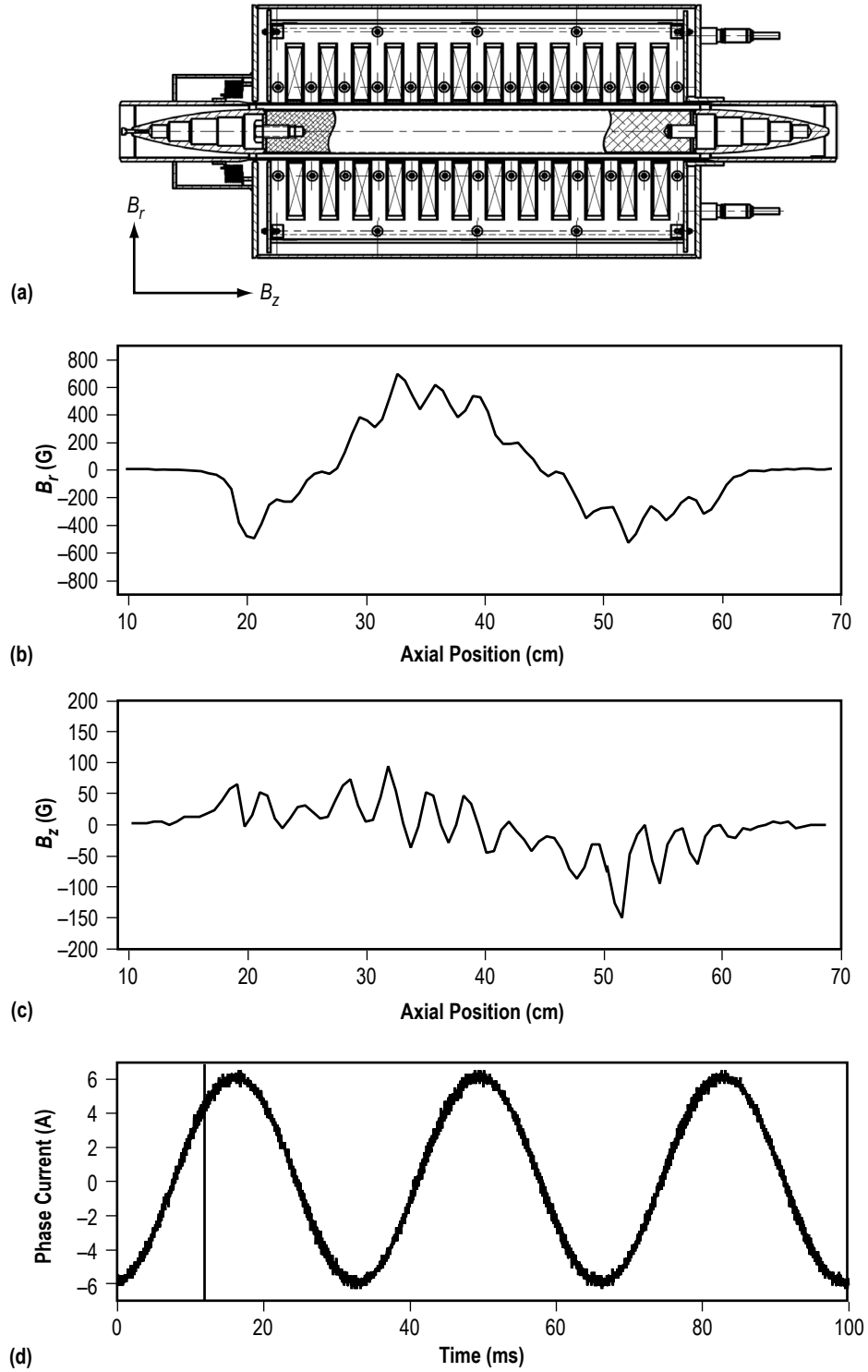
Figure 42. ALIP image (a) on the same scale as (b) and (c), (b) radial (B_r)
and (c) axial (B_z) magnetic field measurements at time $t=12$ ms,
displayed as a function of axial position in the channel. (d) Phase
current displayed with a dark vertical line showing the instant of time.

(a)

(b)

(c)

(d)
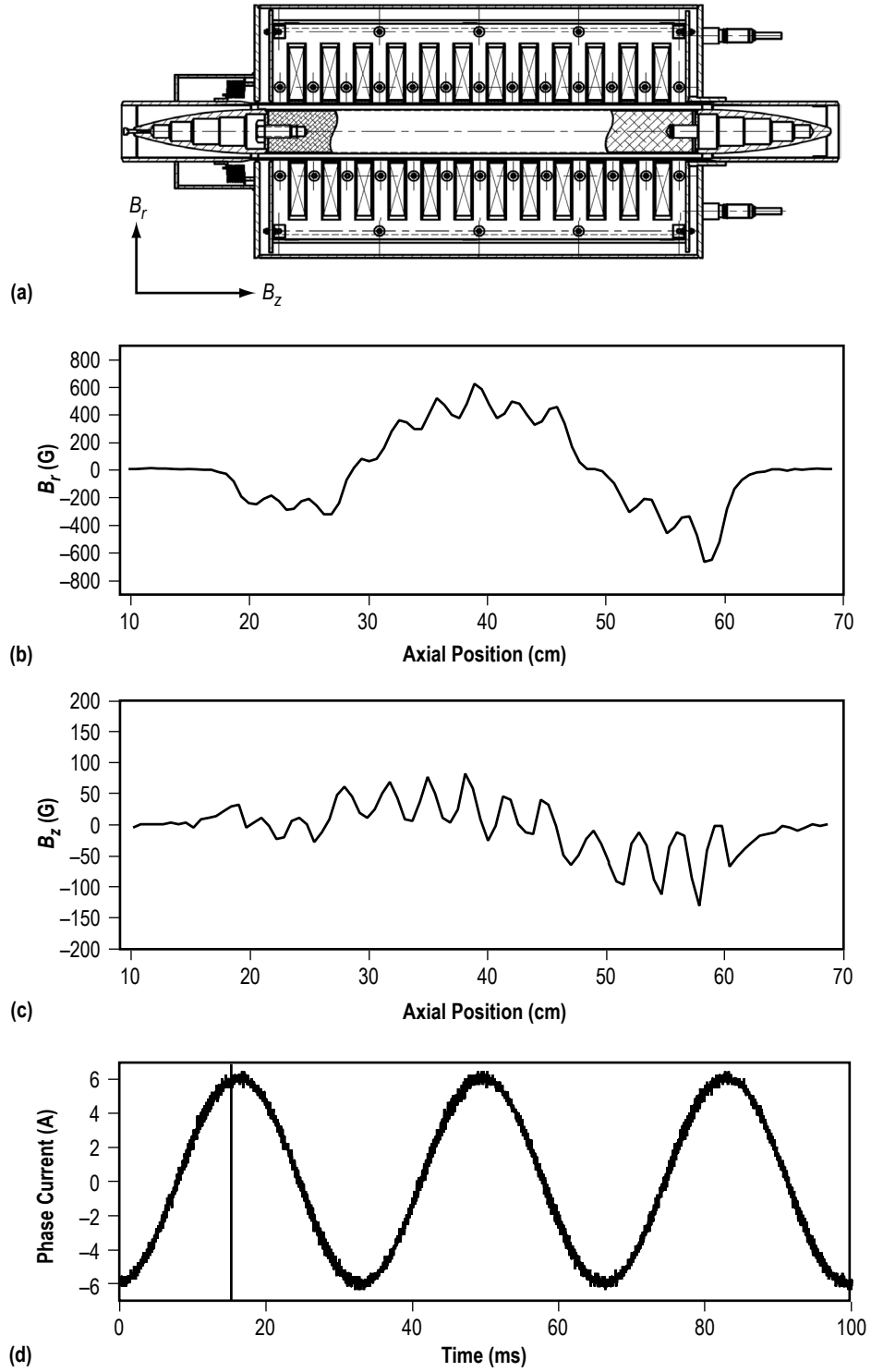
Figure 43. ALIP image (a) on the same scale as (b) and (c), (b) radial (B_r) and (c) axial (B_z) magnetic field measurements at time t=15 ms, displayed as a function of axial position in the channel. (d) Phase current displayed with a dark vertical line showing the instant of time.

(a)

(b)

(c)

(d)
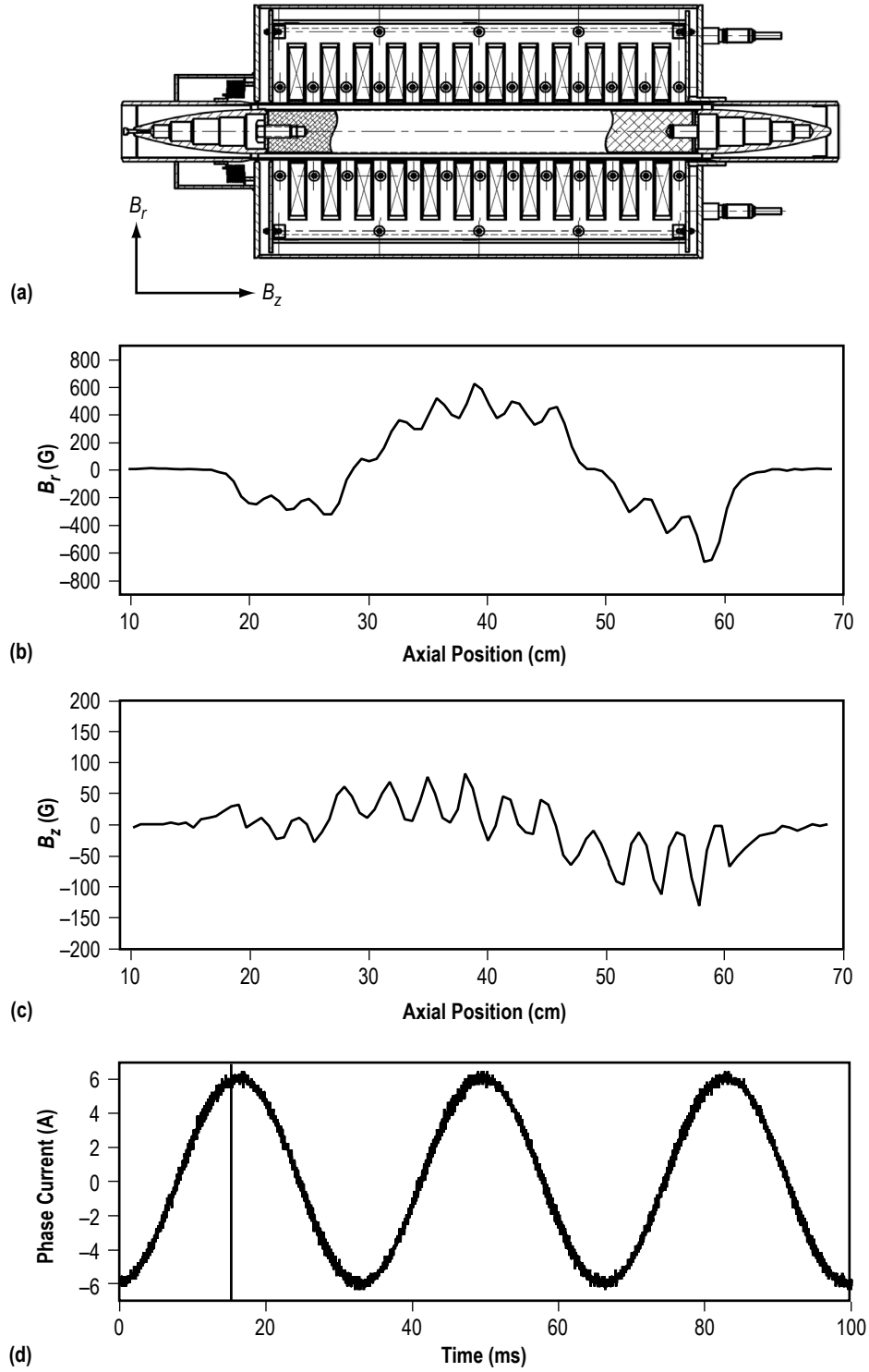
Figure 44. ALIP image (a) on the same scale as (b) and (c), (b) radial (B_r) and (c) axial (B_z) magnetic field measurements at time t=18 ms, displayed as a function of axial position in the channel. (d) Phase current displayed with a dark vertical line showing the instant of time.

(a)

(b)

(c)

(d)
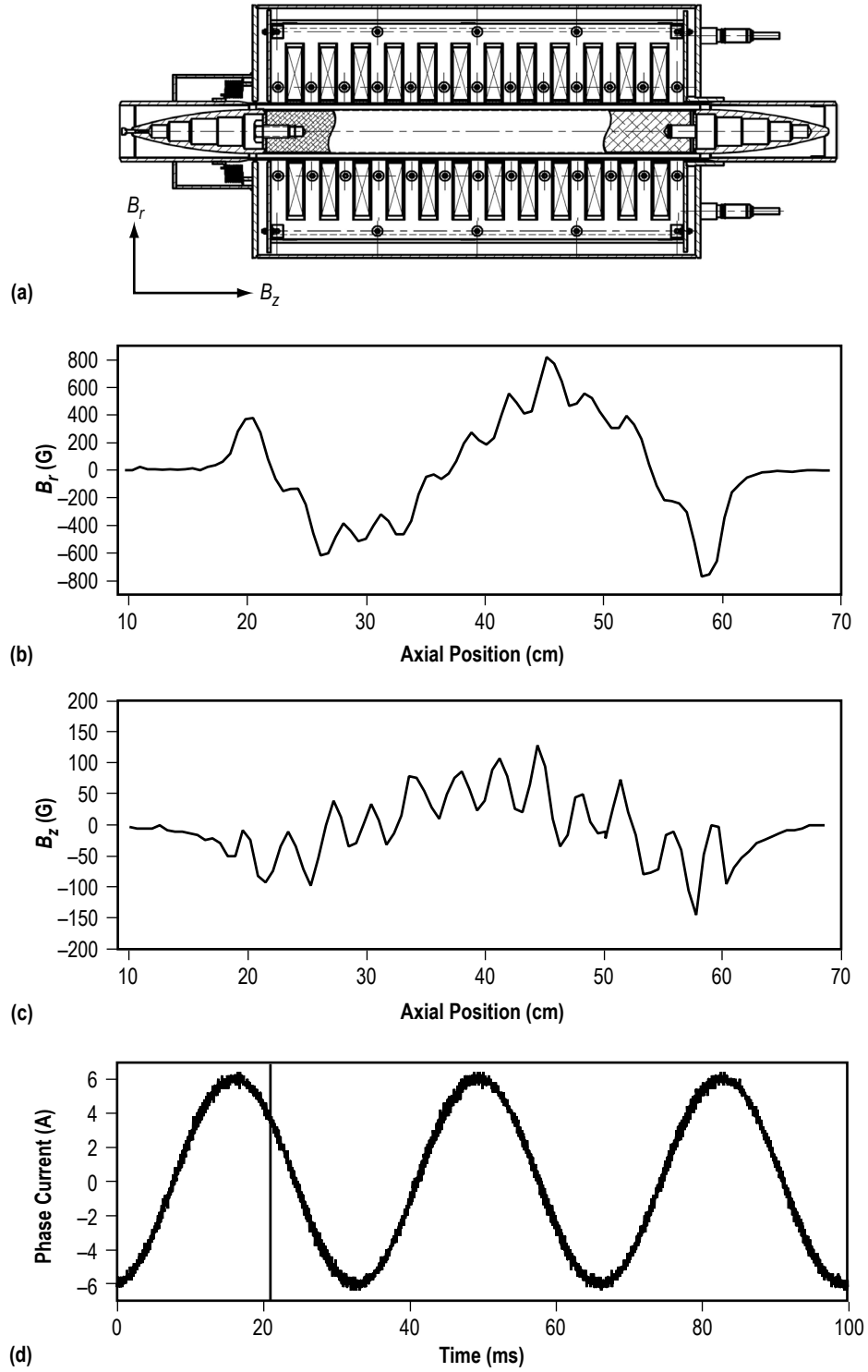
Figure 45. ALIP image (a) on the same scale as (b) and (c), (b) radial (B_r)
and (c) axial (B_z) magnetic field measurements at time $t=21$ ms,
displayed as a function of axial position in the channel. (d) Phase
current displayed with a dark vertical line showing the instant of time.

(a)

(b)

(c)

(d)
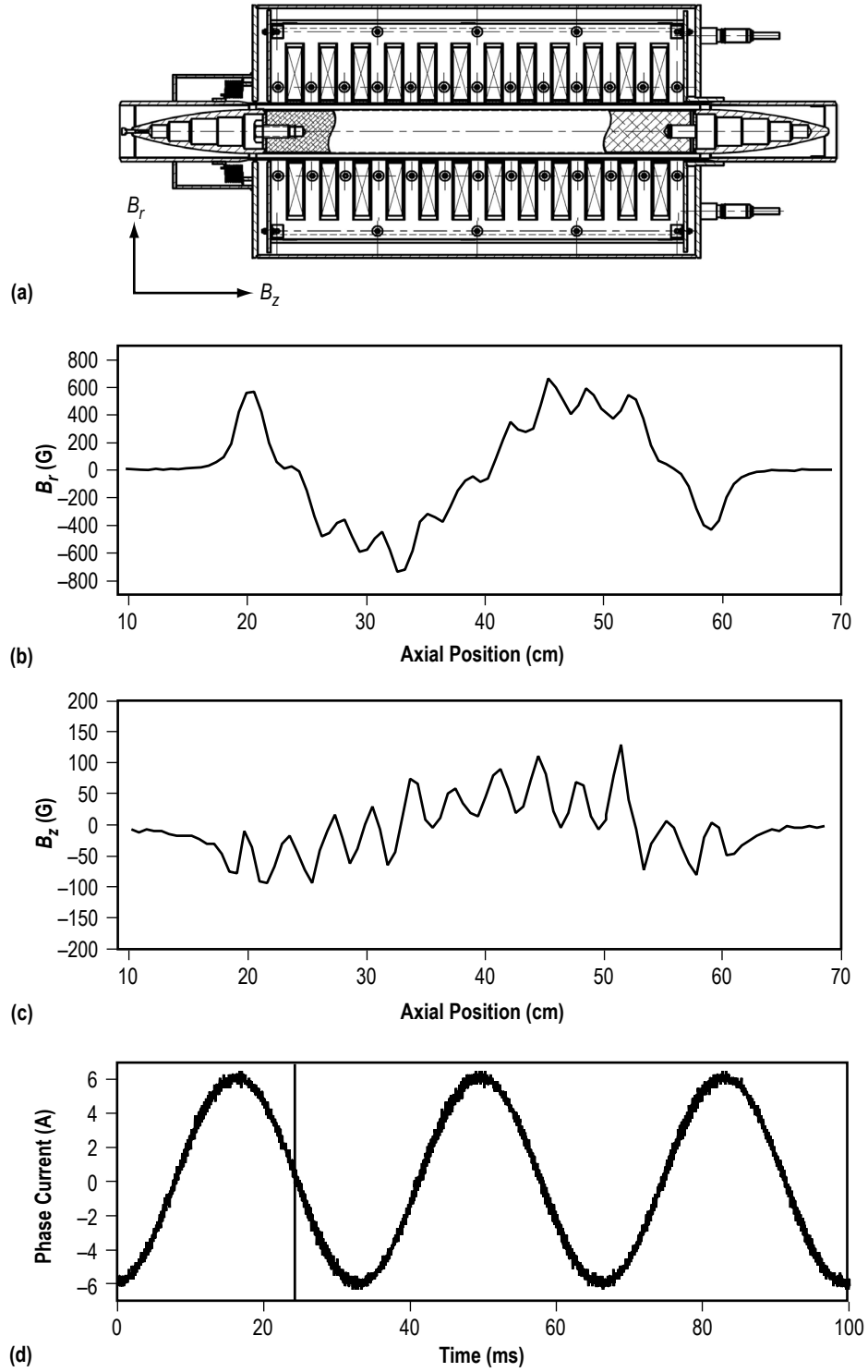
Figure 46. ALIP image (a) on the same scale as (b) and (c), (b) radial (B_r) and (c) axial (B_z) magnetic field measurements at time $t=24$ ms, displayed as a function of axial position in the channel. (d) Phase current displayed with a dark vertical line showing the instant of time.
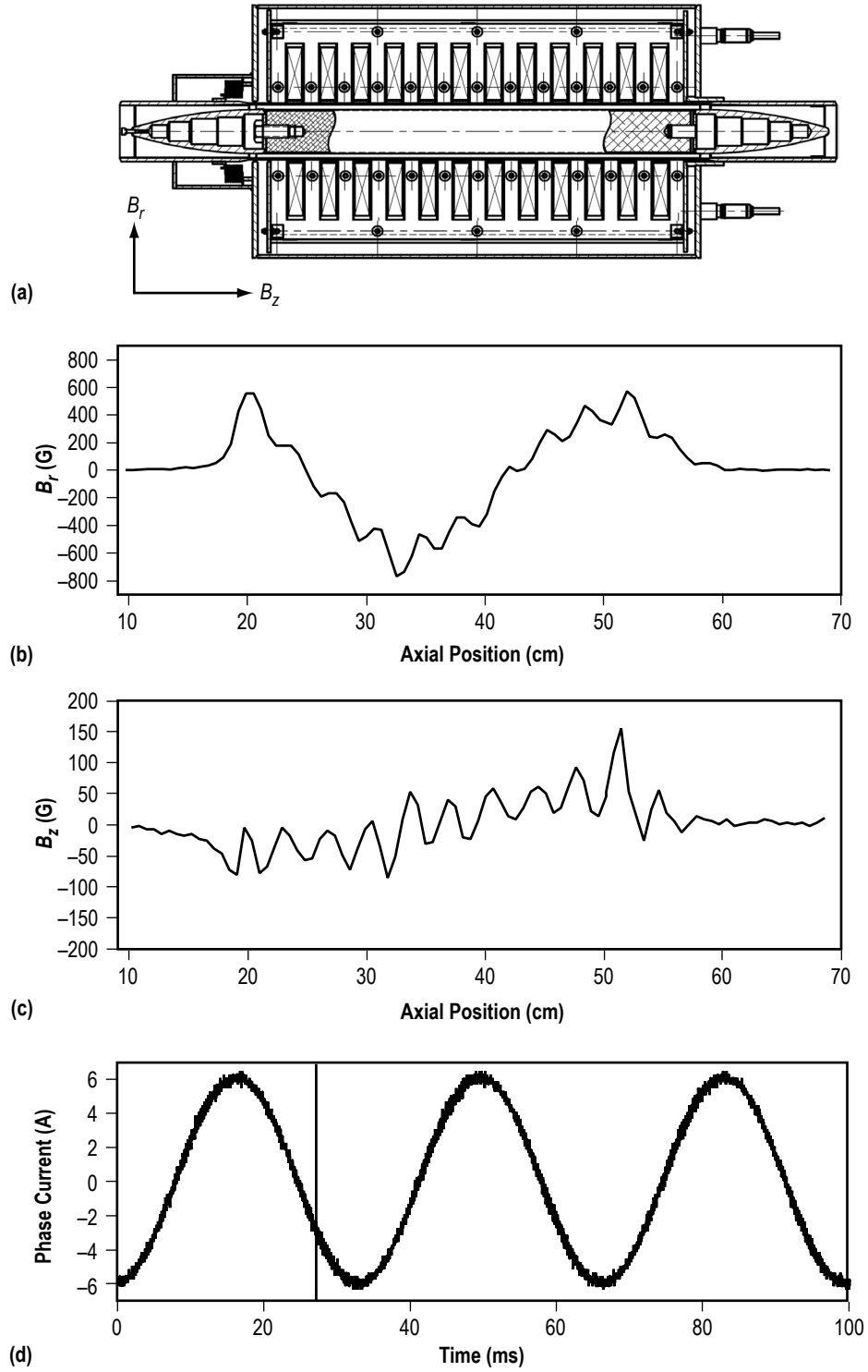
Figure 47. ALIP image (a) on the same scale as (b) and (c), (b) radial (B_r)
and (c) axial (B_z) magnetic field measurements at time $t=27$ ms,
displayed as a function of axial position in the channel. (d) Phase
current displayed with a dark vertical line showing the instant of time.
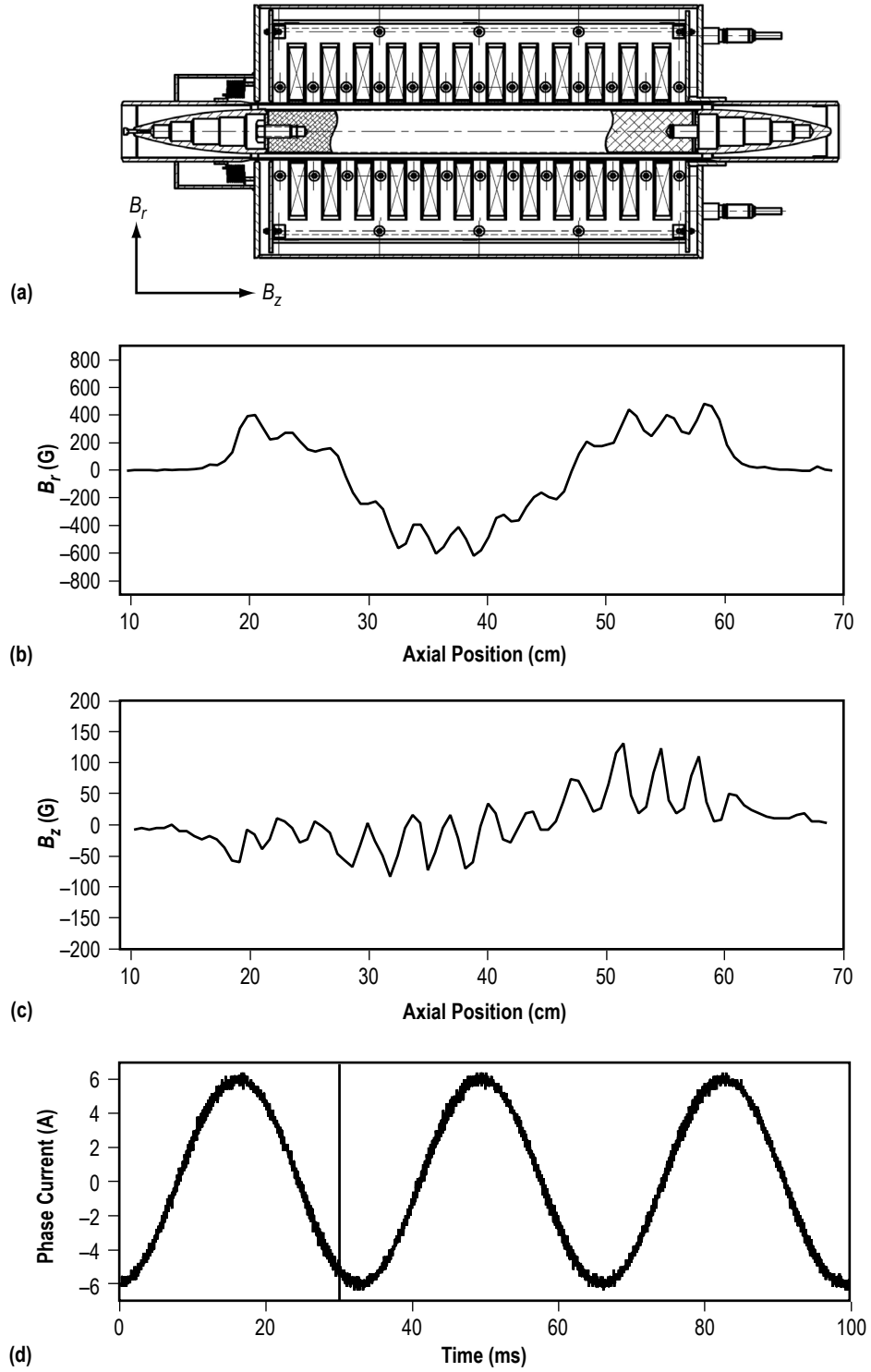
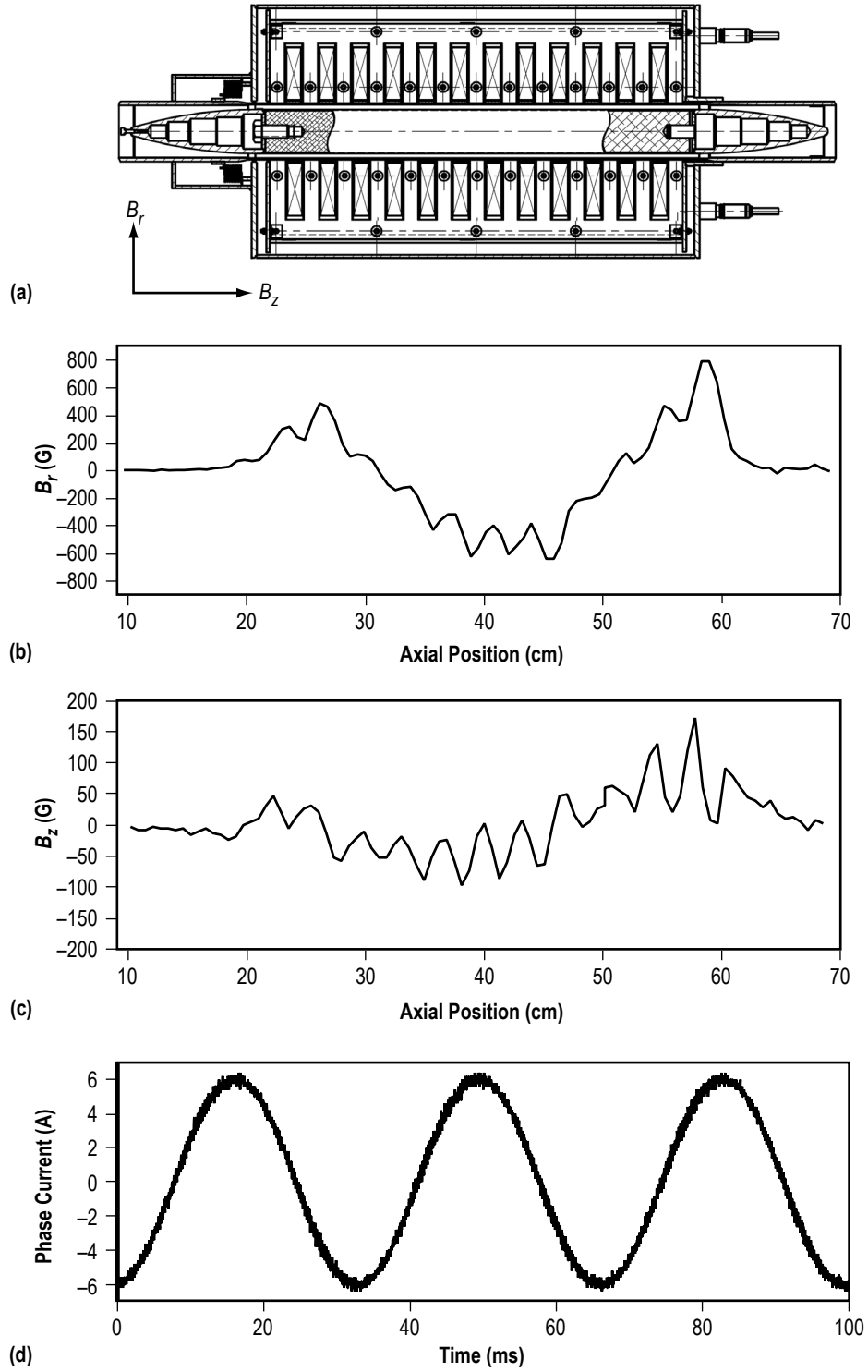Figure 48. ALIP image (a) on the same scale as (b) and (c), (b) radial (B_r)
and (c) axial (B_z) magnetic field measurements at time $t=30$ ms,
displayed as a function of axial position in the channel. (d) Phase
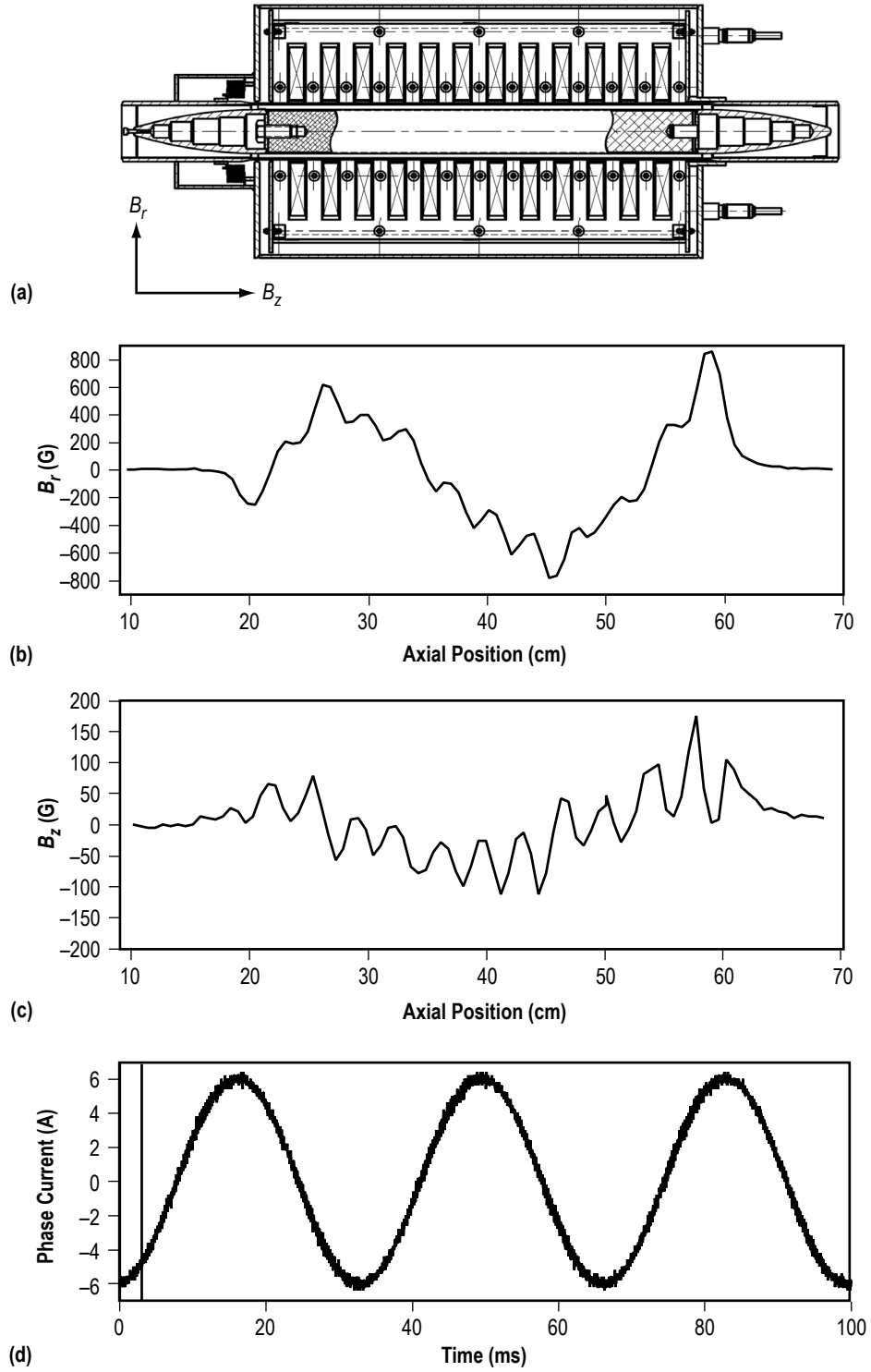current displayed with a dark vertical line showing the instant of time.

(a)

(b)

(c)

(d)
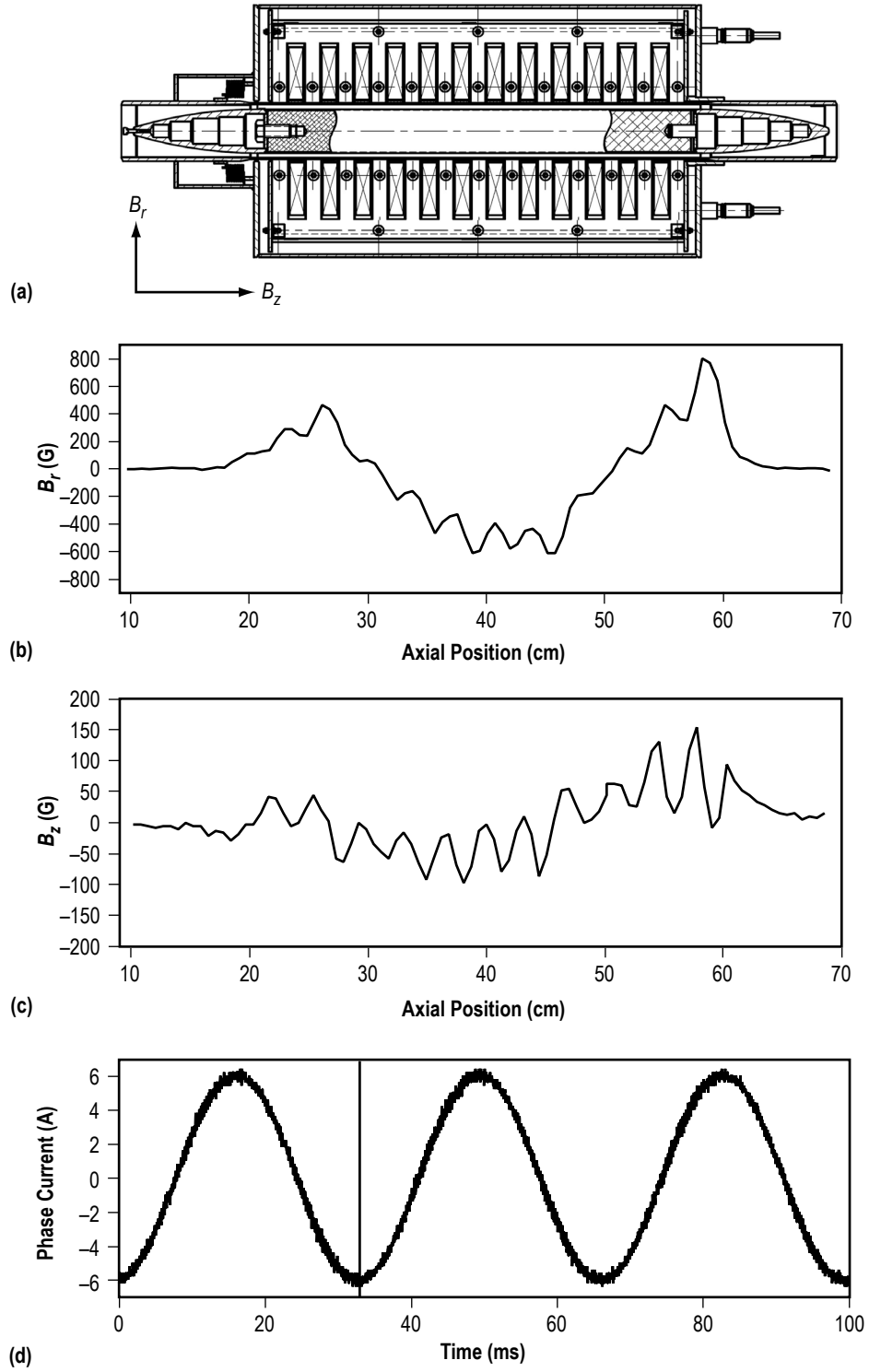
Figure 49. ALIP image (a) on the same scale as (b) and (c), (b) radial (B_r)
and (c) axial (B_z) magnetic field measurements at time $t=33$ ms,
displayed as a function of axial position in the channel. (d) Phase
current displayed with a dark vertical line showing the instant of time.

5. CONCLUSIONS

Testing was performed to quantify the performance of an ALIP. A dedicated test apparatus, the ATC, was fabricated expressly for this purpose. The results of the testing lead to the following conclusions:

- The test setup was well suited to quantifying the performance of the ALIP, allowing for accurate measurement of the various pump input parameters and resulting in narrow, well-defined uncertainties on the data set.

- The VFD output was fed through a sine wave filter and a variac transformer and provided a means to accurately control both the voltage and frequency of the three-phase power applied to the ALIP.

- The flow impedance was successfully controlled using a throttling valve, which allowed for testing across a wide range of flow parameters.

- The pump was tested up to an input of 120 V over a range of NaK temperatures from 25 to 525 °C, and at three-phase power frequencies of 33, 36, 39, and 60 Hz. The pump was fed at 60 Hz using both the VFD and ac power drawn straight from the electrical grid.

- Performance spanned the range of flow rates from roughly 0.16 to 5.7 L/s (2.5 to 90 gpm), and Δp levels from <1 to 90 kPa (<0.145 psi to roughly 13 psi). The maximum efficiency measured during testing was slightly greater than 6%.

- Efficiency decreased as the temperature in the loop increased. Efficiency was maximized near the nominal design point of 36 Hz, and was significantly lower when operating at 60 Hz.

- The data at 60 Hz exhibited no significant variation in performance between power supplied by the VFD and power drawn directly from the electrical grid.

- Performance curves were only slightly impacted when corrections were applied to the data to account for additional pressure losses that occur as the flow passes through the contraction and expansion joints upstream and downstream, respectively, of the ALIP.

- Measurements demonstrate that the flow parameters (flow rate and Δp) respond almost immediately to transients in the power applied to the pump. There is a modest coastdown period in flow rate when power to the pump is quickly brought to zero. When power is still actively supplied, there appears to be no time lag (on the 1-Hz timescale of the measurements) between variations in applied pump power and changes in the measured flow parameters.

- The temperature inside the ALIP did not exceed the NaK temperature during the startup and steady-state phases of testing indicating that the internal ALIP components were thermally well coupled to the NaK.

- Thermal wells yielded a slightly more accurate measure of the freestream NaK temperatures relative to clamped-on thermocouples.

APPENDIX A—THROTTLING VALVE STRUCTURAL ANALYSIS

NPS Gate Valve
Structural Analysis

TR-358-0018-010-R1

Prepared for: YETISPACE, Inc.

Prepared by: INTUITIVE Research and Technology Corporation
5030 Bradford Dr. Building 2, Suite 205 Huntsville, AL 35824

September 17, 2009

Engineering Disclaimer

Signature Sheet

Design prepared by:

    Jeremy Clark

_____	_____
Signature	Date

Analysis performed by:

    Jeremy Clark

_____	_____
Signature	Date

Analysis checked by:

    Rustin Webster

_____	_____
Signature	Date

Report prepared by:

    Jeremy Clark

_____	_____
Signature	Date

    Rustin Webster

_____	_____
Signature	Date

Engineering Disclaimer

Design decisions are not to be based solely on the data presented in this report. It is advised that this information be used in conjunction with experimental data and practical experience. The analysis in this report should aid in reducing the number of necessary field tests but should not be considered a replacement for them. Field testing will be needed to validate final design.

Revision Sheet

Revision Number	Change Description	Change Made By:	Date
R0	Initial release.	J. Clark	2009/09/14
R1	Added 011 Stem Cap to analysis. Modified wetted area accordingly.	J. Clark	2009/09/17

Engineering Disclaimer

Design decisions are not to be based solely on the data presented in this report. It is advised that this information be used in conjunction with experimental data and practical experience. The analysis in this report should aid in reducing the number of necessary field tests but should not be considered a replacement for them. Field testing will be needed to validate final design.

Table of Contents

Engineering Disclaimer

Design decisions are not to be based solely on the data presented in this report. It is advised that this information be used in conjunction with experimental data and practical experience. The analysis in this report should aid in reducing the number of necessary field tests but should not be considered a replacement for them. Field testing will be needed to validate final design.

List of Figures

Engineering Disclaimer

Design decisions are not to be based solely on the data presented in this report. It is advised that this information be used in conjunction with experimental data and practical experience. The analysis in this report should aid in reducing the number of necessary field tests but should not be considered a replacement for them. Field testing will be needed to validate final design.

List of Tables

Engineering Disclaimer

Design decisions are not to be based solely on the data presented in this report. It is advised that this information be used in conjunction with experimental data and practical experience. The analysis in this report should aid in reducing the number of necessary field tests but should not be considered a replacement for them. Field testing will be needed to validate final design.

60

1.0 Analysis Summary

The purpose of this analysis is to determine the maturity of the design for the NPS Gate Valve.   The loading condition for this analysis was determined based on design requirements.

The required analysis for the NPS Gate Valve consisted of a single load case requiring a load of 50 psi at a temperature of 1200°F.

Engineering Disclaimer

2.0 Model Description

The NPS Gate Valve FEA was modeled and analyzed using SolidWorks and SolidWorks Simulation, respectively. The model was comprised of 6 components:

- Stem Cap (011), Qty=1
- Valve Body (012), Qty=1
- Bottom Seal Plate (013), Qty = 1
- Squish Tube (014), Qty=2
- Bellows Cap (016), Qty=1
- Valve Plate & Stem (017), Qty=1

The following figure illustrates the various parts in the assembly.

Figure 2.0-1 NPS Gate Valve Components

Engineering Disclaimer

Design decisions are not to be based solely on the data presented in this report. It is advised that this information be used in conjunction with experimental data and practical experience. The analysis in this report should aid in reducing the number of necessary field tests but should not be considered a replacement for them. Field testing will be needed to validate final design.

2.1 Materials

The material summary for the parts depicted above is listed in the following table.

Table 2.1-1 Component Material Summary

Solids	Part Number	Material	Specification
Stem Cap	011	316 SS	ASTM A 167
Valve Body	012	316 SS	ASTM A 167
Bottom Seal Plate	013	316 SS	ASTM A 167
Squish Tube	014	316 SS	ASTM A 167
Bellows Cap	016	316L SS	ASTM A 167
Valve Plate and Stem	017	INCONEL 625	ASTM B 446

Material properties for 316 SS, 316L SS, and INCONEL 625 were determined at a temperature of 1200°F. Manufacturer data was used to determine these values. Both specifications can be seen in Appendix B.

2.2   Constraints

The NPS Gate Valve model is constrained by fixing the bottom surface of 013 Bottom Seal Plate and by vertically restraining the top surface of 017 Valve Plate and Stem. The constraint on 013 Bottom Seal Plate will prevent the valve from translating and the vertical constraint on 017 Valve Plate and Stem prevents the gate from rising. The FEA model of the NPS Gate Valve was cut two ways and symmetry constraints were chosen to ensure that the model behaved correctly. This was done so that the mesh size could be reduced and the run time for the analysis remain reasonable. The constraints are shown in the figure below.
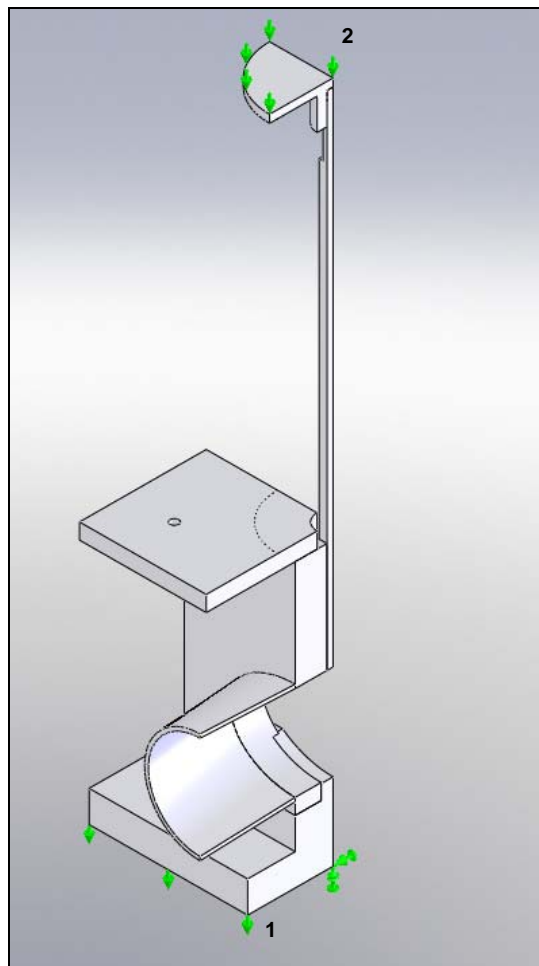
Figure 2.2-1 Constraints (1&2)

Engineering Disclaimer
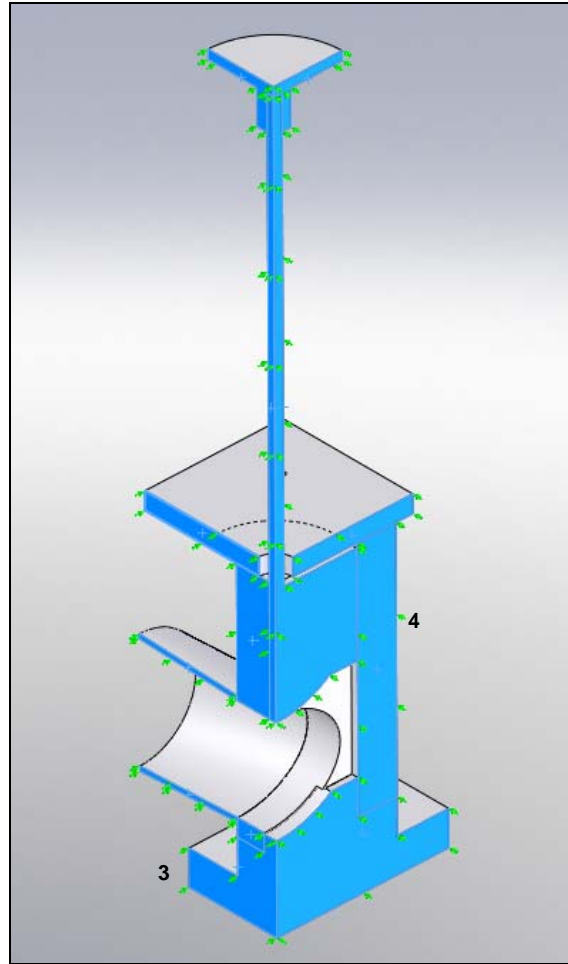
Figure 2.2-2 Constraints (3&4) – Symmetry

Engineering Disclaimer

Design decisions are not to be based solely on the data presented in this report. It is advised that this information be used in conjunction with experimental data and practical experience. The analysis in this report should aid in reducing the number of necessary field tests but should not be considered a replacement for them. Field testing will be needed to validate final design.

2.3 Mesh Details

The global mesh size used was 0.30375 inches with a tolerance of 0.0152 inches. The mesh consist of 2nd order polynomial, 10 node tetrahedral elements automatically generated by SolidWorks Simulation. Two mesh controls were used for this analysis.

Table 2.3-1 Mesh Summary

Load Case	Mesh Type	Mesh Size	Tolerance	Number of Elements	Number of Nodes
1	Solid	0.304	0.0152	47627	76959

Table 2.3-2 Mesh Controls Summary

Mesh Control	Mesh Type	Mesh Size	Applied To
1	Solid	0.120	014 Squish Tube, 011, 012, 013, & 017 Faces
2	Solid	0.060	012 & 014 Interface

The model was run with no loads and with only a temperature load to verify the constraints behaved as expected. Once these checks were completed and deemed satisfactory, a small load was applied and the reactions of the model and constraints were reviewed for behavior.

The following figures illustrate the mesh and mesh controls.
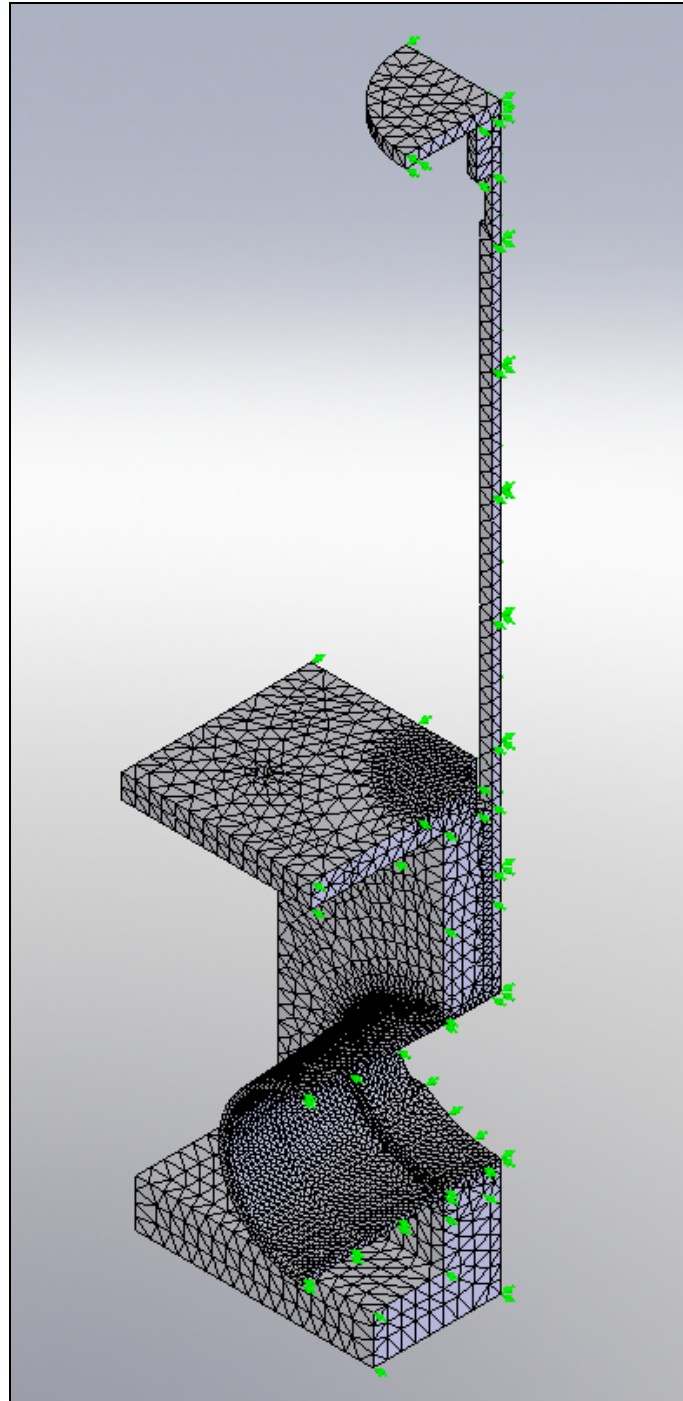
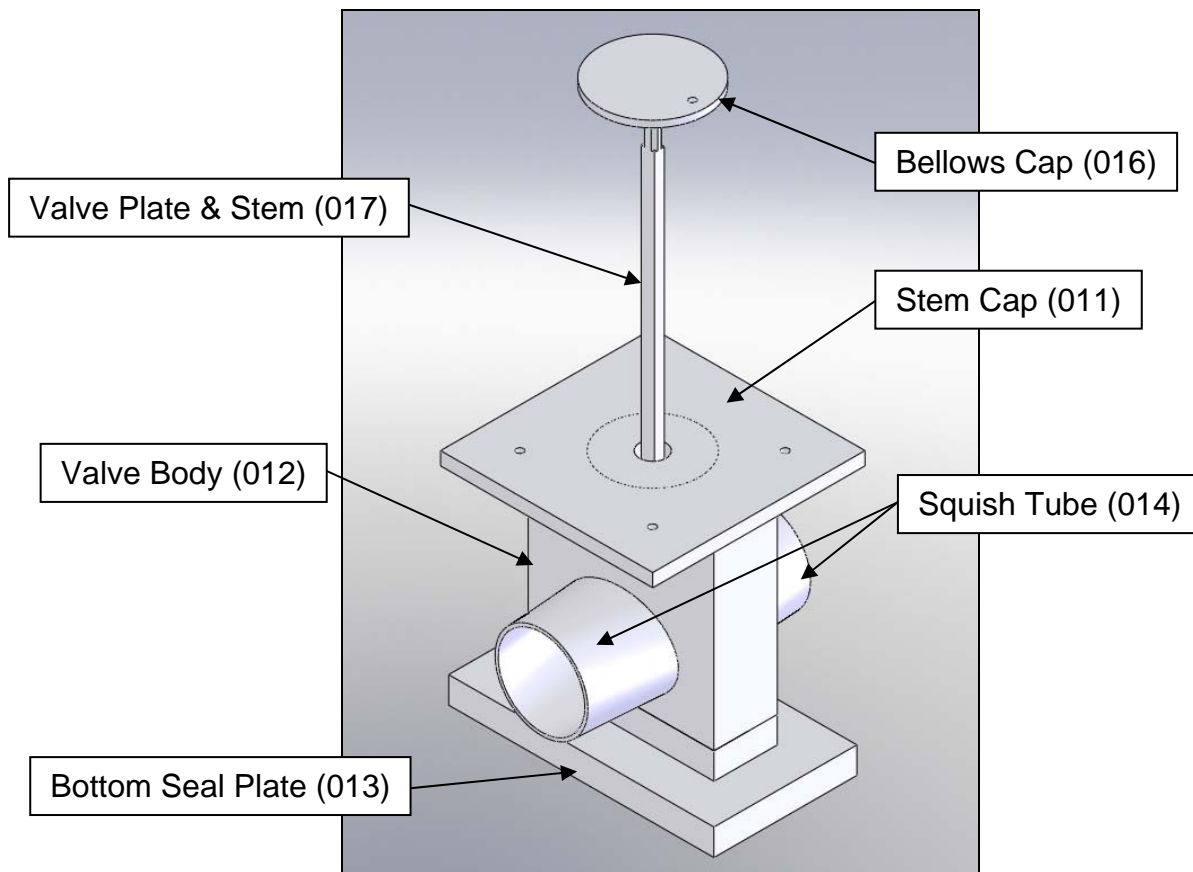**Figure 2.3-1 General Mesh 1**

Engineering Disclaimer

Design decisions are not to be based solely on the data presented in this report. It is advised that this information be used in conjunction with experimental data and practical experience. The analysis in this report should aid in reducing the number of necessary field tests but should not be considered a replacement for them. Field testing will be needed to validate final design.
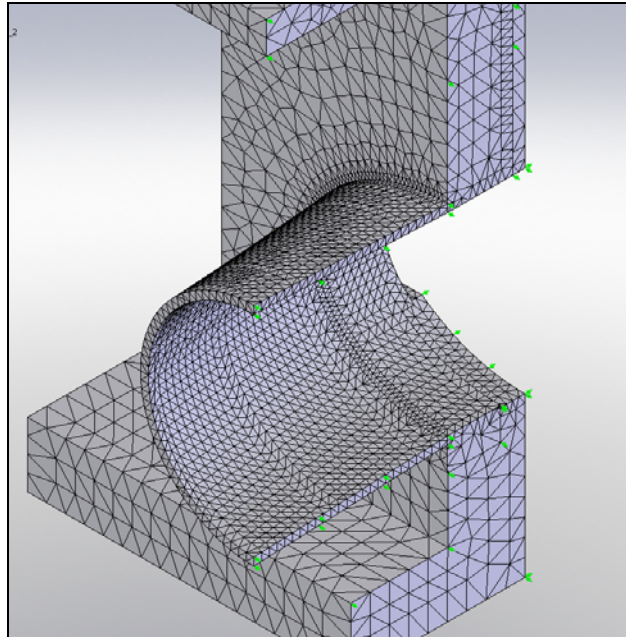
Figure 2.3-2 Detailed Mesh
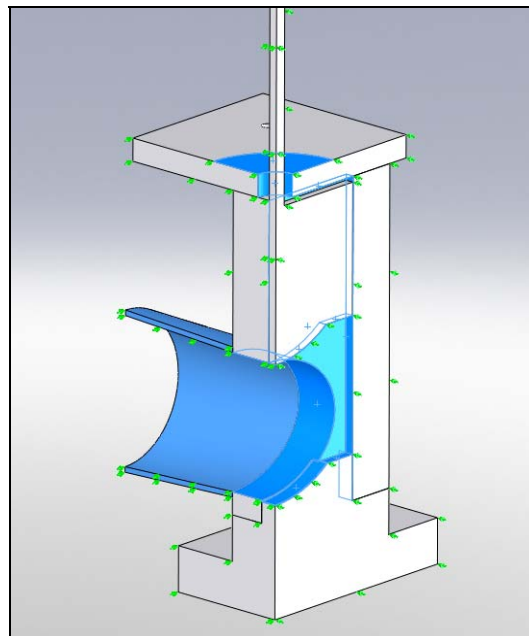
Figure 2.3-3 Mesh Control 1 (.120 in)

Engineering Disclaimer

Design decisions are not to be based solely on the data presented in this report. It is advised that this information be used in conjunction with experimental data and practical experience. The analysis in this report should aid in reducing the number of necessary field tests but should not be considered a replacement for them. Field testing will be needed to validate final design.
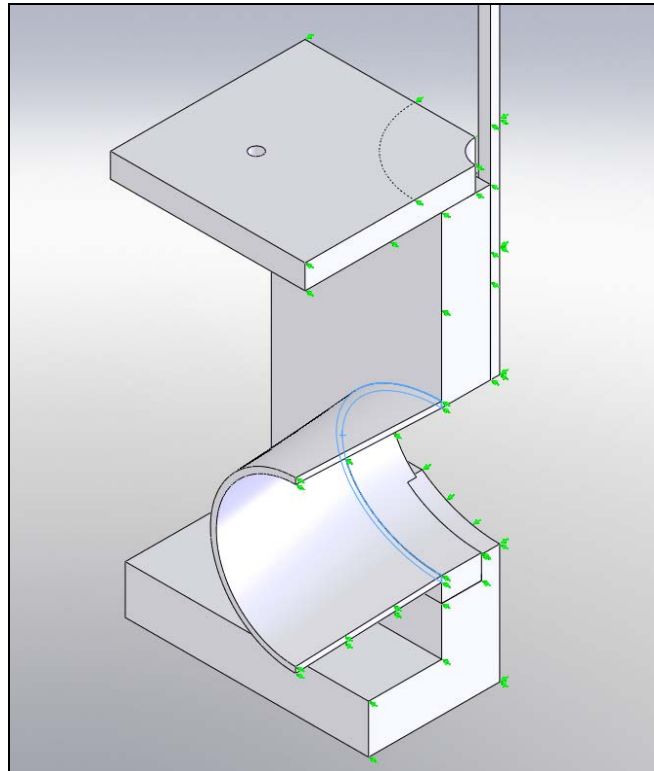
Figure 2.3-4 Mesh Control 2 (.060 in)

Engineering Disclaimer

Design decisions are not to be based solely on the data presented in this report. It is advised that this information be used in conjunction with experimental data and practical experience. The analysis in this report should aid in reducing the number of necessary field tests but should not be considered a replacement for them. Field testing will be needed to validate final design.

## 2.4   Contact and Gap Description

The contact and gap definitions for all load cases were identical.   The global contact/gap definitions were set to "no penetration".   The following table gives the contact set information.

Table 2.4-1 List of Detailed Contacts

Contact Number	Body or Bodies	Number of Faces/Edges	Type
1	012 Valve Body & 013 Bottom Seal Plate	2	Bonded
2	012 Valve Body & 014 Squish Tube	2	Bonded
3	012 Valve Body & 017 Valve Plate & Stem	2	No Penetration
4	012 Valve Body & 017 Valve Plate & Stem	2	No Penetration
5	012 Valve Body & 011 Stem Cap	3	Bonded

The following figure illustrates the locations of the contact sets.

Engineering Disclaimer
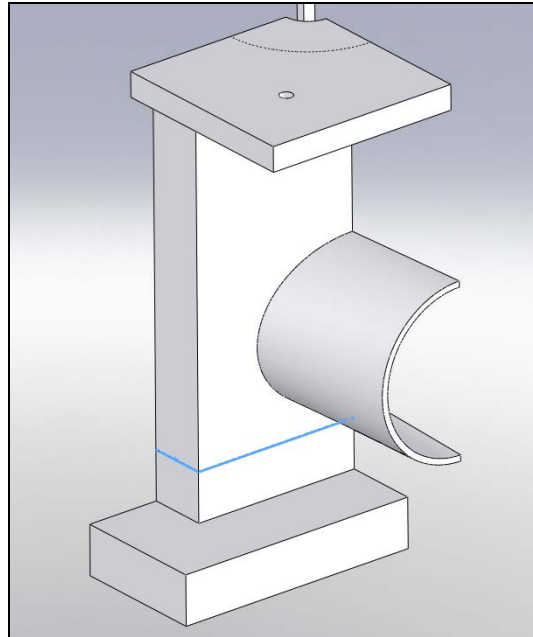
Figure 2.4-1 Contact Set 1 (Bonded)
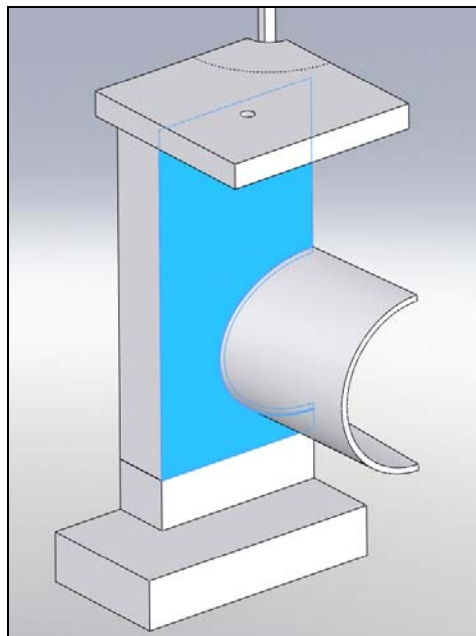
Figure 2.4-2 Contact Set 2 (Bonded)

Engineering Disclaimer

Design decisions are not to be based solely on the data presented in this report. It is advised that this information be used in conjunction with experimental data and practical experience. The analysis in this report should aid in reducing the number of necessary field tests but should not be considered a replacement for them. Field testing will be needed to validate final design.

17

Figure 2.4-3 Contact Set 3 (No Penetration)

Figure 2.4-4 Contact Set 4 (No Penetration)

Engineering Disclaimer

Design decisions are not to be based solely on the data presented in this report. It is advised that this information be used in conjunction with experimental data and practical experience. The analysis in this report should aid in reducing the number of necessary field tests but should not be considered a replacement for them. Field testing will be needed to validate final design.

72

18

2.5   Loads

The required analysis for the NPS Gate Valve consisted of a single load case requiring a load of 50 psi at a temperature of 1200°F.

2.5.1   Pressure Load

Figure 2.5.1-1 Pressure Load (50 psi)

Engineering Disclaimer

Design decisions are not to be based solely on the data presented in this report. It is advised that this information be used in conjunction with experimental data and practical experience. The analysis in this report should aid in reducing the number of necessary field tests but should not be considered a replacement for them. Field testing will be needed to validate final design.
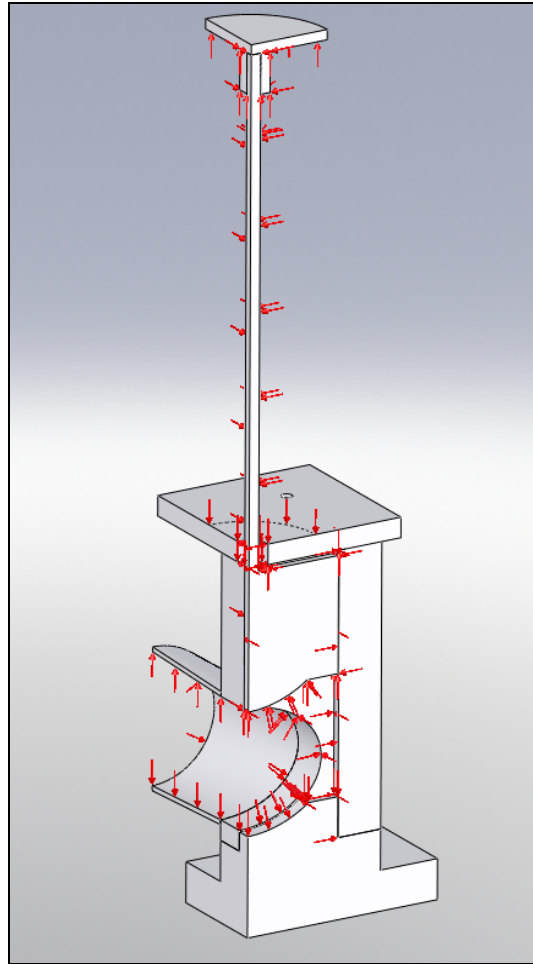
Figure 2.5.1-2 Pressure Load Cont. (50 psi)

Engineering Disclaimer

Design decisions are not to be based solely on the data presented in this report. It is advised that this information be used in conjunction with experimental data and practical experience. The analysis in this report should aid in reducing the number of necessary field tests but should not be considered a replacement for them. Field testing will be needed to validate final design.

3.0 Analysis Results

The results of the Finite Element Analysis of the NPS Gate Valve can be seen below.

Table 3.0-1 Results Summary

Maximum Stress (psi)	Minimum MOS	Maximum Displacement (in)
1820.0	7.59	0.150

It should be noted that the displacement shown above is entirely due to the change in temperature from 77°F to 1200°F. This was confirmed by running the analysis with a temperature load only and pressure load only. Then to verify, hand calculations were done to validate the results. The resulting displacement of the bottom of 017 Valve Plate & Stem with only a temperature load was .150 in. The thermal expansion of both 011 Bellows Cap and 017 Valve Plate & Stem were added together to for total displacement. Hand calculations for the displacement of the 017 Valve Plate & Stem are due to the change of temperature is shown below.

$$\delta_T = \alpha(\Delta T)L$$
$$\delta_T = 8.2 \times 10^{-6}(1200 - 77)(15.98) + 10.8 \times 10^{-6}(1200 - 77)(.25)$$
$$\delta_T = .150in$$

Table 3.0-2 Margin of Safety Summary

PART	Margin of Safety
011 Stem Cap	HIGH
012 Valve Body	14.34
013 Bottom Seal Plate	HIGH
014 Squish Tube	7.59
017 Valve Plate & Stem	HIGH

From the above tables it can be seen that the analysis results show a design where all margins of safety remain positive for all members under load by both temperature and pressure.

Detailed results for von Mises Stress, Displacement, and Margin of Safety are shown below.

Engineering Disclaimer

Design decisions are not to be based solely on the data presented in this report. It is advised that this information be used in conjunction with experimental data and practical experience. The analysis in this report should aid in reducing the number of necessary field tests but should not be considered a replacement for them. Field testing will be needed to validate final design.

3.1 Load Condition – 50 psi at 1200°F

The application of the above loading conditions produced the following results:

- Maximum Stress: 1820.0 psi
- Minimum Margin of Safety: 7.59
- Maximum Displacement: 0.150 in

The graphical results for are illustrated in the figures below.

Figure 3.1-1 von Mises Stress

Engineering Disclaimer

Design decisions are not to be based solely on the data presented in this report. It is advised that this information be used in conjunction with experimental data and practical experience. The analysis in this report should aid in reducing the number of necessary field tests but should not be considered a replacement for them. Field testing will be needed to validate final design.
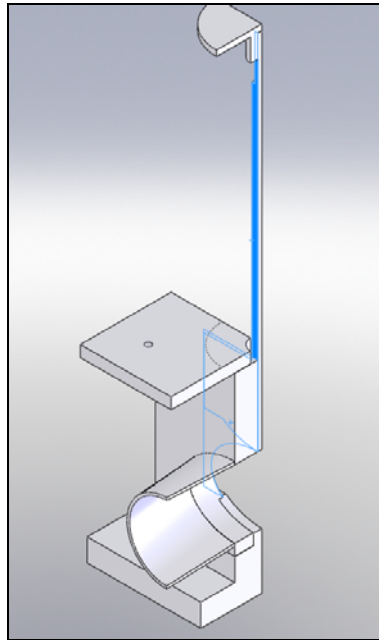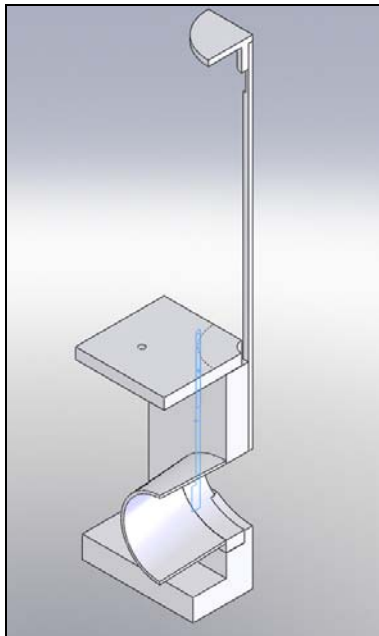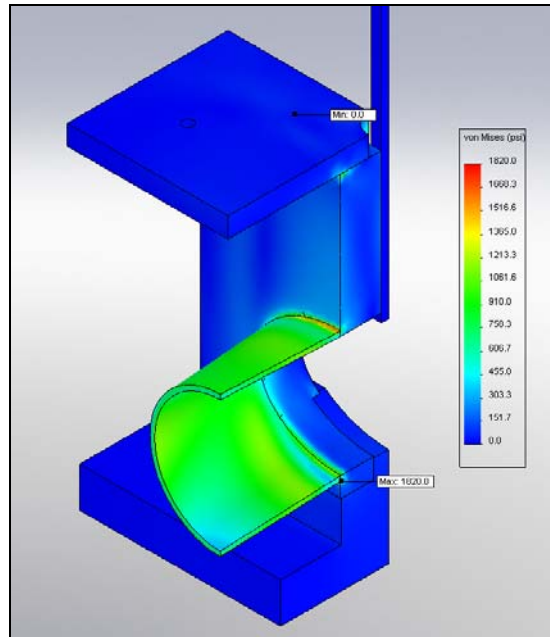
Figure 3.1-2 von Mises Stress – Zoom

Figure 3.1-3 von Mises Stress - Zoom

Engineering Disclaimer

Design decisions are not to be based solely on the data presented in this report. It is advised that this information be used in conjunction with experimental data and practical experience. The analysis in this report should aid in reducing the number of necessary field tests but should not be considered a replacement for them. Field testing will be needed to validate final design.
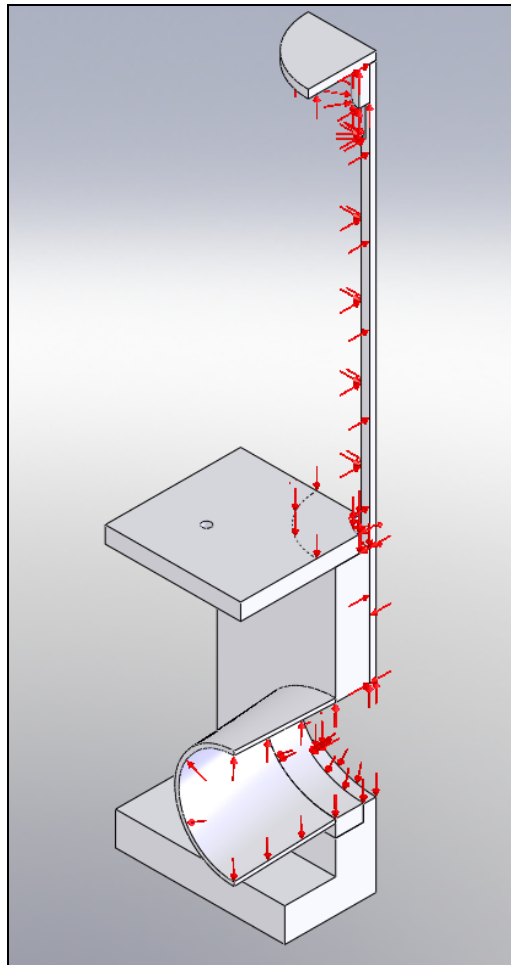
23
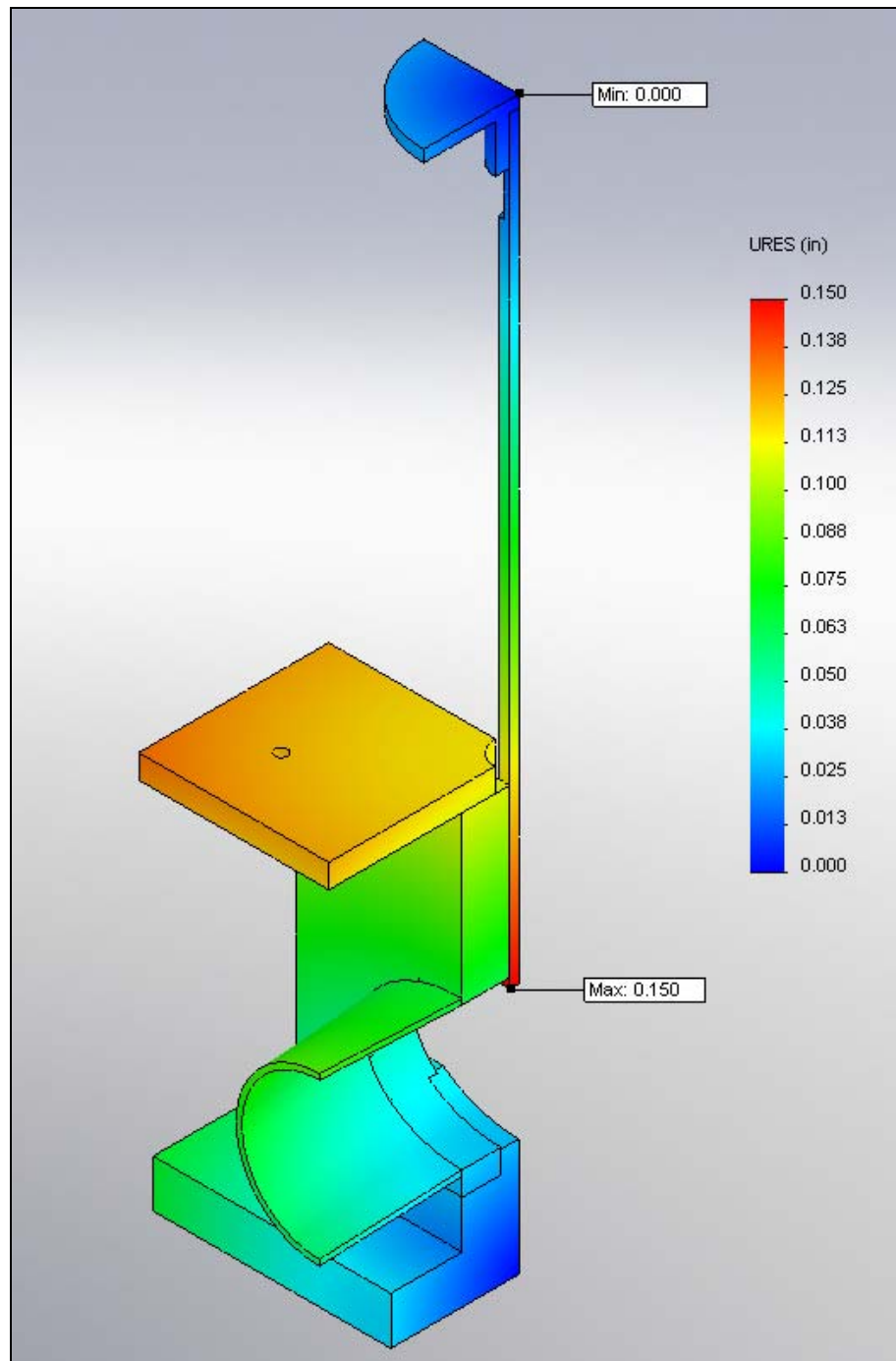
Figure 3.1-4 URES Displacement (1X)

Engineering Disclaimer

Design decisions are not to be based solely on the data presented in this report. It is advised that this information be used in conjunction with experimental data and practical experience. The analysis in this report should aid in reducing the number of necessary field tests but should not be considered a replacement for them. Field testing will be needed to validate final design.
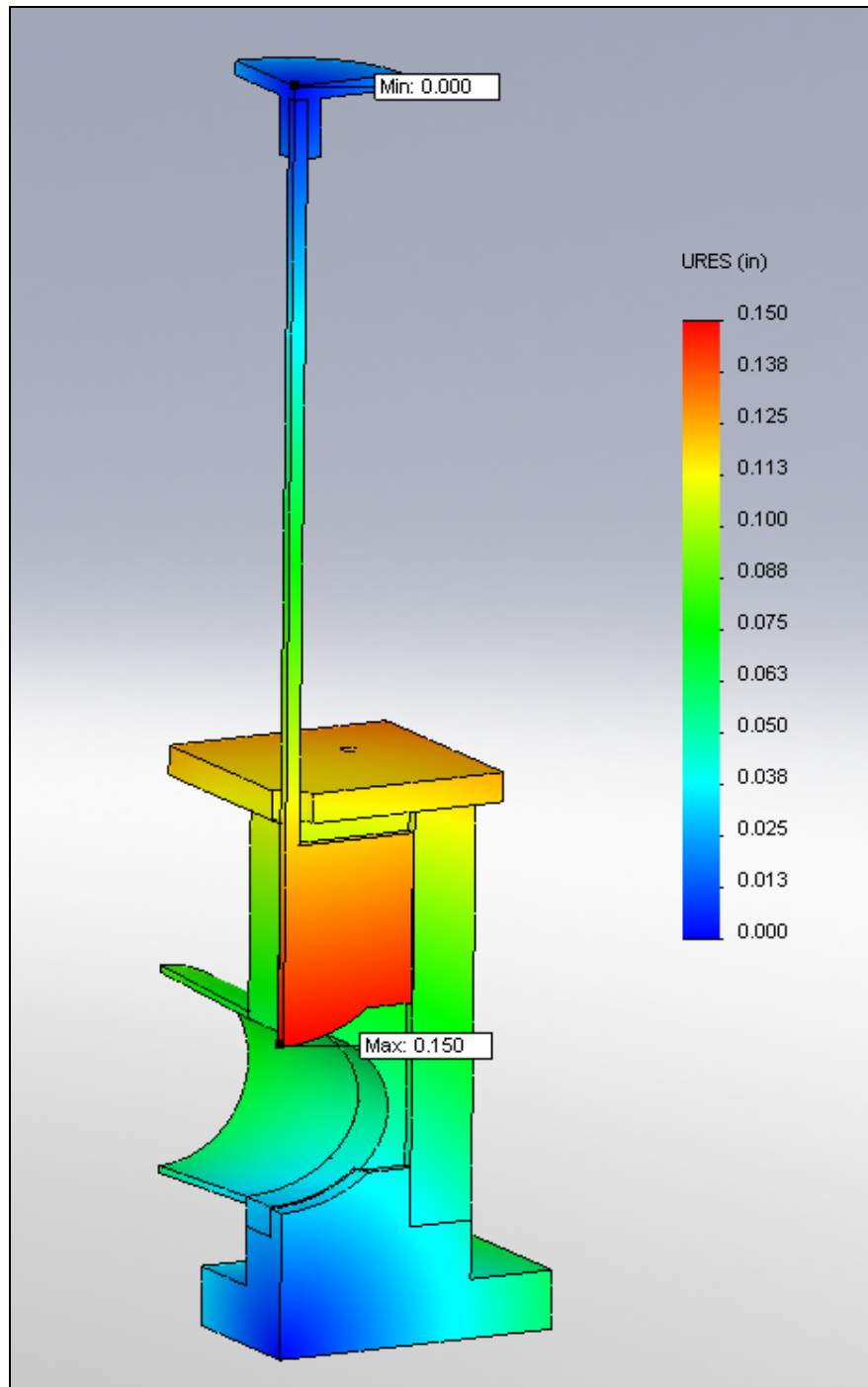
Figure 3.1-5 URES Displacement (1X)

Engineering Disclaimer

Design decisions are not to be based solely on the data presented in this report. It is advised that this information be used in conjunction with experimental data and practical experience. The analysis in this report should aid in reducing the number of necessary field tests but should not be considered a replacement for them. Field testing will be needed to validate final design.
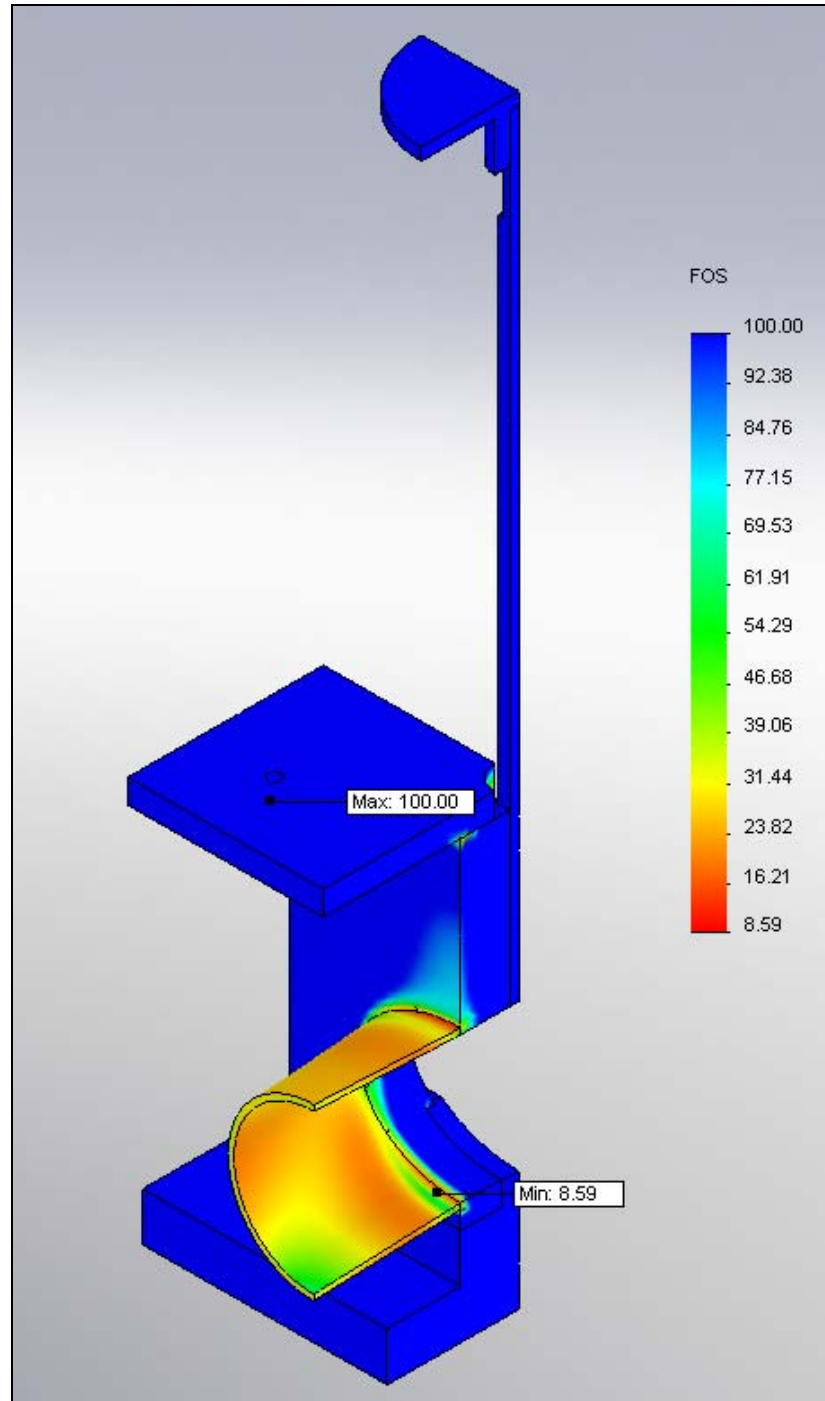
Figure 3.1-6 Factor of Safety (MOS = 7.36)

Engineering Disclaimer

Design decisions are not to be based solely on the data presented in this report. It is advised that this information be used in conjunction with experimental data and practical experience. The analysis in this report should aid in reducing the number of necessary field tests but should not be considered a replacement for them. Field testing will be needed to validate final design.

Figure 3.1-7 Factor of Safety (MOS = 7.59)
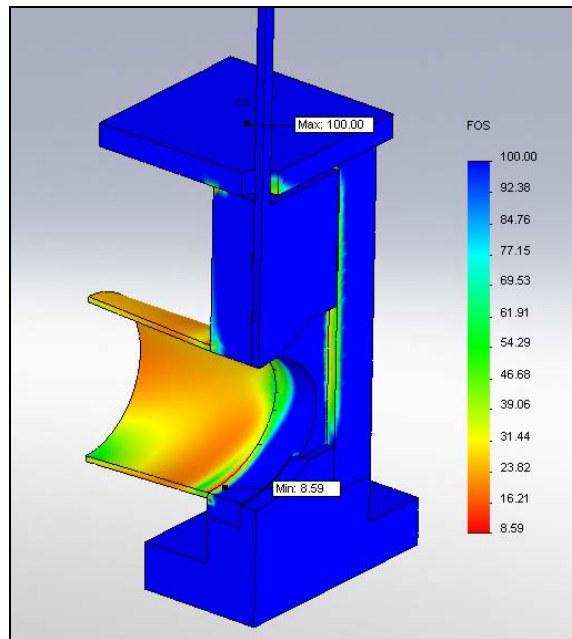
Figure 3.1-8 Factor of Safety (MOS = 7.59)

Engineering Disclaimer

Design decisions are not to be based solely on the data presented in this report. It is advised that this information be used in conjunction with experimental data and practical experience. The analysis in this report should aid in reducing the number of necessary field tests but should not be considered a replacement for them. Field testing will be needed to validate final design.
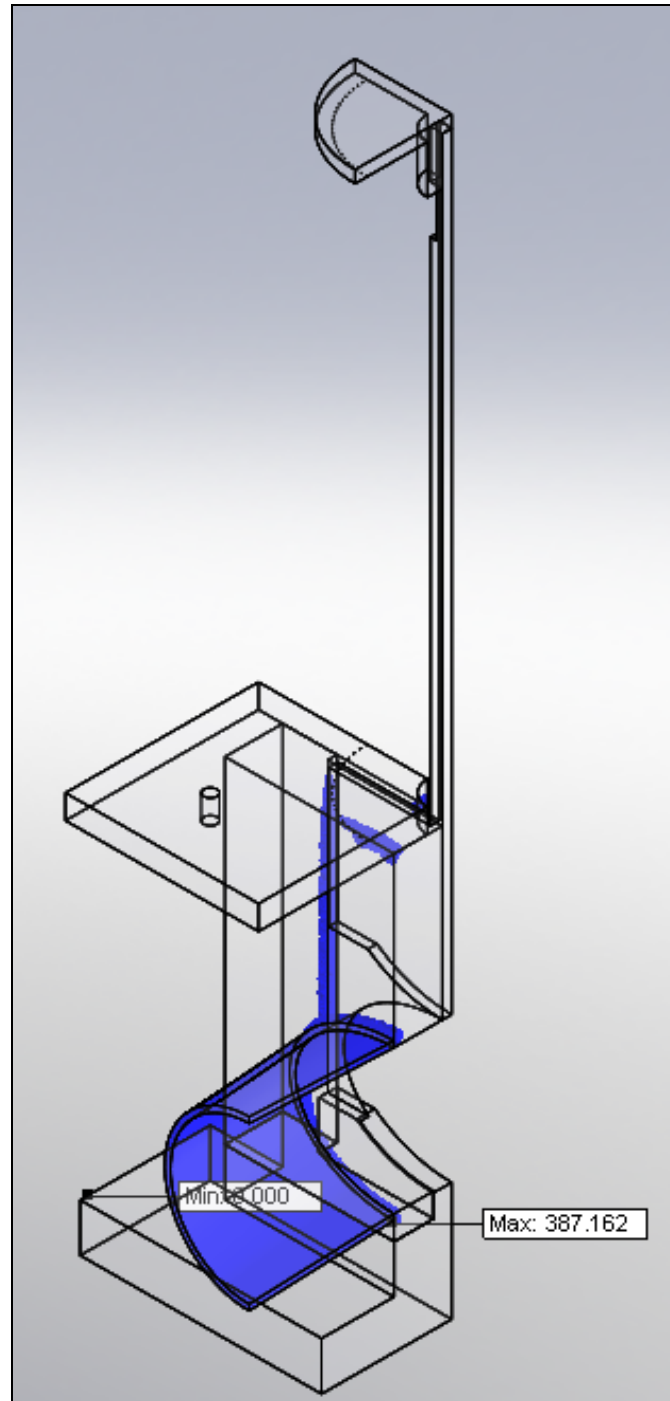
Figure 3.1-9 Design Insight Plot – Critical Load Paths

Engineering Disclaimer
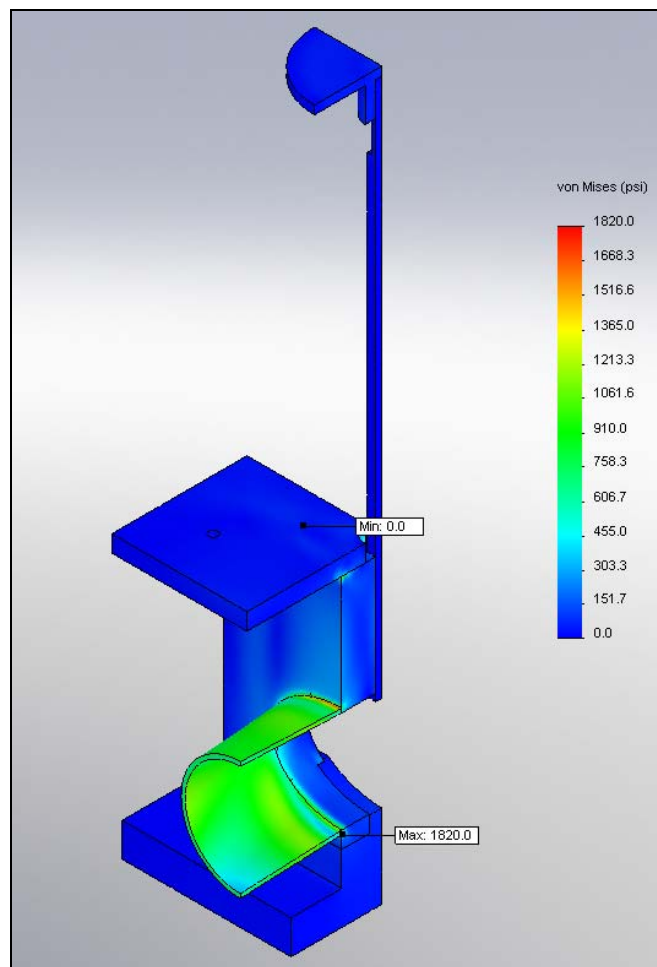
Design decisions are not to be based solely on the data presented in this report. It is advised that this information be used in conjunction with experimental data and practical experience. The analysis in this report should aid in reducing the number of necessary field tests but should not be considered a replacement for them. Field testing will be needed to validate final design.

4.0 Conclusion

The analysis of the NPS Gate Valve shows that under a temperature load of 1200°F and a pressure load of 50 psi, the design is well within required margins. First, it should be noted that 1200°F is well within the maximum working temperatures for both materials and thus is not a concern. The biggest area of concern was the two Squish Tubes for the inlet and outlet of the valve. These are shown to be at a minimum margin of 7.59, thus should not be a concern. When welded into the assembly, the inlet and outlet will be reinforced even further.

The remaining concern is the growth of 017 Valve Plate & Stem vertically. The horizontal growth (thickness) is not a concern due to the fact that the INCONEL 625 material will increase in size with temperature at a rate less than that of the surrounding material of 316 Stainless Steel. When at room temperature versus operating temperature (1200°F), the position of the gate will vary due to the way that the gate is restrained. The difference in position of the gate at room temperature was calculated by hand (.147 in) and compared to the value calculated in the FEA (.147 in). Thus, the size of the opening in the valve will reduce as the working temperature increases due to the movement of the 017 Valve Plate & Stem. This will be offset somewhat by the increase in size of the hole in the 012 Valve Body. This increase in area of the elliptical hole in the 012 Valve Body was calculated to be approximately .21 in^2 with a change of temperature from 77°F to 1200°F. Depending on the initial position of the 017 Valve Plate and Stem, the variation of the area of the valve body because of the change in temperature could be anywhere between approximately .17 in^2 and .70 in^2. This could lead to a net change in opening area of -.04 to +.49 in^2. This may or may not be a concern in the operation of the valve, but should be noted as an effect of the operating temperature.

The Stainless Steel Bellows was not included in the analysis. It was designed specifically for a 50 psi load at 1200°F temperature.
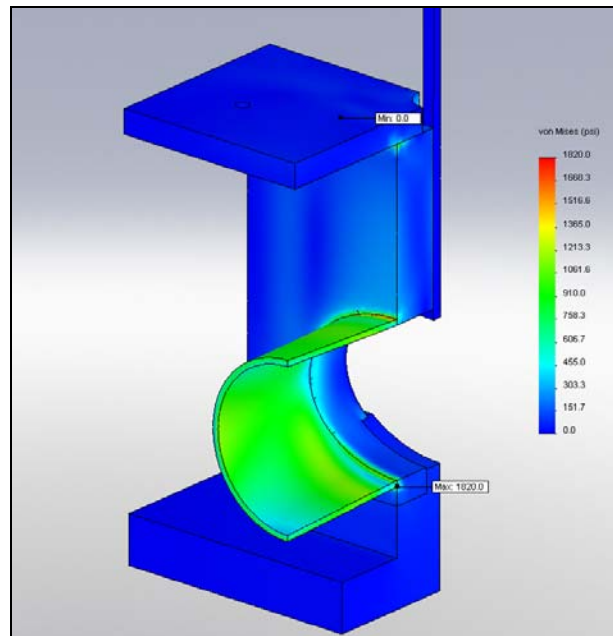
Engineering Disclaimer

APPENDIX A

Material Information

Engineering Disclaimer

Design decisions are not to be based solely on the data presented in this report. It is advised that this information be used in conjunction with experimental data and practical experience. The analysis in this report should aid in reducing the number of necessary field tests but should not be considered a replacement for them. Field testing will be needed to validate final design.

316 Stainless Steel

http://www.sandmeyersteel.com/images/316-316L-317L-Spec-Sheet.pdf

INCONEL 625

http://www.specialmetals.com/documents/Inconel%20alloy%20625.pdf

The above specification sheets are included as separate PDF files.
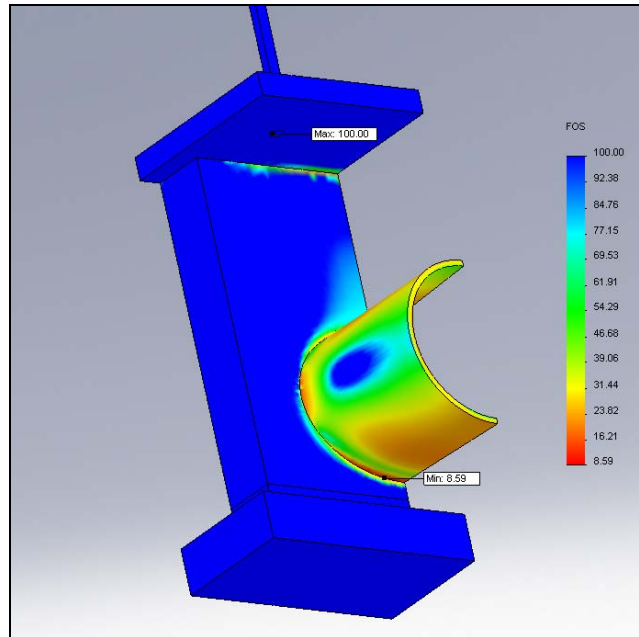
Engineering Disclaimer

Design decisions are not to be based solely on the data presented in this report. It is advised that this information be used in conjunction with experimental data and practical experience. The analysis in this report should aid in reducing the number of necessary field tests but should not be considered a replacement for them. Field testing will be needed to validate final design.

APPENDIX B—PRESSURE CORRECTIONS FROM GENERALIZED
FLUID SYSTEM SIMULATION PROGRAM MODELING

The pressure rise produced by the ALIP is given in figure 50 as Δp_{pump}, which is equal to the difference in the pressure at the pump outlet (p_{pump_out}) and inlet (p_{pump_in}). In the experimental data, the inlet and outlet hydrostatic pressures were measured at locations indicated as p_{meas_1} and p_{meas_2}, respectively. The contraction and expansion sections depicted in the figure reduce the overall value of Δp_{meas} as compared to Δp_{pump}. Consequently, the calculated efficiency based on the measurement of Δp_{meas} will be low relative to that based on Δp_{pump}.
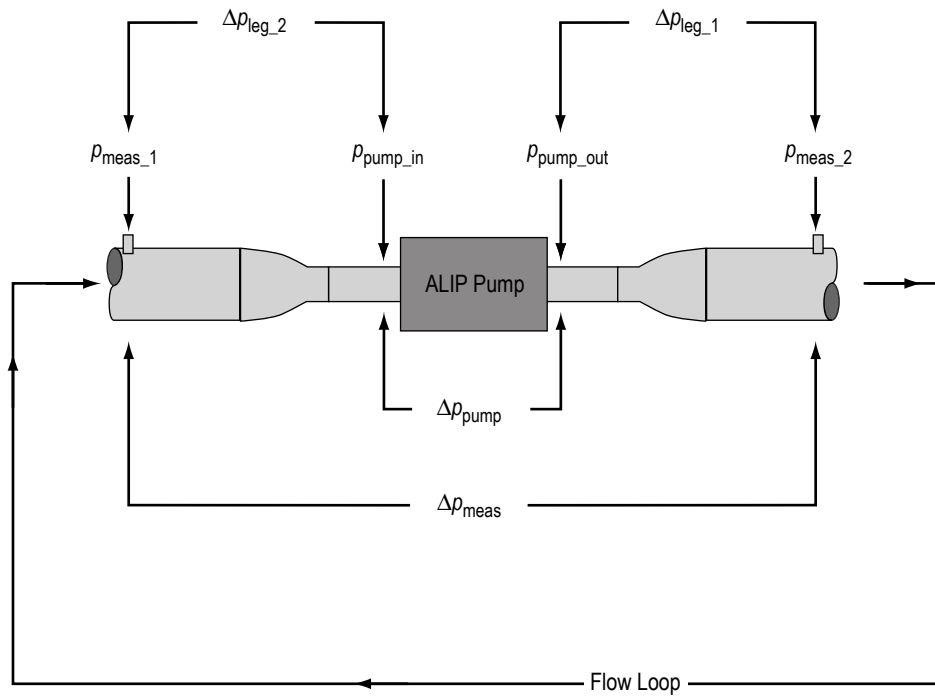
Figure 50. Illustration of the ALIP showing the pipe contraction and expansion
and the relative locations of the pressure measurements.

In this section, a correction is developed that can be added to Δp_{meas} to obtain an estimate of the true ALIP pressure rise, Δp_{pump}, to allow for a more accurate calculation of the pump's efficiency. This correction factor is a function of both flow rate and fluid temperature.

The contraction and expansion in the flow geometry between the measurement locations and the pump inlet and outlet are relatively simple features and are comprised of standard components. Consequently, it was assumed that a computational approach could be used to generate a satisfactory correction factor. The Generalized Fluid System Simulation program (GFSSP) developed at

MSFC was used for this purpose.[12] This program is an advanced computational fluid network solver and has been validated on many different fluid flow applications.

GFSSP models a system as a flow network consisting of a series of nodes and branches. The fluid properties of NaK, specifically thermal conductivity, density, viscosity, ratio of specific heats (gamma), enthalpy, entropy, and the specific heat (C_p), all as a function of temperature, were taken from the published literature.[13]

B.1 Modeling Details

The differences between measured (Δp_{meas}) and actual (Δp_{pump}) pump pressure arise from losses at the expansion from the smaller diameter ALIP pipe to the larger diameter pipe comprising the ATC (Δp_{leg_1}) and the contraction from the larger diameter to the smaller ALIP pipe (Δp_{leg_2}) (fig. 50). The expansion/contraction sections are modeled in GFSSP using a finite number of step contractions.

The pipe comprising the outlet of the ALIP (leg 1) consists of a 7.62-cm- (3-in-) long section of pipe having an inner diameter (ID) of 5.48 cm (2.157 in). The weld joint between the ALIP pipe and the expansion section is modeled as a thick orifice, with the weld extending 0.16 cm (0.0625 in) into the flow and having a streamwise length of 0.16 cm (0.0625 in). Beyond the weld there is a 2.54-cm- (1-in-) long section of pipe with an ID of 5.48 cm (2.157 in). The transition from this size to the larger 8.28-cm (3.26-in) ID pipe is accomplished using a series of five square-edged expansions. The area ratio (smaller-to-larger cross-sectional area) of each step was kept between 0.92 and 0.95 to ensure that the change in any single element was gradual. A review of reference data indicates that area ratios in this range have small loss coefficients.[14] This leads to the conclusion that the modeling technique employed provides a suitable representation of the smooth (low-loss) expansion/contraction components used in the ATC.

Beyond the transition, there is another straight section of pipe having a length of 2.54 cm (1 in) and an ID of 8.28 cm (3.26 in). A weld joint, modeled in the same manner as the previous weld, joins the larger diameter part of the expansion joint to the piping comprising the rest of the ATC. Following the weld, the fluid flows for 7.62 cm (3 in) in an 8.28-cm (3.26-in) ID pipe before it reaches the location for the downstream pressure measurement (p_{meas_2}). This model of the expansion is then reversed to model the contraction at the ALIP inlet (leg 2). The GFSSP model schematics of these two sections are shown in figure 51.

Each leg can be solved independently to determine the pressure difference from one end to the other as a function of flow rate and temperature. This is accomplished in GFSSP by first specifying the pressure loss between the two ends of the leg and then self-consistently calculating the corresponding flow rate. This calculation is repeated over the range of pressures to create the characteristic curve of pressure loss as a function of flow rate. The effects of fluid temperature on the pressure loss in each leg was ascertained by creating similar characteristic curves at various temperatures between 25 and 525 °C.

(a) Leg 1

(b) Leg 2
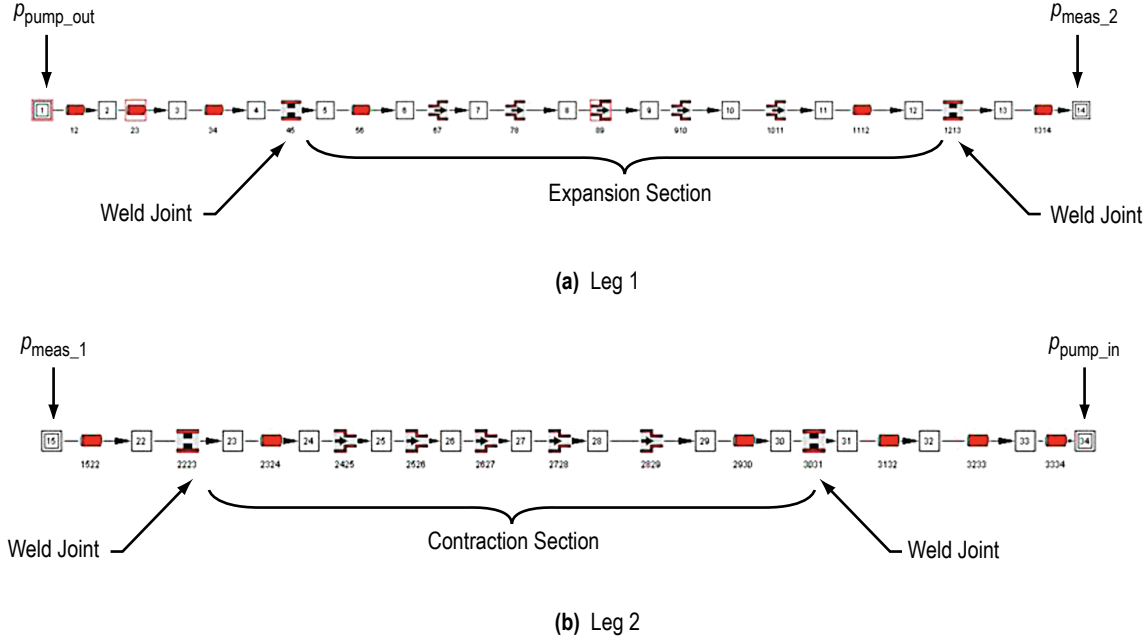
Figure 51. GFSSP graphical representation of the (a) expansion section (leg 1)
and (b) contraction section (leg 2).

B.2 Modeling Results

The computed pressure drops in legs 1 and 2 are plotted as a function of flow rate in figure 52, with each curve corresponding to a different NaK temperature. The resulting pressure losses for each temperature are fit to a second-order polynomial function with a *y*-intercept fixed at zero, since basic fluid flow relationships state that pressure loss is proportional to the mean low velocity (hence, volumetric flow rate) squared.

The correction for computing Δp_{pump} based on Δp_{meas} can be written as

$$\Delta p_{\text{pump}} = \Delta p_{\text{meas}} + \Delta p_{\text{correction}} = \Delta p_{\text{meas}} + \Delta p_{\text{leg\_1}} + \Delta p_{\text{leg\_2}} \; , \tag{3}$$

where $\Delta p_{\text{correction}}$, $\Delta p_{\text{leg\_1}}$, and $\Delta p_{\text{leg\_2}}$ are a function of flow rate and NaK temperature. The total correction for each temperature is obtained by combining the losses in the two legs (fig. 53).

$\Delta p_{\text{leg\_1}}$ and $\Delta p_{\text{leg\_2}}$ are quadratic functions of flow rate, and it follows that the resulting overall correction varies in the same manner. When examining the resulting curve fit for $\Delta p_{\text{correction}}$, it might be reasonable to expect that the fit would still retain physical verisimilitude when the first-order coefficient of the fit was neglected. This expectation was borne out in the results, with the resulting pressure drop correction for each temperature being well represented by a single, second-order coefficient.

(a)

(b)
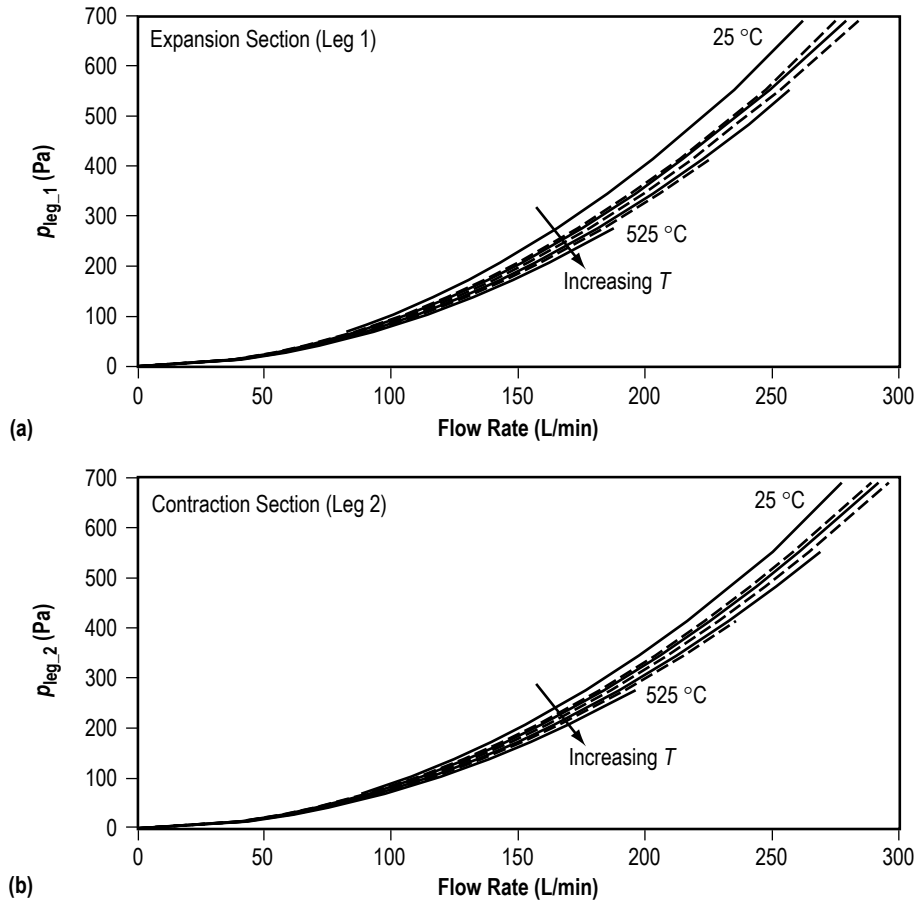
Figure 52. Computed pressure loss as a function of flow rate for (a) leg 1 and (b) leg 2 for seven different temperatures (25, 75, 125, 225, 325, 425 and 525 **°**C).
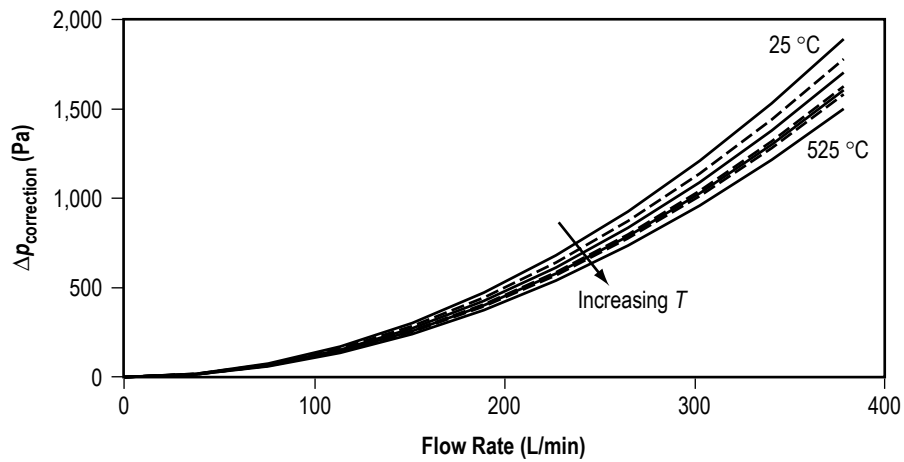
Figure 53. Total pressure correction as a function of flow rate for seven different temperatures (25, 75, 125, 225, 325, 425 and 525 **°**C).

Using only a single coefficient on the curve fit for each temperature significantly reduced the complexity of enfolding temperature dependence into an overall, functional relationship between the flow rate and pressure loss. This was accomplished by plotting the second-order coefficient for each temperature as a function of temperature and then performing a polynomial curve fit on the set. A third-order (in temperature) polynomial fit provided the best approximation of the functional relationship for the second-order (in flow rate) pressure correction coefficients. This results in:

$$\Delta p_{correction} = \left(a_0 T^3 + b_0 T^2 + c_0 T + d_0\right)\dot{v}^2 , \tag{4}$$

where

$a_0 = -6.6013 \times 10^{-11}$ Pa/(C^3-L^2/min^2)
$b_0 = \ \ 6.3584 \times 10^{-8}$ Pa/(C^2-L^2/min^2)
$c_0 = -2.1314 \times 10^{-5}$ Pa/(C-L^2/min^2)
$d_0 = \ \ 1.3682 \times 10^{-2}$ Pa/(L^2/min^2).

Equation (4) predicts the pressure correction for any given value of temperature and flow rate from zero to 80 gpm and 25 to 525 °C.

B.3 Sensitivity Analysis

An analysis was performed to obtain an estimate of the sensitivity of the computed results to variations in input values. While the expansion and contraction sections have been modeled as a series of discrete elements, pipe sections, thick orifices, and step expansion and contraction sections, the ensemble can also be modeled in GFSSP using a single restriction element. This element requires an effective cross-sectional area for the transition and a flow coefficient, C_L. Previously computed results at each of the seven fluid temperatures were used to determine the C_L values that would yield the same flow rate for a given pressure drop across each leg. By varying C_L, the sensitivity of the pressure drop correction factor to variations in the flow coefficient can be ascertained.

The nominal C_L (value matching single restriction to the modeling performed using discrete steps to represent the expansion and contraction) was varied, and the resulting pressure losses were computed for the same flow rates. The maximum variation in C_L was assumed to be $\pm10\%$.[14] Computing the resulting pressure losses for these maximum variations in C_L bounds the resulting pressure loss and yields its sensitivity to flow coefficient variations. This analysis was performed for two fluid temperatures, 25 and 525 °C. Two flow rates were examined at each temperature. The results from this analysis are shown in figure 54, where the curve represents the nominal case and the 'error bars' show the sensitivity to flow coefficient. The results are summarized in table 1.

Increasing the flow coefficient by 10% decreased the pressure loss in the transitions by roughly 10% while decreasing the flow coefficient by 10% had a larger effect as it increased the pressure loss by 12% to 15%. In other words, the model is more sensitive to an underestimate of system losses than an overestimate.
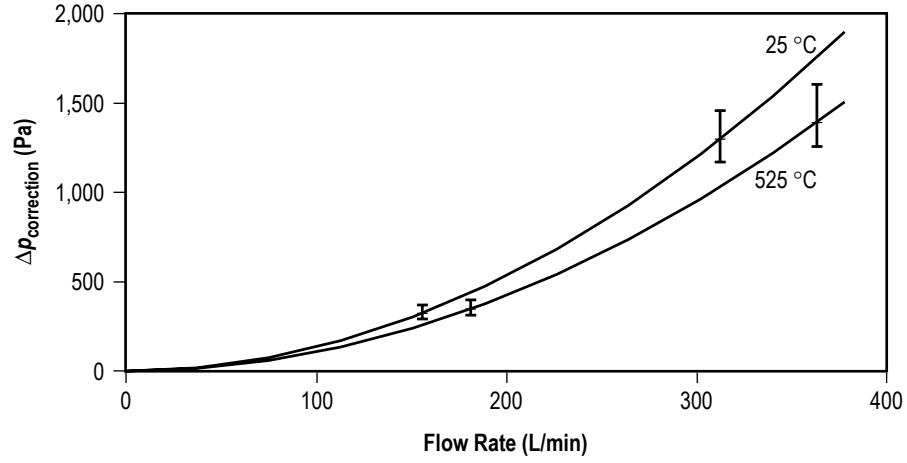
Figure 54. Range of variation in Δp as a function of flow rate, with the error
bars showing the sensitivity to a $\pm 10\%$ variation in the value of C_L.

Table 1. Summary of the range of variation in $\Delta p_{correction}$
for a $\pm 10\%$ variation in the value of C_L.

Fluid Temperature (°C)	CL Variation (%)	% Change in $\Delta p_{correction}$	
		at 11.02 kg/s	at 22.05 kg/s
25	+10	−9.61	−9.93
	−10	14.58	12.33
525	+10	−9.71	−9.59
	−10	14.82	15.35

APPENDIX C—ELECTROMAGNETIC FLOWMETER CALIBRATION

Two identical EM flowmeters were fabricated during the course of testing—one was integrated into the ATC while the other was sent to Creative Engineers, Inc. (CEI), York, PA, for calibration testing. The flowmeter at CEI was placed in a small vacuum vessel to reduce convective heat transfer between the flow channel and the permanent magnets. The entire unit was integrated into the test setup shown schematically in figure 55.
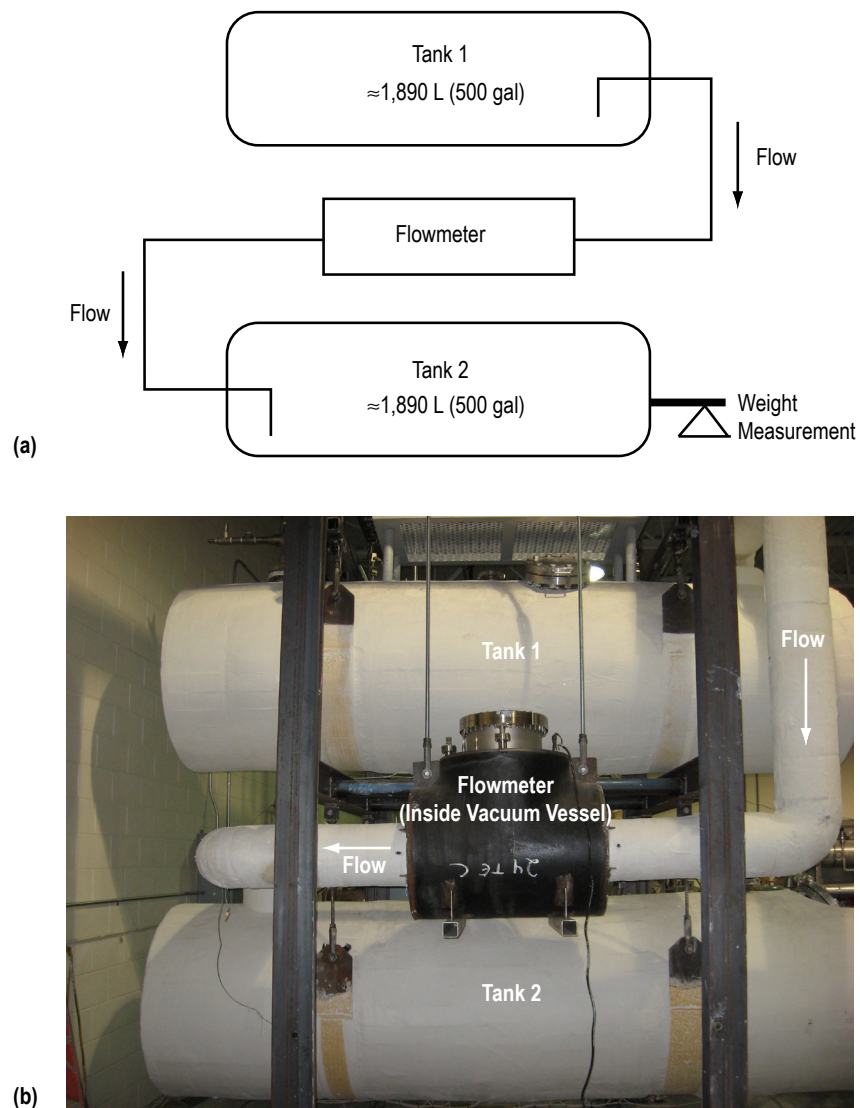
Figure 55. Test setup: (a) Schematic of the flowmeter calibration
setup and (b) photograph of the test setup at CEI.

The relationship between volumetric flow rate and induced voltage is linear (as shown in eq. (1), sec. 2.2.3), as long as the fluid is relatively conductive. Consequently, the flowmeter can be calibrated on any conductive fluid as long as the volumetric flow rate can be independently quantified. In the present work, liquid sodium (Na) was used for the calibration. Testing was performed by first heating the Na in tank 1 to melt it and raise its temperature to a level that was comparable to what would be seen by the flowmeter in the ATC (calibration data obtained at roughly 150 and 500 °C). A valve was opened, allowing the liquid Na to flow from tank 1 into tank 2. As the Na flowed, the induced voltage at the flowmeter and the mass of tank 2 (in kg) were recorded at a frequency of 1 Hz. The error on the induced voltage measurement was essentially a DAQ system limit of ±0.02 mV, while the error on the mass measurement was ±1% or ±0.45 kg (1 lb), whichever was greater. Thermocouple measurements on tank 1 (also recorded at 1 Hz) were also stored and used to compute the density of the Na flowing in the system.

C.1 Data Reduction Method

A sample calibration data set as a function of time is shown in figure 56. The volume (v) of Na in tank 2 is given in panel (a), while the signal from the flowmeter is found in panel (b). The Na volume has been computed from the accumulated mass measurement using the following relation for the density,[15]

$$\rho_{Na} = 0.9493 - 0.1245 \times 10^{-3}\, T \ , \tag{5}$$

where ρ_{Na} is in units of g/cm^3 and T is in units of °F. For the 150 °C data set, the Na temperature varied from 133–160 °C, while the variation on the 500 °C data set was 470–548 °C. The density
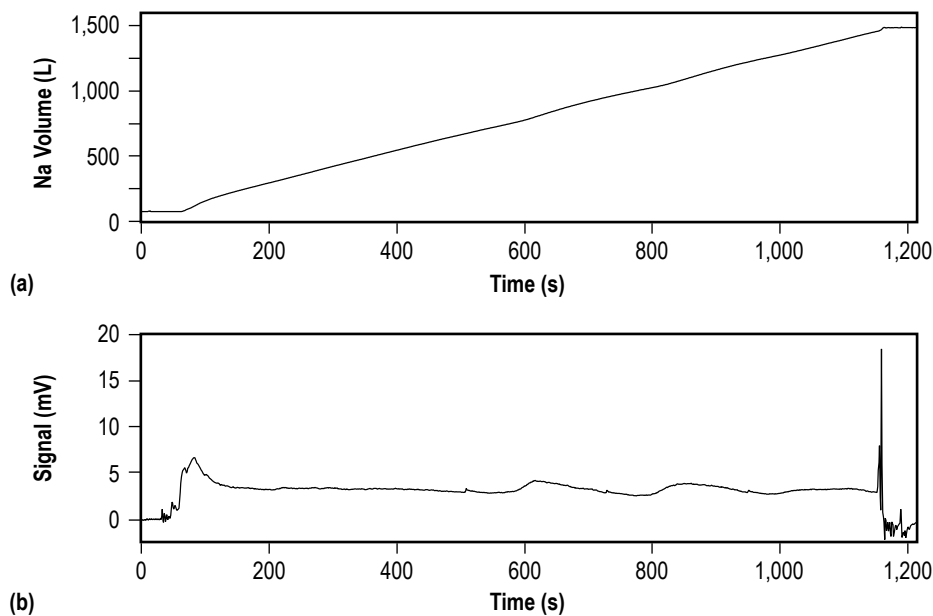
Figure 56. Sample flowmeter calibration data set showing (a) accumulated Na volume and (b) flowmeter output voltage as a function of time.

used to calculate volume was based on the mean temperature for the data set. The uncertainty is taken as the difference between the density at the mean temperature and the value calculated at the maximum or minimum temperature in the set. (Note: Because the temperature range is the full width of the variation, the uncertainty on the density calculated by this method is a 100% confidence interval, and is multiplied by 0.66 to yield a 1-σ confidence interval.) The volume of Na accumulated is the mass accumulated (m) divided by the density, and the error on this value is

$$\sigma_v^2 = \left(\frac{1}{\rho_{\text{Na}}}\right)^2 \sigma_m^2 + \left(\frac{m}{\left(\rho_{\text{Na}}\right)^2}\right)^2 \sigma_\rho^2 \ , \tag{6}$$

where the σ values represent the systematic (as opposed to random) uncertainty on each data point, with the subscripts denoting which quantity (volume, mass, density) is associated with the uncertainty.

In figure 57, a subset of the data founding figure 56 is plotted as a function of time (t). In this region, the flowmeter signal can be accurately approximated as a linear function of time, which will prove critical to the analysis that follows. The accumulated volume is curve fit to a quadratic function of t:

$$v_{\text{fit}} = a + bt + ct^2 \ , \tag{7}$$

where a, b, and c are curve fit coefficients.

The derivative is

$$\dot{v} = b + 2ct \ , \tag{8}$$

where $\dot{v}$ is the volumetric flow rate, which is constructed to be a linear function of time. Performing the curve fit and then taking the derivative introduces less error than numerically calculating the derivative at each point using a finite-difference method.

The error band in equation (7) (given by the dashed lines in fig. 57) is found by performing a curve fit of the values of σ_v calculated from equation (6) for each data point, and is given as

$$\sigma_{v,\text{fit}} = d + et + ft^2 \ , \tag{9}$$

where d, e, and f are curve fit coefficients. Since the errors are systematic, the actual data are expected to follow a curve that is a quadratic function of t and lies somewhere within the error band. The error on the volumetric flow rate is the derivative of equation (9), given as

$$\sigma_{\dot{v}} = e + 2ft \ . \tag{10}$$
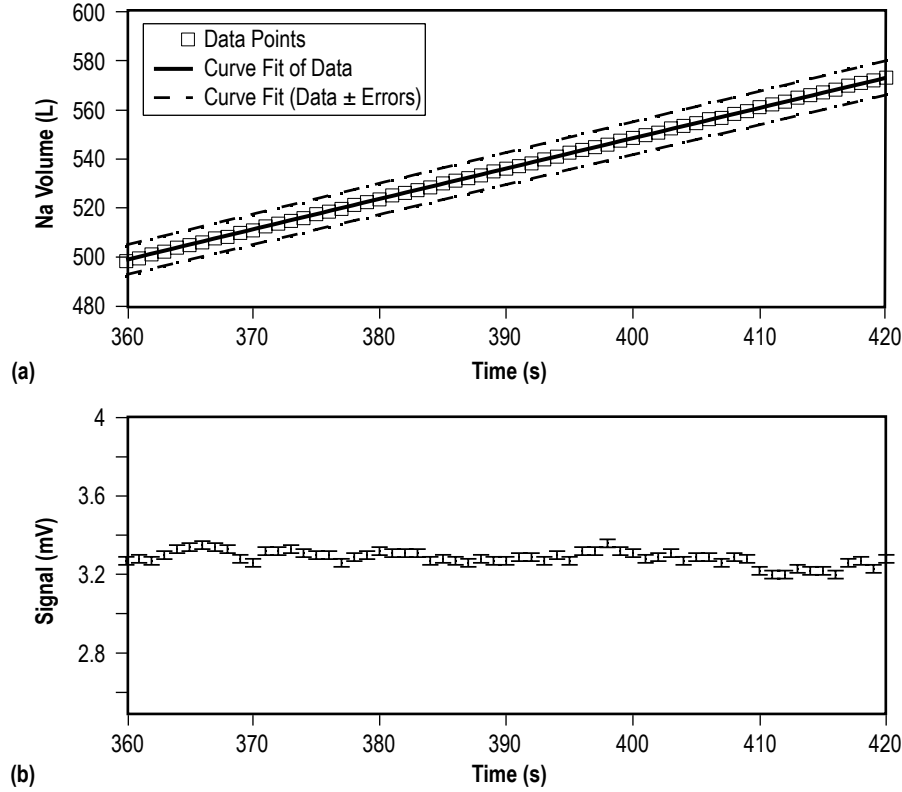
Figure 57. Data subset from figure 56 showing (a) accumulated Na volume
and (b) flowmeter output voltage in a regime where flow rate
is a linearly-varying function of time. Error bars are displayed
on these data to show the relative uncertainties in each measurement.

C.2 Flowmeter Calibration Curve

Each data point in figure 58 was constructed using equation (8) to calculate the flow rate for each data point in a subset, such as the one depicted in figure 57, and graphing it as a function of the corresponding measured flowmeter output. Through a judicious selection of the calibration data subset analyzed, both $\dot{v}$ and flowmeter output voltage are linear functions of time. Consequently, they also necessarily satisfy the relationship in equation (1). A linear regression of the data in figure 58,

$$\dot{v} = mV + b \ , \tag{11}$$

is displayed and results in m = 0.4063 L/s / mV (6.440 gpm/mV) and b = 0 L/s (0 gpm). The errors on the coefficients of equation (11) were found by recreating this regression with each data point biased by its maximum uncertainty ($+\sigma$ found using equation (10)). Biasing the data in this manner serves to shift the curve fit coefficients by the greatest possible value relative to the initial regression. The process was repeated with each data point biased by the negative of its maximum uncertainty
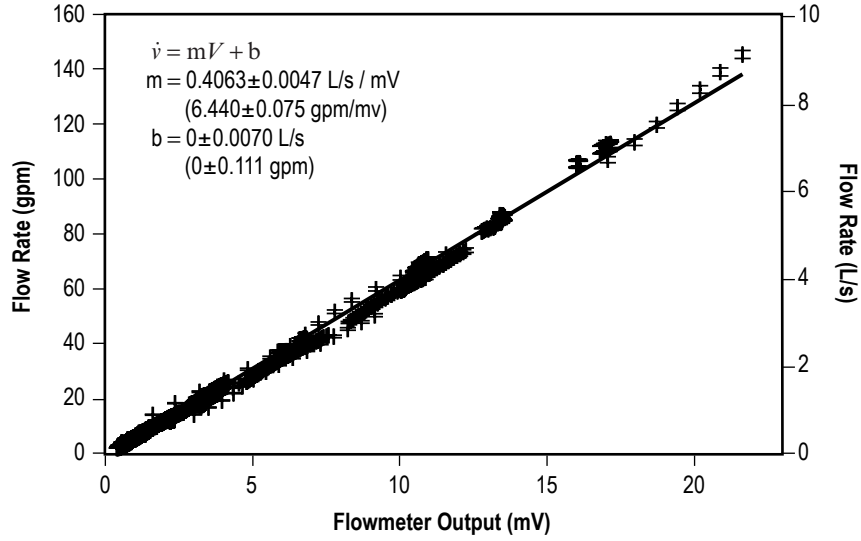
Figure 58. Volumetric flow rates displayed as a function of flowmeter output voltage (with error bars), and a curve fit to the data having coefficients and uncertainties as given in the figure.

$(-\sigma)$. The greater value in the variation of m and b from these latter two regressions is taken as the uncertainty on the coefficients in equation (11). The errors on m and b, as presented in figure 58, are $\sigma_m = 0.0047$ L/s / mV (0.075 gpm/mV) and $\sigma_b = 0.0070$ L/s (0.111 gpm).

APPENDIX D—ANNULAR LINEAR INDUCTION PUMP POWER MEASUREMENT, CALIBRATION/ERROR ANALYSIS

The Ohio Semitronics two-meter wattmeter is designed to measure three-phase input power levels up to 80 kW with a maximum uncertainty in the measurement of ±1% of full scale. In ATC testing, the ALIP power level was typically below 4 kW and, in some cases, down to the level of watts. In addition, the accuracy of the instrument when used to measure the power being supplied by the VFD, which does not produce a purely sinusoidal current or voltage—even when employing the sine wave filter—was unknown. As a consequence, effort was invested to independently measure the input power into the pump for the purpose of validating the measurement accuracy and developing a calibration to significantly reduce uncertainty in measured power.

Referring to figure 33 in section 4.2 and following the discussion in Walden's two-meter wattmeter,[10] the instantaneous real power delivered to the pump at any instant in time (regardless of whether the load is wired in a delta or wye configuration) is

$$P = V_{AC}I_A + V_{BC}I_B \; . \tag{12}$$

Consequently, a calibration can be performed by simultaneously and independently measuring these two differential voltages and two currents to calculate the power being delivered to the pump. The independent measurement was performed using a Tektronix TDS684C oscilloscope, Tektronix differential P5210 voltage probe, and Pearson model 101 current monitors. A measure of the currents, voltages, and calculated power levels are given in figure 59. The fact that the load is unbalanced—different current levels in all three legs—leads to a variation in the instantaneous power delivered to the pump as a function of time.

An average of the instantaneous power measurement (taken over several cycles of the waveforms and denoted as P_{scope}) was compared to the power measurement obtained using the wattmeter and data acquisition system (P_{DAQ}). Samples of these measurements obtained at many different ALIP operating voltages for two different frequencies are presented in figure 60. The ratio P_{scope}/P_{DAQ} deviates from unity as the power level is reduced and asymptotes to unity at higher power levels. The error bars found on the data for P_{scope} were obtained by taking the full width of the instantaneous power data scatter (shown representatively on the power data in fig. 59) and multiplying it by 0.66 to obtain the 1-σ variation on the power measurement. It is important to note that this is not the same as taking the width of the oscillation in power since that variation is a real aspect of the waveform and not an uncertainty or error.

The calibration was produced by curve fitting the following function to the data for each frequency:

$$y = y_0 + A e^{-\left[ln\left(x/x_0\right)/\sigma \right]^2} \; , \tag{13}$$

97
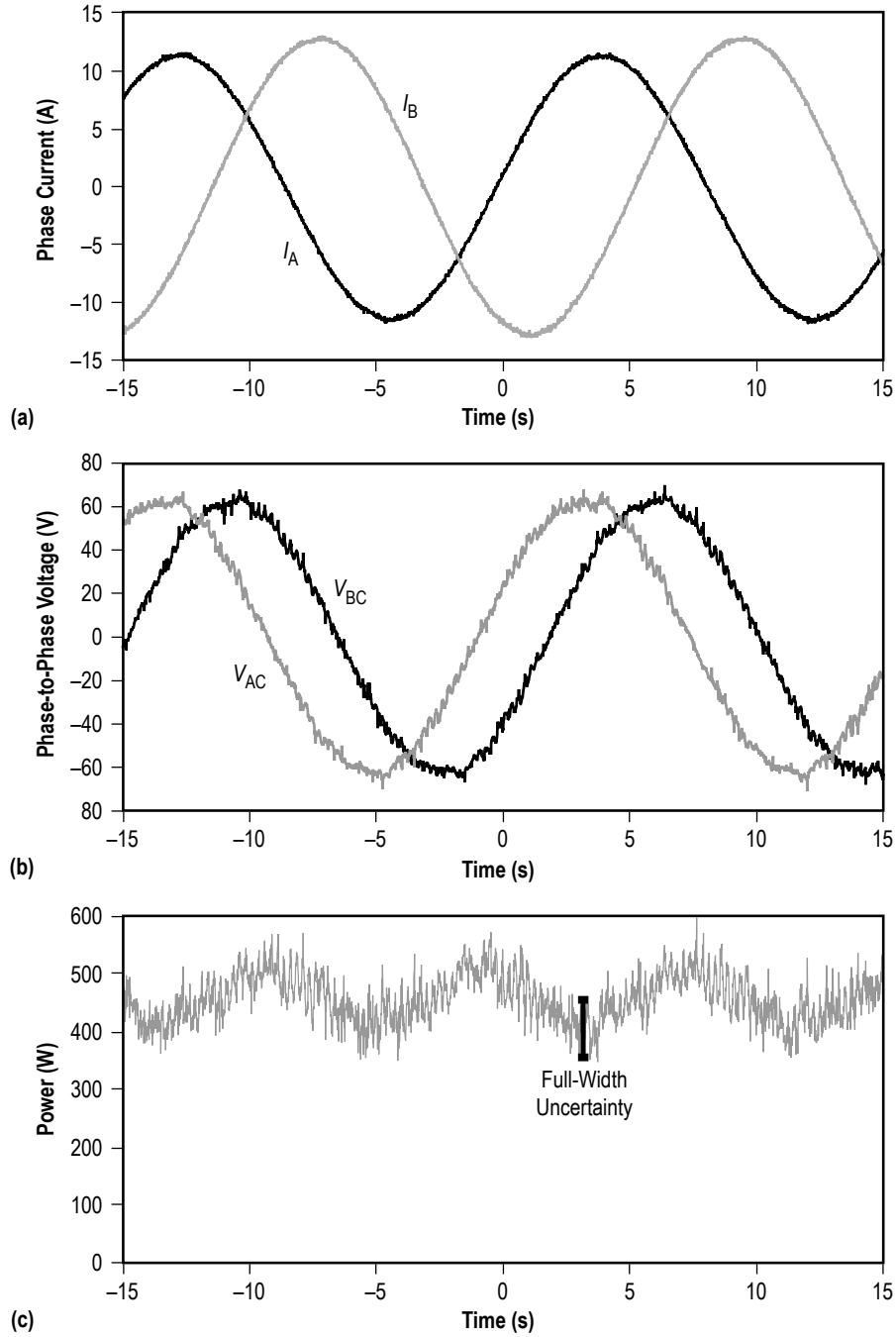
Figure 59. Sample (a) phase currents, (b) phase-to-phase voltages, and (c) calculated power delivered to the pump.

where the fit coefficients are y_0, A, x_0, and σ. The error band on the fit is determined by fitting the same function to the data plus and minus the error on the value of P_{scope}/P_{DAQ}. Examples of these curve fits are shown in figure 60. Curve fit functions for each frequency were derived in this manner and are used to correct the DAQ system data and yield measurement uncertainties on the power measurements data up to the point where the fit function was unity, $P_{scope}/P_{DAQ}=1$. At power levels above that point, the DAQ measurement was directly used and the error was taken as the
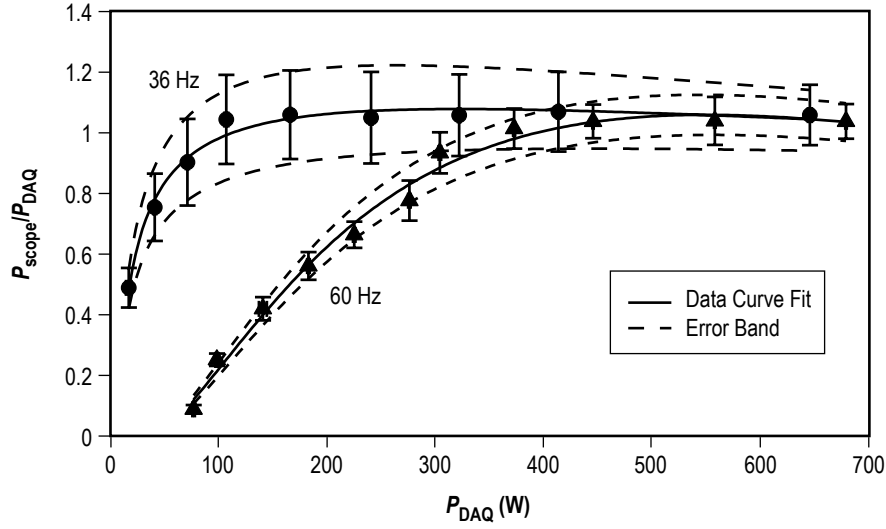
Figure 60. Power measurements and error bands obtained at many
different ALIP operating voltages for 36 and 60 Hz.

numerical value of the error band at this crossover between the fit function and the location where
$P_{\text{scope}}/P_{\text{DAQ}}$. The fit function does not necessarily asymptote to unity, but the ratio between P_{scope}
and P_{DAQ} does. The calibration is effectively a 'patch' of these two calibration/correction solutions
to obtain a function that is applicable throughout the measurement range. The coefficients on the
calibration corrections and the associated error bands are given in table 2.

Table 2. Coefficients on the power measurement calibration
corrections and associated error bands.

	y_0	A	x_0	σ	Applicability (W)
33 Hz	−12.365	13.4429	246.591	12.706	<630
36 Hz	−12.3497	13.4237	323.796	13.7807	<900
39 Hz	−12.4494	13.5356	293.874	13.1368	<830
60 Hz	−0.04827	1.10308	550.518	1.42829	<755
60 Hz (wall power)	1.00483	0.050056	39.0713	0.848073	<200
Positive Error Band					
33 Hz	−12.3397	13.5695	240.356	12.0001	
36 Hz	−12.2602	13.4732	269.941	12.1648	
39 Hz	−12.2749	13.5371	263.776	13.4569	
60 Hz	−0.05044	1.1713	544.242	1.4316	
60 Hz (wall power)	1.05266	0.088366	21.3474	1.10833	
Negative Error Band					
33 Hz	−12.5078	13.434	254.9	13.6268	
36 Hz	−12.4466	13.3901	449.23	16.2922	
39 Hz	−12.5508	13.4626	324.138	12.7979	
60 Hz	−0.04625	1.03516	557.64	1.4244	
60 Hz (wall power)	0.735827	0.241423	116.445	4.87674	

APPENDIX E—HALL PROBE DESIGN AND IMPLEMENTATION

The two-axis Hall probe used to measure the time-varying internal magnetic field in the annular flow channel of the ALIP is shown in figure 61. The probe tip is comprised of two Allegro A1301 ratiometric linear Hall-effect sensor, surface mount, integrated circuits. One sensor is oriented to provide a measure of the radial magnetic field component and the other is mounted to measure the axial component. The magnetic field sensitivity specification for this sensor model is nominally 2.5 mV/G and has a frequency response ($\approx$30 kHz) sufficient to capture the time-varying fields in the ALIP.
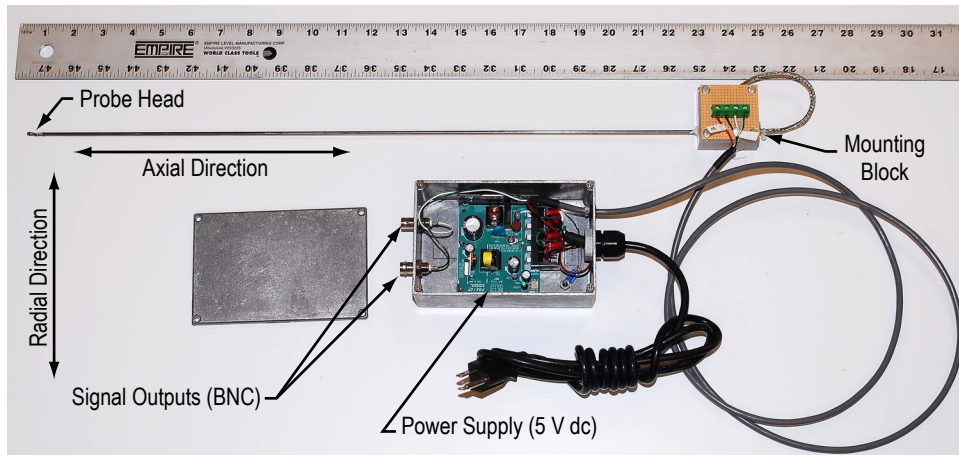

Figure 61. Hardware comprising the two-axis Hall probe.

Calibration of the probe tips was performed by measuring the field emitted from a SmCo rare-Earth magnet with the Hall sensors and then repeating those measurements using a Lakeshore model 421 gaussmeter. The calibration curves for the axial and radial probe heads are developed by comparing the two measurements, and are presented in figure 62.

The probe was mounted on a precision translation stage and inserted into the annular channel of the ALIP. Current was applied to the ALIP, and the axial and radial magnetic field measurements were captured on an oscilloscope (triggered to the rising current level in one of the pump legs to ensure that time was aligned in every data set). After capturing data at one position, the probe was translated axially and the process was repeated. This yielded a measure of the magnetic field at every location over several cycles of the current. Querying these data for the magnetic field values at a particular instant in time allows for the construction of spatial magnetic field maps. Repeating this process for several different times allows for the reconstruction of the spatial and temporal evolution of the magnetic field.
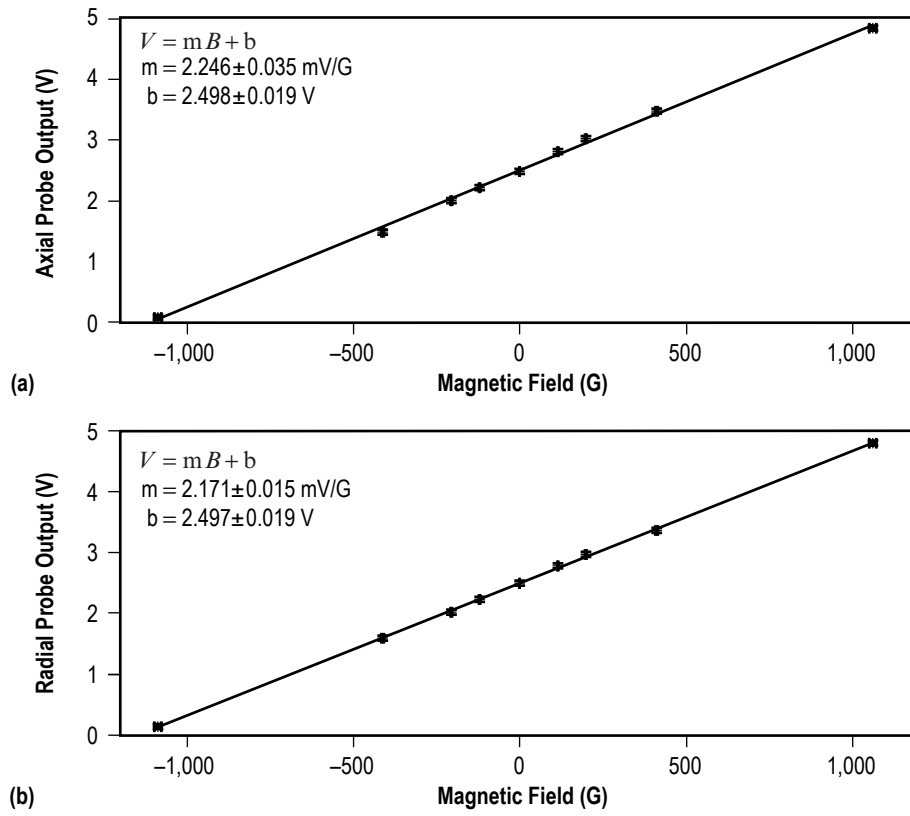
Figure 62. Calibration curves for the (a) axial and (b) radial Hall probes.

REFERENCES

1. Nainiger, J.: "Affordable Fission Surface Power System Study Final Report," NASA Exploration Systems Mission Directorate Report, October 2007.

2. Mason, L.S.: "A Comparison of Fission Power System Options for Lunar and Mars Surface Applications," *NASA/TM—2006–214120*, Glenn Research Center, Cleveland, OH, February 2006.

3. Mason, L.S.: "A Practical Approach to Starting Fission Surface Power Development," *NASA/TM—2006–214366*, Glenn Research Center, Cleveland, OH, July 2006.

4. Mason, L.S.; Poston, D.; and Qualls, L.: "System Concepts for Affordable Fission Surface Power," *NASA/TM—2008–215166*, Glenn Research Center, Cleveland, OH, January 2008.

5. Palac, D.; Mason, L.; and Harlow, S.: "Fission Surface Power Technology Development Status," *NASA/TM—2009–215602*, Glenn Research Center, Cleveland, OH, March 2009.

6. Adkins, H.; and Werner, J.E.: "Analysis of the Fission Surface Power Annular Linear Induction Pump Design Tools Based on Performance Test Results," Idaho National Laboratory Technical Report INL/EXT-10-18211, 2010.

7. Godfroy, T.J.; Van Dyke, M.; and Dickens, R.: "Realistic Development and Testing of Fission Systems at a Non-Nuclear Testing Facility," Space Technologies and Applications International Forum, STAIF-2000, *AIP Conf. Proc.*, Vol. 504, pp. 1208–1210, 2000.

8. Van Dyke, M.; Godfroy, T.J.; Houts, M.; et al.: "Results of a First Generation Least Expensive Approach to Fission Module Tests: Non-Nuclear Testing of a Fission System," Space Technologies and Applications International Forum, STAIF-2000, *AIP Conf. Proc.*, Vol. 504, pp. 1211–1217, 2000.

9. Polzin, K.A.; Markusic, T.E.; Stanojev, B.J.; et al.: "Electromagnetic Flow Sensor for Liquid-Metal-Fed Electric Propulsion," *J. Prop. Power*, Vol. 24, No. 5, pp. 1141–1143, 2008.

10. Walden, B.: "The Two-Meter Wattmeter Method," Technical Documentation, Ohio Semitronics, Inc., Hilliard, OH, 2004.

11. Coleman, H.W.; and Steele, W.G.: *Experimentation and Uncertainty Analysis for Engineers*, John Wiley and Sons, Inc., New York, 1999.

12. Majumdar, A.; Steadman, T.; and Moore, R.: "Generalized Fluid System Simulation Program (GFSSP) Version 5.0," Thermal and Combustion Analysis Branch Internal Report, NASA Marshall Space Flight Center, AL, February 2007.

13. Jackson, C.B., editor: Liquid Metals Handbook: NaK Supplement, TID-5277, Atomic Energy Commission, Department of the Navy, Washington, DC, 1955.

14. Fox, R.W.; and McDonald, A.T.: *Introduction to Fluid Mechanics*, 2nd ed., John Wiley and Sons, Inc., 1978.

15. Mausteller, J.W.; Tepper, F.; and Rodgers, S.J.: *Alkali Metal Handling and Systems Operating Techniques*, Gordon and Breach, Science Publishers, p. 218, New York, 1967.

REPORT DOCUMENTATION PAGE

1. REPORT DATE (DD-MM-YYYY) 01–05–2010	2. REPORT TYPE Technical Publication	3. DATES COVERED (From - To)

4. TITLE AND SUBTITLE Performance Testing of a Prototypic Annular Linear Induction Pump for Fission Surface Power	5a. CONTRACT NUMBER
	5b. GRANT NUMBER
	5c. PROGRAM ELEMENT NUMBER
6. AUTHOR(S) K.A. Polzin, J.B. Pearson, M.P. Schoenfeld, K. Webster, M.G. Houts, T.J. Godfroy,* and J.A. Bossard**	5d. PROJECT NUMBER
	5e. TASK NUMBER
	5f. WORK UNIT NUMBER

7. PERFORMING ORGANIZATION NAME(S) AND ADDRESS(ES) George C. Marshall Space Flight Center Marshall Space Flight Center, AL 35812	8. PERFORMING ORGANIZATION REPORT NUMBER M–1279

9. SPONSORING/MONITORING AGENCY NAME(S) AND ADDRESS(ES) National Aeronautics and Space Administration Washington, DC 20546–0001	10. SPONSORING/MONITOR'S ACRONYM(S) NASA
	11. SPONSORING/MONITORING REPORT NUMBER NASA/TP—2010–216430

12. DISTRIBUTION/AVAILABILITY STATEMENT
Unclassified-Unlimited
Subject Category 20
Availability: NASA CASI (443–757–5802)

13. SUPPLEMENTARY NOTES
Prepared by the Propulsion Systems Department, Engineering Directorate
*Maximum Technology Corporation, Huntsville, AL   **BSRD, LLC/Yetispace, Inc., Huntsville, AL

14. ABSTRACT
Results of performance testing of an annular linear induction pump are presented. The pump electromagnetically pumps liquid metal (NaK) through a circuit specially designed to allow for quantification of the performance. Testing was conducted over a range of conditions, including frequencies of 33, 36, 39, and 60 Hz, liquid metal temperatures from 25 to 525 °C, and input voltages from 5 to 120 V. Pump performance spanned a range of flow rates from roughly 0.16 to 5.7 L/s (2.5 to 90 gpm), and pressure head <1 to 90 kPa (<0.145 to 13 psi). The maximum efficiency measured during testing was slightly greater than 6%. The efficiency was fairly insensitive to input frequency from 33 to 39 Hz, and was markedly lower at 60 Hz. In addition, the efficiency decreased as the NaK temperature was raised. While the pump was powered, the fluid responded immediately to changes in the input power level, but when power was removed altogether, there was a brief slow-down period before the fluid would come to rest. The performance of the pump operating on a variable frequency drive providing 60 Hz power compared favorably with the same pump operating on 60 Hz power drawn directly from the electrical grid.

15. SUBJECT TERMS
ALIP, annular linear induction pump, pump performance curve, space nuclear power, fission surface power, NaK

16. SECURITY CLASSIFICATION OF:			17. LIMITATION OF ABSTRACT	18. NUMBER OF PAGES	19a. NAME OF RESPONSIBLE PERSON STI Help Desk at email: help@sti.nasa.gov
a. REPORT U	b. ABSTRACT U	c. THIS PAGE U	UU	118	19b. TELEPHONE NUMBER (Include area code) STI Help Desk at: 443–757–5802

National Aeronautics and
Space Administration
IS20
George C. Marshall Space Flight Center
Marshall Space Flight Center, Alabama
35812